AN ABSTRACT OF THE THESIS OF

Rachel Katie Adams for the degree of Master of Science in Civil Engineering presented on June 1, 2017.

Title: Near-Surface Response of Beach Sand: An Experimental Investigation

Abstract approved: _____

H. Benjamin Mason

Keywords: near-surface response, low confinement, friction angle, shear strength, granular characteristics, particle shape

The near-surface region of a coastal sediment bed is complex and dynamic. At some sites, near-surface sediment deposits are susceptible to extreme events, such as tsunamis or other large overflows, which induce high shear stresses on the sediment bed. The specific properties of sediment beds subjected to such extreme loading govern the response. Current sediment instability and transport models employ index characteristics of the sediment bed to predict the response; however, additional geotechnical factors could be considered in the models. The work herein aims to connect geotechnical and coastal engineering communities by characterizing near-surface

beach sediments with geotechnical methods to inform more inclusive sediment instability and transport models as they continue to develop.

A sediment bed investigation is performed in South Beach, Newport, Oregon, which is susceptible to a sizable tsunami following the impending Cascadia Subduction Zone earthquake. A laboratory program is completed to determine the index properties and near-surface response trends of the sediment sampled from South Beach and to populate a database. More specifically, sieve analyses, particle shape analyses, specific gravity testing, minimum and maximum packing density testing, triaxial testing, simple shear testing, angle of repose testing, and inclined plane testing are performed and the methodology and results are discussed.

Low confinement strength testing is performed using a simple shear device, which is thought to roughly mimic the type of shearing caused by tsunami-induced bed-shear stresses. Angle of repose and inclined plane testing are also performed to observe the response of the exposed sediment at the surface. In addition, existing correlations are evaluated for South Beach sediment that relate index properties to the response (e.g., using particle roundness to estimate the critical state friction angle) to observe the accuracy of the correlations for the fine sand. The results show similar trends found by other researchers using various testing techniques; however, the simple shear device shows some weaknesses when performing low confinement tests.

A specific interest of the current study is understanding how the friction angle changes with decreasing confinement (i.e., as the in situ location of the deposit approaches the surface of the sediment bed) for the South Beach sand investigated. The friction angle is an important property that governs the response of sediment to

various types of loading, including sediment exposed to bed-shear stresses.

The results show that the investigated cross section of South Beach appears to be a generally stable and homogeneous environment; therefore, the sediment properties and response trends defined herein are expected to be applicable to the specific location for the foreseeable future, notwithstanding significant morphological changes from impending natural disasters or human-induced changes. The results also show that established correlations that utilize particle shape to estimate limiting packing densities and friction angle are generally applicable for the South Beach sediment. Although there are challenges with performing low confinement simple shear testing, the friction angle near the surface of the respective sediment bed is found to increase following the comprehensive interpretation of the test results. In addition, the laboratory results show that at depths less than about 3 m below the surface of a simulated dry, medium density sediment bed, the critical state and peak friction angles increase, and may be well estimated by the angle of repose and pocket-friction angles at the surface.

The application of the sediment properties defined herein is focused towards sediment instability and transport models for the investigated location of South Beach; however, defining near-surface sediment properties and response trends is also important for many other engineering applications. Applications involving shallow soil response, including foundations, retaining structures, landslides, and lunar construction (where the 'near-surface' region would be a much larger zone due to the low stress environment of the moon), would be influenced by accounting for the effect of the altered loading response trends of soils near the surface. Considering the altered

response trends (i.e., sediment strength properties) would improve the accuracy of analyses for the noted applications.

The results of the current study imply that considering near-surface sediment characteristics will lead to improved sediment instability and transport model predictions, as expected. The improved predictions will help researchers determine appropriate input parameters to model their application of interest and result in better infrastructure design when the response of the near-surface region to extreme overflow events is of concern. For similar granular soil studies, laboratory procedures are suggested following the evaluation of methods performed herein while developing the database of properties for South Beach sand.

Near-Surface Response of Beach Sand: An Experimental Investigation

by

Rachel Katie Adams

A THESIS

submitted to

Oregon State University

in partial fulfillment of
the requirements for the
degree of

Master of Science

Presented June 1, 2017
Commencement June 2017

Master of Science thesis of Rachel Katie Adams presented on June 1, 2017.

APPROVED:

Major Professor, representing Civil Engineering

Head of the School of Civil and Construction Engineering

Dean of the Graduate School

I understand that my thesis will become part of the permanent collection of Oregon State University libraries. My signature below authorizes release of my thesis to any reader upon request.

Rachel Katie Adams, Author

ACKNOWLEDGEMENTS

Upon completion of this thesis, I owe great thanks to my advisor, Dr. Ben Mason. Over the past three years of working together during my undergraduate and graduate degrees at Oregon State University, Dr. Mason has encouraged, challenged, and coached me through achieving my academic and personal goals. Together, we outlined a research project that, while investigating an interesting and important topic, allowed me to strengthen my understanding of soil mechanics and geotechnical laboratory testing. I would also like to thank the remainder of my graduate committee, Dr. Ben Leshchinsky, Dr. Harry Yeh, and Dr. Andrew Meigs, for their feedback, assistance, and thoughtful comments that have helped me to complete this work.

I would like to thank Dr. Abbas Abdollahi for his mentorship and friendship throughout my geotechnical research work. I am also grateful to the remainder of the Mason research group for their thoughtful discussions, advice, and support. This would have been a lonely journey without their friendship. I am thankful to James Batti and my fellow laboratory researchers in Graf Hall, specifically Gabe Gray, for all of their assistance in addressing laboratory issues. I would like to thank Dr. Matt Evans and Dr. Armin Stuedlein for providing access and advice to use specific laboratory equipment, and Greyson Termini who helped modify and repair equipment necessary to complete this work. Dr. Brady Gibbons and his research group provided access to the microscope in their research laboratory for particle imaging and I am very thankful for all of their assistance. I would also like to thank Maggie Exton and Sam Harry for their efforts setting up a high speed camera for inclined plane testing.

I thank my family and friends for their patience, support, and love throughout my time in graduate school. My father, Mark Adams, and my mother and step-father, Sally Adams and Kelly Fough, provided unwavering support throughout my education and I am forever thankful for their encouragement. I would like to sincerely thank my fiancé, Gabriel Acosta, for making my entire graduate school journey enjoyable, by constantly providing plans to work towards and look forward to.

This work would have not been possible without the funding that I received throughout my research at Oregon State University. I am grateful for my various assistantships and fellowships, specifically the Yamamuro Fellowship.

TABLE OF CONTENTS

TABLE OF CONTENTS (Continued)

LIST OF FIGURES

LIST OF FIGURES (Continued)

LIST OF FIGURES (Continued)

LIST OF TABLES

LIST OF APPENDIX FIGURES

Chapter 1: Introduction

The most dynamic region of a sediment deposit in coastal areas is the surficial layer, because it is susceptible to disturbance through a variety of processes. For instance, the displacement of surficial sediment particles (i.e., sediment transport) occurs naturally from imposed fluid or wind bed-shear stresses. There is clearly a need to predict when sediment transport of near-surface sediments is likely to occur during various initiating processes. A common approach, for predicting the occurrence of sediment transport, is the Shields (1936) approach. In the Shields (1936) approach, the response of granular surface particles to bed-shear stresses is typically estimated by comparing the non-dimensional Shields parameter, which is the ratio of the bed-shear stress to the buoyant weight of the sediment, to an empirically determined critical Shields parameter, which is determined experimentally as a function of the flow Reynolds number. It is evident that the sediment bed characteristics (e.g., the mean grain-size diameter and density of particulates) are important for the preceding calculations.

In geotechnical engineering applications, "continuum" soil properties are typically employed to estimate soil response during perturbation. The word "continuum" implies that the strength properties for a collection of individual particles are "averaged" over the collection of particles; i.e., the concepts of stress and strain of a soil element are valid. A typical relationship used to understand when failure of coarse-

grained sediments occurs is the Mohr-Coulomb failure criterion. For a soil element within a uniform deposit, the Mohr-Coulomb failure criterion assumes a linear relationship between confining pressure (i.e., depth of embedment) and shear strength. For coarse-grained soils, such as beach sands, the stress-independent component of the linear Mohr-Coulomb failure criterion (i.e., the cohesion intercept, c') is typically approximately zero, so the mobilized shear strength at a given stress is solely a function of the slope, which is given by the friction angle, ϕ'.

Multiple researchers (e.g., Ponce and Bell, 1971; Stroud, 1971; Fukushima and Tatsuoka, 1984) have shown that sediment deposits near the ground surface exhibit unique behavior with respect to the Mohr-Coulomb strength parameters, and that the contribution of different resistance mechanisms to the overall mobilized friction angle (i.e., mobilized shear strength) is complex. The distinction of shear strength for near-surface sediment is important, because it governs the response of deposits in low-stress environments during load application.

Following the preceding discussion, it is evident that prediction of sediment transport requires knowledge of geotechnical engineering, and conversely, when geotechnical engineering conventions are applied to near-surface sediments, the principles of sediment transport are also important. For instance, using typical strength parameters (i.e., friction angles) to predict the response of near-surface sediments without considering the nuances of the lower confining stresses may be inappropriate. Additionally, although the geotechnical engineering community has accepted that sediment properties, such as particle size, gradation, shape, and packing density, affect the response of perturbed soils (e.g., Santamarina et al., 2001; Mitchell and Soga, 2005),

many sediment transport models only employ simple index properties, such as the mean grain-size diameter. In conclusion, to understand the response of near-surface sediments to typical and extreme perturbations, it is necessary to combine knowledge from the fields of geotechnical and coastal engineering (specifically relating to the study of sediment transport). An implicit aim of this thesis is to further connect the knowledge of the aforementioned fields.

As previously alluded to, at some sites, near-surface sediment deposits are susceptible to extreme events, such as tsunamis or other large overflows. Tsunamis cause significant damage to coastal communities. Notably, the 2004 Indian Ocean Tsunami (Cluff, 2007) and the 2011 Great East Japan Tsunami (EERI, 2011) caused substantial loss-of-life and billions of dollars in damage to coastal infrastructure. The inundation of water during tsunami runup can impose large bed-shear stresses on near-surface sediments, which can cause significant sediment transport, enhanced scour, and destruction of coastal structures (Tonkin et al., 2003; Yeh and Mason, 2014). Scouring is also exacerbated during tsunami draw-down, because the overlying pressures from the tsunami wave are quickly removed, which can create an upward flow of dissipating pore-water pressures (Yeh and Mason, 2014).

In addition to identifying the near-surface strength properties of a sediment bed for the purposes of understanding sediment instability in a coastal environment, there are many applications for which understanding soil response at low confinement is important (Ponce and Bell, 1971; Stroud, 1971; Fukushima and Tatsuoka, 1984; Chakraborty and Salgado, 2010; Sadrekarimi and Olson, 2011). The accuracy of all low confinement geotechnical engineering application analyses that utilize the

friction angle to define the shear strength of granular sediment would be improved by considering the true friction angle of the in situ environment, including shallow bearing capacity problems, shallow sand slope failure analysis, interpreting in situ tests performed at shallow depths, and simulating 1-g model tests (i.e., those not modeled in a centrifuge to alter gravitational forces). Another low-stress environment of interest for future applications may be the moon, as lunar construction becomes a more realistic venture (Chakraborty and Salgado, 2010). Considering the friction angle of sediment as a function of confining pressure (i.e., depth) would lead to more accurate analyses of near-surface environments.

The important influence of sediment bed properties near the ground surface justify the aims of this thesis to perform a comprehensive study that will identify relevant geotechnical properties and loading response trends of a selected beach sediment. The developed database strives to inform inclusive sediment instability and transport models for the specified coastal site. The improved accuracy of sediment transport models that more completely consider the near-surface response of the sediment bed will lead to better coastal infrastructure design and improve the resiliency of coastal communities.

1.1 Objectives and Overview of Current Study

A sediment bed investigation is performed in South Beach, Newport, Oregon, which is susceptible to a sizable tsunami following the impending Cascadia Subduction Zone earthquake (Atwater et al., 1995; Priest et al., 1997; Schulz, 2015). Tsunami-induced

scour will greatly alter the coastal morphology of South Beach and cause damage to the surrounding infrastructure (e.g., bridge piers, building footings, ports). South Beach, Newport, Oregon is in close vicinity to important coastal infrastructure, such as Hatfield Marine Science Center. The selected site is also the nearest beach location to Oregon State University, where the present research is conducted. The site location is convenient for obtaining additional samples or other beach information to complete the proposed investigation.

The primary goal of the study performed herein is to create a database of relevant properties of South Beach sediment as input parameters for sediment instability and transport models that include more details of the respective sediment bed. In addition to classic index properties provided (e.g., mean grain-size diameter, particle shape, limiting void ratios), the sediment's strength properties were investigated. More specifically, various characteristic friction angles were determined for different in situ conditions of interest, i.e., considering the sediment deposit location moving up through the bed to the ground surface. The detailed characterization of a natural beach sand also provided opportunities to investigate granular soil correlations, such as using shape properties to estimate limiting void ratios and friction angle. Surficial sediment samples were obtained from the selected beach cross-section at various tidal marks throughout the course of the study to observe the spatial and seasonal variability of the South Beach site. More information and background about the site of interest is provided in §2.1. A testing program was performed to characterize the soil and define the response under a spectrum of confinement conditions.

Prepared testing specimens of the South Beach sediment samples were subjected

to sieve analyses, particle shape analyses, specific gravity testing, minimum and maximum packing density testing, consolidated-drained triaxial compression testing, constant vertical stress simple shear compression testing, angle of repose testing, and inclined plane testing. Few researchers have related low confinement test results used to simulate the near-surface sediment response to particle behavior under essentially no confinement at the surface, especially for fine sands. The methodology for the laboratory program is provided with an evaluation of the respective testing methods. The implications of the results defining the near-surface region of the simulated sediment bed are considered for sediment instability and transport model applications. The current study aims to help bridge the gap between geotechnical and coastal engineering communities to ultimately lead to better infrastructure design when the response of the near-surface region to extreme overflow events is of concern. The outcomes of this study revealed future work to be performed to further clarify the complexities of sediment response near the ground surface. Although a coastal focus is adopted herein, understanding sediment characteristics near the surface is important for predicting the response for various engineering problems involving low-stress environments.

1.2 Research Questions and Thesis Organization

With the stated objectives and aims of this thesis, the specific research questions that will be addressed in the current study are:

1. What are the morphological characteristics of the South Beach, Newport, Ore-

gon site and how do they change during the course of this study?

2. How well do existing correlations relating soil index properties and the response of granular materials apply to South Beach sand studied herein?

3. How does the friction angle and the mechanism of mobilized shear strength change in the near-surface region of the sediment bed for South Beach sand?

4. How are dilatant behavior and stiffness of the sediment affected by shearing at low confining pressures in the utilized simple shear device?

5. Is simple shear testing a sufficient method to investigate low confinement behavior?

6. What affect would the implementation of the specific near-surface sediment properties and response have on sediment instability and transport models?

Notably, Question 6 will only be preliminarily answered within this thesis, and it will be highlighted as a rich question for future work.

The organization of this thesis is presented as follows: Chapter 2 provides background information and a brief literature synthesis that are helpful for understanding the work presented herein. Chapter 3 details the methodology of the performed laboratory program and provides the typically reported, unadjusted results of the respective laboratory tests. Chapter 4 utilizes the results obtained in Chapter 3 to perform analysis techniques not typically employed in sediment characterization studies. Chapter 4 also details the evaluation of testing methods performed herein and

discusses the implications of the results of this study on sediment instability applications. Finally, Chapter 5 presents the concluding remarks and focused discussions in response to the specific research questions.

NOTATION:

The significant notation utilized throughout this thesis is defined in the following general order of occurrence:

d_{10} Particle diameter which 10% of the grain-size distribution is finer than (mm)

d_{30} Particle diameter which 30% of the grain-size distribution is finer than (mm)

d_{50} Mean grain-size diameter (mm)

d_{60} Particle diameter which 60% of the grain-size distribution is finer than (mm)

C_u Coefficient of uniformity

C_c Coefficient of curvature

s Sphericity

r Roundness

$r_{max-insc}$ Radius of the largest inscribed circle of a particle image projection

$r_{min-circ}$ Radius of the smallest circumscribed circle of a particle image projection

d_1 Major diameter of an ellipse (mm)

d_2 Minor diameter of an ellipse (mm)

d_{equiv} Equivalent sieve opening size for an ellipsoidal particle model (mm)

G_s Specific gravity

e_{min} Minimum void ratio

e_{max} Maximum void ratio

e Void ratio

n Porosity

D_r Relative density (%)

γ_d Dry sediment unit weight (kN/m^3)

γ_w Unit weight of water (9.81 kN/m^3)

σ'_1 Major principal stress (kPa)

σ'_3 Minor principal stress (kPa)

q' Deviatoric stress (kPa)

p' Mean stress (kPa)

p_{ref} Reference pressure (1 kPa)

ε_1 Major principal strain - triaxial testing (%)

ε_v Volumetric strain - triaxial testing (%)

τ' Shear stress (kPa)

σ'_v Vertical effective stress (kPa)

σ'_h Horizontal effective stress (kPa)

γ Shear strain (%)

ε Axial strain - simple shear testing (%)

ϕ' Mobilized friction angle (°)

ϕ'_μ Sliding friction angle (°)

ϕ'_r Particle rearrangement friction angle (°)

ϕ'_d Dilation angle (°)

ϕ'_{cs} Critical state friction angle (°)

ϕ'_{cv} Constant volume friction angle (°)

ϕ'_p Peak friction angle (°)

I_R Relative dilatancy index

Q and R Fitting parameters for dilation angle predictions

ν Poisson's ratio

E Modulus of elasticity (MPa)

G Shear modulus (MPa)

D Constrained modulus (MPa)

K_0 At-rest earth pressure coefficient

B Skempton's B value

u Pore-water pressure (kPa)

ϕ'_{Rep} Angle of repose (°)

ϕ'_{IP} Pocket-friction angle (°)

z Depth (m)

c_v Coefficient of consolidation (mm^2/s)

Chapter 2: Background

2.1 Coastal Morphology

When investigating the seasonal and spatial trends of a beach cross section, it is important to understand the coastal morphology. The Oregon Department of Geology and Mineral Industries (DOGAMI, 2011) has developed documentation for the topographic changes of Oregon beaches over time. Historical beach profiles developed from topographic data are provided for a South Beach, Newport, Oregon Beach cross section, as shown in Figure 2.1a. The most relevant beach profile, denoted as "Southbeach 29", provided in the DOGAMI database is in close vicinity to the selected beach cross section of interest for the current study, located south of the Yaquina Bay jetty and just north of the beach outlet trail from the South Beach State Park parking lot, as shown in Figure 2.1b (within approximately 300 m north of the sampling cross section herein). Details of the beach cross section investigated in the current study will be detailed further in §3.1.

Figure 2.1a shows three beach profiles, representative of different dates. The oldest profile, from the summer of 1997, shows the surface of the sediment bed at a higher elevation within the swash zone [i.e., the portion of the beach that is alternatively wet and dry throughout the daily tide levels, between the Mean Lower Low Water (MLLW) and Mean Higher High Water (MHHW) levels (NOAA, 2013)] than the two

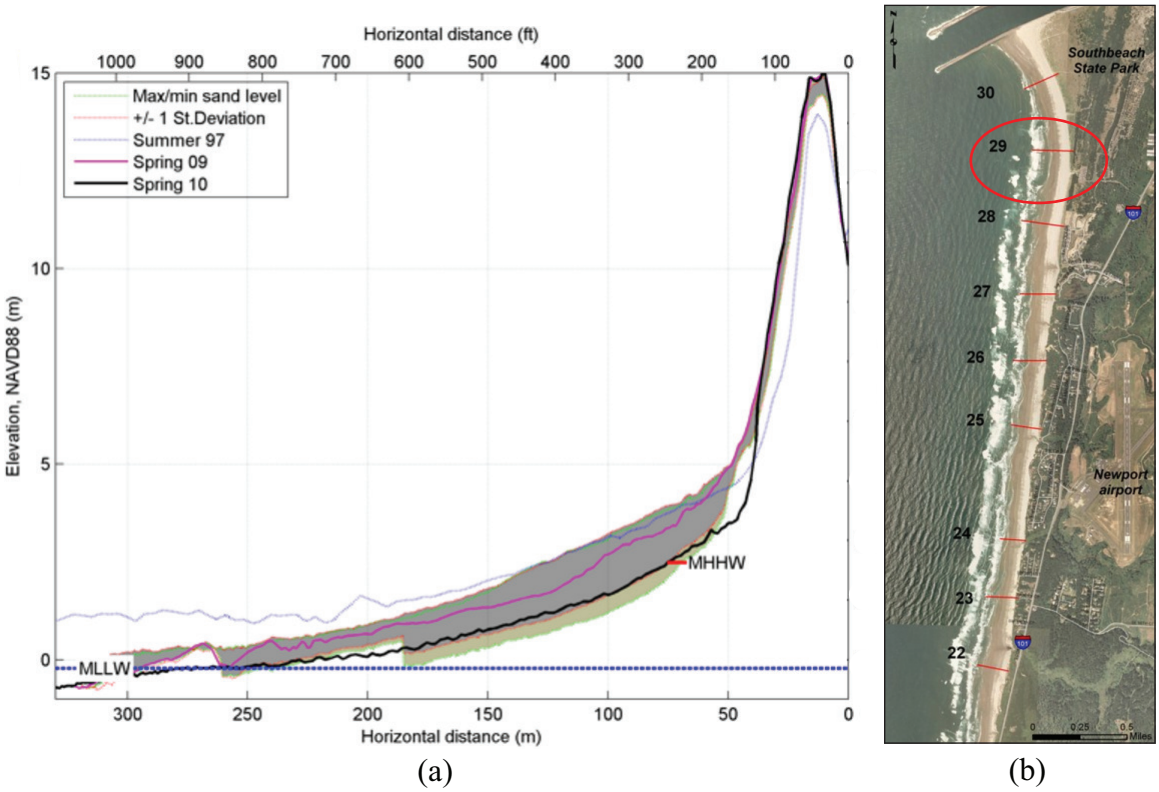

Figure 2.1: Beach profile history of South Beach, Newport, Oregon. Profiles of Southbeach 29 cross section (a), and location of the selected beach profile (b) (modified from DOGAMI, 2011).

spring profiles from 2009 and 2010. The exaggerated vertical scale of Figure 2.1a should be noted when making comparisons between profiles. The slope of the swash zone appears to be generally consistent over time, and for the 2010 spring profile, it is estimated as 1:75 (V:H, calculated from the elevation change between 0 m at the MLLW level and 4 m at the base of the sand dune, extending over the beach cross section length of approximately 300 m). Although the differences in the profiles presented in Figure 2.1a may be due to long-term morphology of the beach, there

are likely also seasonal effects, such as accretion and erosion of the beach during the summer and winter months, respectively, which may alter the beach topography (DOGAMI, 2011).

The gentle slope and wide swash zone of the beach profiles in South Beach, Newport, Oregon are characteristic of dissipative beaches (Shih and Komar, 1994). Dissipative beaches are composed of very fine sand grains (i.e., particles with diameters of about 0.3 mm or less). The low slope of dissipative beaches causes waves to break far offshore and the majority of the wave energy is dissipated while crossing the wide swash zone before reaching the base of the backing sand dune or bluff. Dissipative beaches have been found to have minimal seasonal variability, especially when compared with the variability of reflective beaches (i.e., steep beaches composed of coarse sand grains) (Shih and Komar, 1994).

Historical data of tidal levels are also documented for South Beach, Newport, Oregon, by the National Oceanic and Atmospheric Administration (NOAA). Figure 2.2 shows the monthly MHHW and MLLW levels for a twenty year span, dating back to the first available beach profile presented in Figure 2.1a. Generally, the MHHW and MLLW peak levels occur during the winter months and the low water levels occur in summer months. Figure 2.2 shows that the trends in water levels are consistent over time and no substantial changes to the wave conditions are apparent over the most recent twenty year span.

The preceding background on the morphology of South Beach, Newport, Oregon informs the assumption that there will be no substantial seasonal or long-term changes to the beach topography in the foreseeable future, notwithstanding significant

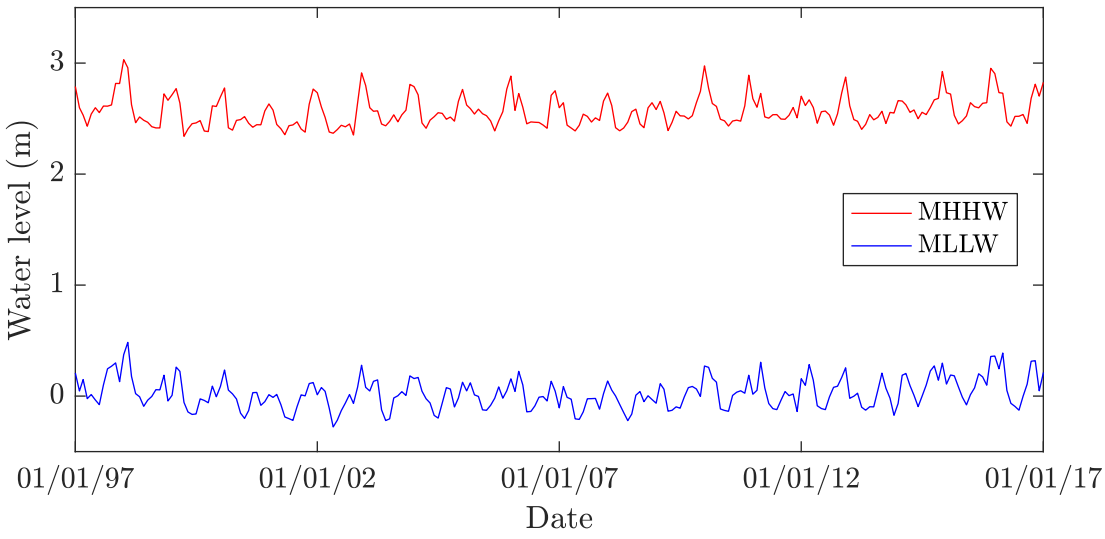

Figure 2.2: Historical monthly tidal level means. NOAA tidal levels for South Beach in reference to the MLLW datum for the present epoch (1983 to 2001).

morphological changes from impending natural disasters or human-induced changes. The initial site visits and sampling efforts performed herein reveal that the beach is composed of granular sediment. Accordingly, the following discussions and remainder of the current study will be relevant specifically to the properties and response of granular material.

2.2 Sediment Classification and Granular Properties

This thesis focuses on the investigation of sampled and reconstituted specimens to define the granular characteristics and mechanical behavior. Many studies have revealed that basic index properties of a collection of soil particles govern the response of the collection of soil, which necessitates investigation at the micro-scale. Index

properties, such as size and shape of particles, as well as information about the range of possible packing densities, are determined in the following subsections.

2.2.1 Particle Size

The cumulative distribution of particle sizes within a collection of soil is often used to classify the soil. Well-graded, uniform graded, and gap graded soils can be identified from the shape of the grain-size distribution curve. A well graded soil is one that has a wide range of particle sizes in the distribution, while uniform and gap graded soils are both forms of poorly graded soils, which are deficient in certain particle sizes (Bardet, 1997). In addition, characteristics of grain-size distribution curves can reveal information about the origins of a soil deposit (Santamarina et al., 2001). For example, alluvial terrace deposits and aeolian deposits are often poorly graded (Mitchell and Soga, 2005). The use of the grain-size distribution curve standardizes the presentation of gradation, which allows meaningful comparisons to be made between different soil types. When particle size analysis is paired with other descriptive details, like particle shape and color, more meaningful conclusions can be made about the mechanical behavior of the sediment of interest (Bardet, 1997).

The grain-size distribution curve is plotted as the fraction (or percentage) of a mass of soil particles that are finer than specified particle sizes. To appreciate the difference in magnitude between various particle sizes within a distribution, Mitchell and Soga (2005) suggests depicting the representative particles as scale drawings in addition to observing the typical semi-logarithmic grain-size distribution plot. Index

parameters obtained from the grain-size distribution curve, such as the mean grain-size diameter, d_{50} (i.e., the particle diameter corresponding to the 50th percentile of the grain-size distribution), are widely utilized and reported in soil investigations (Santamarina et al., 2001). The values of parameters such as d_{50} correlate to the sediment's mechanical behavior. Additional properties of the grain-size distribution curve, such as location, steepness, flatness, and general shape of the curve, are also correlated to engineering properties of the sediment. Parameters that take multiple points into account along the grain-size distribution curve have been developed to numerically describe the shape. The coefficient of uniformity, C_u, and the coefficient of curvature, C_c, are parameters that account for the slope and curvature of the grain-size distribution and are given as,

$$C_u = \frac{d_{60}}{d_{10}}, \qquad C_c = \frac{(d_{30})^2}{d_{10}d_{60}}, \tag{2.1}$$

where d_{10}, d_{30}, and d_{60} are the particle diameters corresponding to 10%, 30%, and 60% of the collection of soil being finer than the noted particle size, respectively. Sand is considered to be well graded when $C_u > 4$ and $1 < C_c < 3$ (Bardet, 1997). Physically, when $C_u > 4$, larger particles within the soil collection constitute the soil skeleton, and the smaller particles of the distribution fill the void space. With less void space present in the complete soil skeleton, a denser, more stable sediment arrangement is possible. Conversely, when $C_u = 1$, all particles are of equal size, or uniformly graded (Santamarina et al., 2001). Visually, a steep grain-size distribution curve indicates a uniform soil, containing only a narrow range of particle sizes, whereas a smooth,

concave upward curve indicates a well-graded soil (Bardet, 1997).

As stated by Santamarina et al. (2001), there are multiple definitions for the size of a particle, which are important for determining the grain-size distribution. Accordingly, it is important to determine particle size consistently within a study and report the respective methods of determining particle size. Data from a particle-size analysis do not produce a continuous grain-size distribution curve. Manual interpretation (i.e., sketching between data) and more sophisticated functional fits can be used to create a grain-size distribution curve from the data points determined in a particle-size analysis. However, some methods have limitations, such as failing to accurately represent the curve at extremes and assuming false symmetric trends.

A function developed to fit the grain-size distribution data for a wide range of sediments is presented by Fredlund et al. (2000). More specifically, Fredlund et al. (2000) utilizes the unimodal method of fitting an equation for well-graded and uniform soils. The developed unimodal equation, which can be fit to grain-size distribution data points determined via sieve analysis, is given as,

$$P_p(d) = \frac{1}{\left\{\ln\left[\exp(1) + \left(\frac{a_{gr}}{d}\right)^{n_{gr}}\right]\right\}^{m_{gr}}} \left\{1 - \left[\frac{\ln\left(1 + \frac{d_{rgr}}{d}\right)}{\ln\left(1 + \frac{d_{rgr}}{d_m}\right)}\right]^7\right\}, \qquad (2.2)$$

where $P_p(d)$ is the percentage of particles by mass passing a particular sieve size, a_{gr} is a parameter that designates the inflection point of the curve, n_{gr} is a parameter related to the steepest slope of the curve, m_{gr} is a parameter related to the shape of the curve as it approaches the fines region [i.e., particles passing the No. 200 sieve (0.075 mm sieve openings)], d_{rgr} is a parameter related to the amount of fines in a soil,

d is the diameter of any particle size under consideration, and d_m is the diameter of the minimum allowable size particle. There are limitations of the unimodal equation with gap-graded grain-size distributions, and the use of a bimodal equation is recommended for that case. The use of a mathematical equation is beneficial to estimate a continuous function for the grain-size distribution. From a continuous grain-size distribution function, parameters such as d_{50} can be consistently determined.

Standardized procedures for completing a sieve analysis and determining the distribution of particle sizes in a collection of soil are provided by ASTM D422-63 (2007), ASTM D6913-04 (2009), and ASTM C136/C136M-14 (2014). Square-mesh woven-wire cloth sieves are utilized to separate particles of different sizes. The soil sample is prepared and a specimen is poured through a stack of sieves with appropriately sized openings to capture the range of particle sizes within the sample. The stack of sieves is then agitated (typically with a mechanical sieve shaker) for ten to twenty minutes to separate the specimen into fractions that are retained on the individual sieves. The mass of the material retained on each sieve is then measured to determine the percent by mass of each particle size within the collection of soil. The particle sizes that constitute the soil may then be presented as a grain-size distribution curve with a representative function, such as the unimodal equation presented by Fredlund et al. (2000), fit to the measured data.

2.2.2 Particle Shape

In addition to particle size, particle shape is important for characterizing a collection of soil (Santamarina and Cho, 2004; Mitchell and Soga, 2005; Cho et al., 2006; Holtz et al., 2011). As discussed previously, the grain-size distribution curve is used for classifying soil; however, soil classification systems, including the Unified Soil Classification System (USCS) described in ASTM D2487-11 (2011), do not consider particle shape. Particle shape also affects the mechanical response of soil, including the range of possible packing densities, stiffness, and shear strength (Cho et al., 2006). It is recommended that particle shape be characterized and documented as a part of every soil investigation, especially when investigating clean sands and gravels.

Qualitative shape determination is common in geotechnical engineering (Mitchell and Soga, 2005; Holtz et al., 2011). Descriptions such as spherical, rounded, blocky, bulky, platy, flat, elliptical, elongated, needlelike, and flaky can be used to characterize particle shape. Descriptions of particle shape are established at three different scales: global, major surface features, and surface texture (Santamarina et al., 2001; Santamarina and Cho, 2004; Mitchell and Soga, 2005; Cho et al., 2006). Particle morphology is described at the global or particle scale, and texture, which reflects local roughness features, is important at smaller scales. The parameters that coincide with the three scales of particle shape descriptions are sphericity, s, roundness, r, and roughness. Values of low sphericity to high sphericity, and similarly, values of low roundness (i.e., high angularity) to high roundness, range from zero to one. Roundness values are divided into classes. Table 2.1 shows the roundness classes presented

Table 2.1: Particle roundness classification intervals (Powers, 1953).

Classification	Roundness intervals	
Very angular	0.12	0.17
Angular	0.17	0.25
Subangular	0.25	0.35
Subrounded	0.35	0.49
Rounded	0.49	0.70
Well rounded	0.70	1.0

in Powers (1953).

Sphericity, roundness, and roughness are independent parameters describing particle shape. For instance, Cho et al. (2006) states that round particles can be non-spherical, and equidimensional particles can be very angular. Sphericity and roundness can be estimated qualitatively by comparing features of individual grains to common particle geometries presented in visual charts (e.g., Powers, 1953; Krumbein and Sloss, 1963). The micro-scale of roughness makes the measurement difficult (Santamarina and Cho, 2004; Cho et al., 2006). Computer analysis of particle shape data obtained by digital imaging can also be used to systematically determine shape parameters. Comparing direct measurement of particle features via fitted spheres provides a quantitative method to determine roundness and sphericity. It is common to use a two-dimension particle image projection and measures of fitted circles to determine roundness and sphericity values. Figure 2.3 shows circles fit to a particle image projection. From the dimensions of the circles shown, one definition for sphericity is the inscribed circle sphericity, which is defined as the ratio of the radius of the largest inscribed circle, $r_{max-insc}$, to the radius of the smallest circumscribed

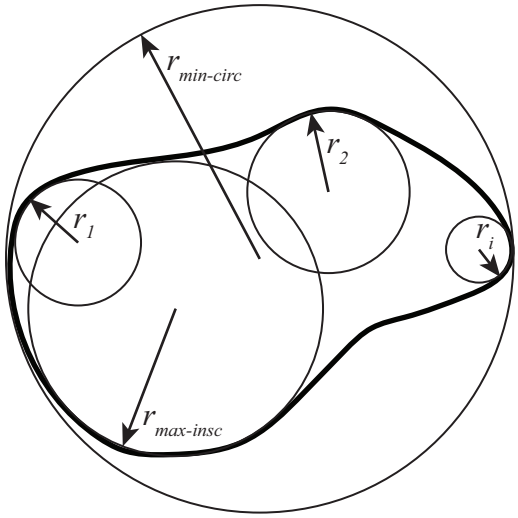

Figure 2.3: Particle shape measurements (modified after Cho et al., 2006).

circle, $r_{min-circ}$ (Santamarina et al., 2001). Roundness can be estimated as the ratio of average surface feature curvature radii, $\bar{r_i}$, to the radius of the maximum sphere (or circle for two-dimensional projections), $r_{max-insc}$, that can be inscribed within the particle (Santamarina et al., 2001).

Mathematical techniques, such as the Fourier series, can be used to approximate the surface profile of a particle and characterize the shape in more detail (Schwarcz and Shane, 1969; Santamarina et al., 2001; Santamarina and Cho, 2004; Mitchell and Soga, 2005; Cho et al., 2006). A soil particle can be modeled as a fitted ellipse by minimizing the distance between the vertex points of the particle image projection and an ellipse in the form of a quadratic curve (detailed coding of this processes provided in Simpson, 2014). The aspect ratio (minor axis length to major axis length) of the fitted ellipses also provide a measure of particle sphericity (Schwarcz and Shane, 1969). Santamarina and Cho (2004) states that the method used to define sphericity

and roundness does not greatly impact the results. Specifically, the values determined with various methods are thought to agree within values of 0.1, not exceeding 0.2 (for methods that produce roundness and sphericity values from zero to one). The authors state that the uncertainty introduced by classifying particle shape with different methods, or operator bias, does not exceed the variability of particle shapes present within most sand samples. Several applications of modern technology are becoming applicable for particle shape analyses. Hryciw et al. (2014) details the usefulness and importance of modern particle shape analyses.

The literature detailing Fourier analyses for particle shape determination do not appear to produce comparable results to the r and s values determined with other methods noted (e.g., visual classification chart estimations, measurement of fitted circles to the particle perimeter and surface features). As discussed by Schwarcz and Shane (1969), there is a somewhat subjective selection of the particle center for the Fourier method, and sphericity estimation values increase as the particle departs from spherical shape, which is contradictory to other methods in which a spherical shape produces the maximum sphericity value of one. Four roundness estimations are detailed with the Fourier method. There are also noted challenges of sphericity features affecting roundness estimations, which should be independent measures, however this limitation may be present in other methods as well.

Particle shape analysis can lead to the estimation of many other properties of the sediment. If a sufficient number of particles from a sample are analyzed, an estimation of the grain-size distribution can be approximated (e.g., Simpson and Evans, 2015). Ellipses fit to the analyzed particles projection outlines can be rotated around the

major or minor axes to create prolate or oblate spheroids, respectively. Masses can be assigned to the ellipsoids based on the respective volumes and the specific gravity (density of particle solids) to create a distribution of particle sizes by mass, similar to the process of a sieve analysis. The size of the ellipsoidal models can be defined in various ways, and it is important to match the respective size that would be determined with sieve analyses (Hryciw et al., 2014). An equivalent sieve opening size, d_{equiv}, for ellipsoidal models has been determined as,

$$d_{equiv} = \sqrt{(d_1^2 + d_2^2)/2}, \tag{2.3}$$

where d_1 and d_2 are the major and minor axis diameters, respectively (Hryciw et al., 2014; Simpson and Evans, 2015).

The dimensionless roundness parameter has been used to estimate the range of packing densities of a collection of soil. Santamarina and Cho (2004) cite the relationship developed by Youd (1973), defined as,

$$e_{max} = 0.554 + 0.154r^{-1}, \qquad e_{min} = 0.359 + 0.082r^{-1}, \tag{2.4}$$

where e_{max} and e_{min} are the maximum and minimum void ratios, respectively (discussed in more detail in §2.2.3). Equation 2.4 assumes that the coefficient of uniformity is $C_u = 1$. The correlation given in Equation 2.4 shows that attainable limiting void ratios (i.e., packing densities of the collection of soil) are affected by particle shape. Limiting void ratios increase with a decrease in roundness and sphericity. (Santamarina and Cho, 2004; Cho et al., 2006).

Several researchers have developed relationships comparing particle shape to the shear strength of a soil through the friction angle. The critical state friction angle predicted from shape has been calibrated with laboratory test results (e.g., angle of repose, friction angles from drained triaxial test) (Santamarina and Cho, 2004; Mitchell and Soga, 2005). It is hypothesized that the friction angle will increase with increased angularity and roughness due to the added difficulty of particle rotation and hindered slippage. Dilatancy is an important component of shear strength, which will be discussed herein, and angularity and roughness contribute to dilatancy and anisotropy (Santamarina and Cho, 2004). Santamarina and Cho (2004) provides a direct relationship that estimates the critical state friction angle, ϕ'_{cs}, by,

$$\phi'_{cs} = 42^\circ - 17^\circ r. \tag{2.5}$$

2.2.3 Packing Density

Particle size, gradation, and shape, affect the limiting packing densities for a collection of soil, which influence the mechanical response. To quantify the limiting packing arrangements and determine the density state of a sediment, the specific gravity, G_s, must be determined. Specific gravity is the ratio of the unit masses of soil solids and water, and provides a measure of the density of particle solids for a collection of soil (Bardet, 1997). ASTM D854-10 (2010) details the procedures for determining G_s. The test results are very sensitive to temperature, water quality, and volume and mass measurements. Calibration of pycnometers filled only with pure water is

performed to improve the accuracy of the results. For a triplicate test performed by a single operator within the same laboratory, the acceptable range for two resulting G_s values is 0.02 for sandy soils. The average value for poorly graded sand reported within ASTM D854-10 (2010) is $G_s = 2.66$. As stated by (Coduto, 2001, pg. 50), "it is usually not necessary to measure the specific gravity of solids, G_s. For most projects, we can assume $G_s = 2.65$ for clays or 2.70 for sands. . . ." Other examples of typical measured of specific gravity were noted in the literature studied herein. Beach sands investigated in Rousé (2014) have $G_s = 2.64$ and 2.68, Toyoura sand used in studies performed by Fukushima and Tatsuoka (1984) and Tatsuoka et al. (1986) has $G_s = 2.64$, and Southport sand used in the investigation by Holubec and D'Appolonia (1973) has $G_s = 2.68$. The specific gravities for the variety of beach sands noted agree well with the range of approximately $G_s = 2.65$ to 2.7 suggested by Coduto (2001).

Once the specific gravity of soil solids has been determined, other phase relationships for a collection of soil may be defined. As noted, the limiting packing densities, or void ratios, must be determined to prepare specimens of a known density state. Void ratio, porosity, and the relation between the two are defined as,

$$e = \frac{V_v}{V_s}, \qquad n = \frac{V_v}{V_t}, \qquad n = \frac{e}{1+e}, \tag{2.6}$$

respectively, where for a given specimen V_v is the volume of voids, V_s is the volume of solids, and V_t is the total volume. Void ratio and porosity may be determined by filling a container of a known volume with a known mass of sediment, so that the

mass of the solids, m_s, and V_t are defined. V_s can be calculated through through m_s and G_s, and the difference between V_t and V_s is V_v.

ASTM D4254-16 (2016) and ASTM D4253-16 (2016) detail the standardized procedures to determine the maximum and minimum void ratios, e_{max} and e_{min}, respectively. The maximum void ratio identifies the loosest packing arrangement of a sediment of interest, and the minimum void ratio identifies the densest packing arrangement. It is important to note that the limiting void ratios define the repeatable values of e_{max} and e_{min} by following the standardized procedures, and may not be the absolute loosest and densest possible arrangements of the particulate investigated. The minimum void ratio is a difficult parameter to obtain correctly by standard procedures. ASTM D4253-16 (2016) specifies that a soil mold with an even surcharge applied be agitated with a vibratory table to produce the dense packing arrangement.

Uniformly graded soils tend to have a narrower range of possible densities compared to well-graded soils (Mitchell and Soga, 2005). Various developed test methods can produce different limiting void ratios. Holubec and D'Appolonia (1973) provides a study of the minimum and maximum void ratios for various sands. As an example, for Southport sand, Holubec and D'Appolonia (1973) determines $e_{max} = 0.88$, and e_{min} is determined with two methods. In the first method, vibration is applied to the the mold filled with sand by horizontal tapping, with the resulting $e_{min} = 0.624$. In the second method, the modified proctor compaction method is used (similar to the ASTM D4253-16 (2016) procedures), with the resulting $e_{min} = 0.530$. Notably, for the variety of sands investigated by (Holubec and D'Appolonia, 1973), the values from different methods for determining e_{min} do not vary more than 0.1.

The limiting void ratios allow density classes to be defined for a sediment of interest (Mitchell and Soga, 2005). The relative density, D_r, is a measure of the current void ratio in relation to the maximum and minimum void ratios defined as,

$$D_r = \frac{e_{max} - e}{e_{max} - e_{min}} \times 100\%, \tag{2.7}$$

where e is the void ratio of interest for the prepared sediment state.

Typical porosities of surficial natural beach sands have been found to range from $n = 0.39$ to 0.49. For instance, Atkins and McBride (1992) determine the average porosity of beach sands by investigating the (difficult to determine) in situ state of various sands. The average porosity of beach sands is summarized as $n = 0.47$ in the respective study. Seventy-three percent of the sands investigated had a range of porosities between $n = 0.41$ to 0.50. If the assumption is made that this was near the extreme minimum and maximum packing densities of the sands investigated (or at least provides a range of loose to dense beach sand arrangements), then a typical medium relative density is likely for the studied beaches. The authors noted that even beaches trampled by people exhibited similar in situ states as beaches that had not been frequently disturbed. It should be noted that a full investigation of the sands reported was not performed, including standardized minimum and maximum void ratio testing, or shape and gradation classification; therefore, robust comparisons of the results of Atkins and McBride (1992) to other sands of interest is limited.

2.3 Mechanical Behavior of Granular Sediment

Forces between interparticle contacts govern the shear strength of granular material (Rowe, 1962; Lee and Seed, 1967; Terzaghi et al., 1996). In a geotechnical laboratory, the strength of sediment is typically measured with compression shear testing. Herein, typical testing equipment was employed to determine the shear strength of the South Beach, Newport, Oregon sediment (e.g., triaxial and simple shear testing) in addition to less standardized tests that investigate the response of surficial particulate. Low confinement simple shear tests were performed in an attempt to relate the results of the typical shear strength testing to the surficial response of the beach sediment. The subsequent discussions provide background information regarding strength characteristics for granular sediment under drained conditions [i.e., no generation of excess pore-water pressure; drained conditions are denoted with the prime symbol ($'$)], triaxial and simple shear testing, and surface particle testing (i.e., angle of repose and pocket-friction angle). The understanding of the respective background information is useful for interpreting the results presented in Chapter 3, as well as understanding the conclusions drawn in Chapter 4.

The shear strength of sands and other granular material has been studied in great detail and presented in seminal geotechnical literature (e.g., Lee and Seed, 1967; Lambe and Whitman, 1969; Terzaghi et al., 1996; Holtz et al., 2011). If the mechanism of particle crushing is neglected, which is appropriate at low confining pressures, then the strength of sand can be attributed to three sources: sliding friction, particle rearranging, and dilation (Rowe, 1962; Lee and Seed, 1967; Terzaghi et al.,

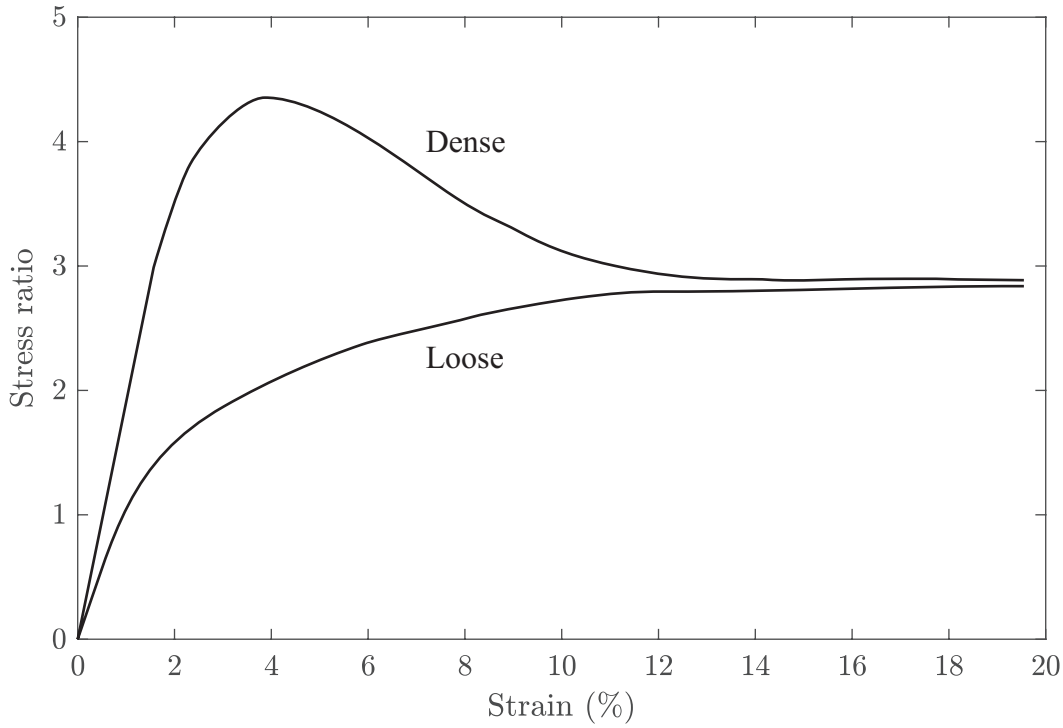

Figure 2.4: Generic plot showing the typical loose and dense shearing response expected of sand.

1996; Mitchell and Soga, 2005). Dense arrangements of sand exhibit a peak shear stress during shearing followed by post-peak softening until a constant shear stress is reached with continued shearing. Loose arrangements of sand mobilize shear strength, at a slower rate than dense sands, until a maximum shear stress is achieved and then maintained with continued shearing. The corresponding volume changes during a drained shearing response generally show dilation and contraction for dense and loose arrangements of sand, respectively. Figure 2.4 shows a generalized plot that demonstrates the loading response trends described during shearing of dense and loose sands. Similarly, Figure 2.5 shows a generalized plot demonstrating the volumetric

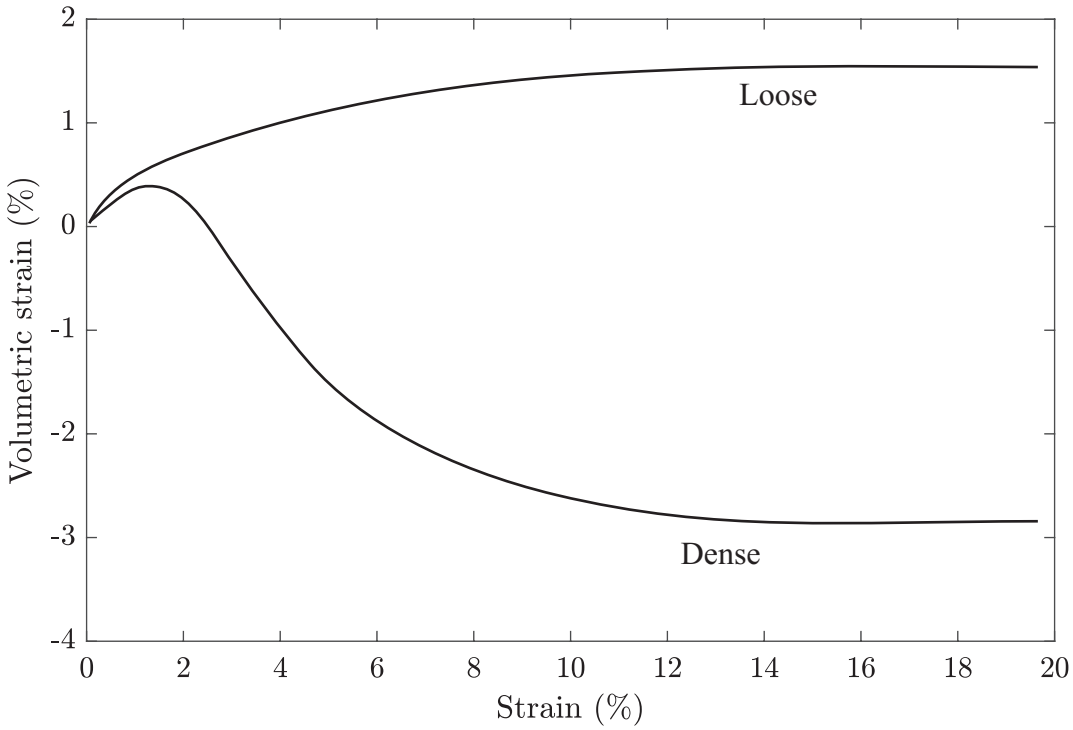

Figure 2.5: Generic plot showing the typical loose and dense volumetric response expected of sand during drained loading.

response trends expected during the drained loading of dense and loose sands.

The stress ratio on the y-axis of Figure 2.4 can be defined in several ways, all of which produce similar trends as depicted. For consolidated drained (CD) triaxial compression testing, the stress ratio is commonly defined as the normalized deviatoric stress, q'/σ'_3, where $q' = \sigma'_1 - \sigma'_3$, and σ'_1 and σ'_3 are the major and minor principal stresses, respectively. The strain on the x-axis of Figure 2.4 for triaxial tests is typically shown as the axial (major principal) strain, ε_1, defined as the ratio of the change in the specimen height to the initial height (see Figure 2.8 for the loading and displacement schematic of the CD triaxial compression test). For other CD shearing

tests, such as direct shear or simple shear tests, the shear stress, τ', is measured directly. The stress ratio on the y-axis of Figure 2.4 is defined as the shear stress normalized by the the vertical effective stress, σ'_v. The strain on the x-axis is the shear strain, γ, defined as the ratio of the horizontal displacement to the initial specimen height (see Figure 2.9 for the loading and displacement schematic of the simple shear test).

At a certain strain value, dense and loose arrangements of sand will approach roughly the same stress ratio, indicating that the specimen has reached critical state. The initial state of a specimen has little influence on the shear strength of the sediment at critical state (Sadrekarimi and Olson, 2011). At critical state, volumetric strains also approach a constant value, indicating negligible volume change of the specimen with continued shearing. The critical state of shearing resistance of a soil is primarily governed by the particle mineralogy and shape (Bardet, 1997; Sadrekarimi and Olson, 2011).

The friction angle is a common parameter used to define the shear strength of soil. The friction angle defines the slope of the failure envelope in the Mohr-Coulomb failure criterion (Holtz et al., 2011). When considering the effective, or drained, response of soil to perturbation, the friction angle, ϕ', defines the linearly proportional relationship between shear and normal stress by,

$$\tau' = \sigma' \tan \phi', \tag{2.8}$$

for a granular material with no apparent cohesion intercept, where τ' is shear stress

and σ' is effective normal, mean, or confining stress at a given state of interest during shearing. Equation 2.8 indicates that an increase in effective stress provides an increase in the available capacity of mobilized shear stress. The friction angle at critical state can be determined experimentally for a soil within a margin of about one degree, as stated by Bolton (1986). The investigation performed in Bolton (1986) shows that for a variety of sands, the typical range of the critical state friction angle is between 32° and 37°.

Geotechnical laboratory testing can be performed to determine the shear strength of soils at various degrees of specimen saturation. It is important to consider the effects of saturation when comparing the results of different testing procedures. Skinner (1969) shows that wet particles have higher measures of interparticle friction than dry particles, when investigating glass and steel spheres. Although the interparticle friction may be different for wet and dry particles, there is not a defined alteration of the friction angle for a collection of dry or wet particles. The mechanisms of shearing changes between rolling and sliding particles as interparticle friction changes, whichever offers the least resistance. Sadrekarimi and Olson (2011) found only slight differences in the resulting friction angle of the granular sediment during dry and wet (saturated) shear strength testing. Bishop and Henkel (1962) notes that the friction angle resulting from dry triaxial test results may be only slightly larger than that of fully saturated triaxial test results. The preceding findings justify the conclusions that the friction angle resulting from dry and saturated geotechnical shear strength tests should be comparable.

The interparticle friction angle governs the contribution of sliding friction, ϕ'_μ,

to the overall shear strength of sand. The interparticle friction angle is dependent on particle mineralogy (Mitchell and Soga, 2005). For quartz particles, which are a common sand constituent, the typical range of sliding friction angle is $\phi'_\mu = 22^\circ$ to 35° (Terzaghi et al., 1996; Mitchell and Soga, 2005). As discussed, the remaining portion of the mobilized friction angle of a collection of soil is due to particle rearranging, ϕ'_r, and dilation, ϕ'_d, angles of friction; i.e.,

$$\phi' = \phi'_\mu + \phi'_r + \phi'_d. \tag{2.9}$$

The contribution of the particle rearrangement is typically $\phi'_r = 5^\circ$ to 6° (Terzaghi et al., 1996). The critical state, or constant volume, friction angle, ϕ'_{cs}, contains no dilative effects; i.e.,

$$\phi'_{cs} = \phi'_\mu + \phi'_r. \tag{2.10}$$

Unlike the critical state friction angle, the dilation angle is not a constant value for a collection of soil, because it is a function of packing density and confining pressure (Bolton, 1986). Mitchell and Soga (2005) states that continuum mechanics assumes forces transmit uniformly through a homogeneous granular material; however, interparticle force distributions are not homogeneous. The mobilized friction angle defined as the summation provided in Equation 2.9 is a simplification to estimate the magnitude of the contributing resistance mechanisms. Equation 2.9 possesses inherent uncertainty as a result of the inhomogeneous interparticle force distributions during loading of a collection of soil particles.

As previously discussed, dilatant behavior is typically observed in the shearing

response of dense sand. In a notable study of strength and dilatancy of sands, Bolton (1986) shows that the peak friction angle of soil, which is determined from the maximum stress ratio of the response, usually coincides with the maximum rate of dilation. The maximum rate of dilation is defined as $(-d\varepsilon_v/d\varepsilon_1)_{max}$, where ε_v is the volumetric strain and ε_1 is the major principal strain. The maximum rate of dilation can be observed in the volumetric response of specimens during shearing as the maximum slope of the curve, corresponding to the peak stress state. The empirical relationship developed by Bolton (1986), named the relative dilatancy index, I_R, relates density and stress state to dilation potential by,

$$I_R = I_D \left(Q - \ln \frac{p'}{p_{ref}} \right) - R, \tag{2.11}$$

where I_D is the relative density index ($D_r/100$), p' is the mean effective stress at failure, p_{ref} is 1 kPa, and Q and R are fitting coefficients. Values of $Q = 10$ and $R = 1$ fit the data set presented within Bolton (1986) well, and provides the limiting values of $0 < I_R < 4$. The relative dilatancy index is used to determine the difference between the peak, ϕ'_p, and critical state friction angles by $\phi'_p - \phi'_{cs} = 5I_R$ for plane strain conditions and $\phi'_p - \phi'_{cs} = 3I_R$ for triaxial strain conditions. The relationships are shown by Bolton (1986) to be accurate within about 2° for the sands investigated between mean effective stress levels of $p' = 100$ to 1000 kPa.

Similar to the shearing response of dense sands under typical geotechnical confining pressures, loose sands sheared under low confining pressures may dilate (Ponce and Bell, 1971). There is some consensus in the literature that the friction angle of sand

at any density state increases at very low confining pressures. However, researchers have speculated various magnitudes of the contributing mechanisms that produce the increased friction angle (e.g., Ponce and Bell, 1971; Fukushima and Tatsuoka, 1984; Sture et al., 1998; Chakraborty and Salgado, 2010; Sadrekarimi and Olson, 2011).

During low confinement testing, factors must be considered that would not typically be accounted for in tests performed under typical geotechnical confining pressures. For instance, Ponce and Bell (1971) present CD triaxial compression tests performed on poorly graded sand ($d_{50} \approx 0.45$ mm) under very low confining pressures, which account for the effects of membrane strength, strain rate, specimen self-weight, and frictional resistance of the loading piston. The outcomes of the Ponce and Bell (1971) study show that the sand sheared under low confining pressures [down to approximately $\sigma_3' = 1.4$ kPa (0.2 psi)], produced a principal stress ratio at failure (the maximum principal stress ratio, $(\sigma_1'/\sigma_3')_{max}$) of nearly double that of the typical confining pressure tests [between approximately $\sigma_3' = 35$ kPa (5 psi) and $\sigma_3' = 240$ kPa (35 psi)]. The noted trend is observed for the range of packing densities investigated, from very loose to dense arrangements (see Figure 5 within Ponce and Bell (1971) for more detailed results of the respective study). The only variable meant to affect the shearing response in the respective study is the change in confining pressure, and the increase in stress ratio is initially attributed by the authors to effects of an apparent cohesion intercept changing with confining pressure.

Ponce and Bell (1971) also interprets the maximum principal stress ratios as resulting peak friction angles neglecting the possible contribution of apparent cohesion. Following the assumption of neglecting the apparent cohesion intercept, Ponce and

Bell (1971) modify the trend of dilatancy expected for sand under extremely low confining pressures with respect to the trend defined by Rowe (1962) under typical confining pressures. Figure 2.6 shows the expected contributions of dilatancy, particle rearrangement, and sliding friction to the peak friction angle at either typical ($\sigma'_3 \approx 200$ kPa) or extremely low ($\sigma'_3 \approx 1.4$ kPa) confining pressures, as a function of relative density. An additional trend postulated by Ponce and Bell (1971), is that loose sand sheared under extremely low confining pressures exhibits a decrease in particle rearranging as dilation increases. This hypothesis is somewhat contradictory to trends shown in Figure 2.6, which the authors note are overly simplified, because the decrease of particle rearrangement at extremely low confining pressures is not depicted for the low relative densities. Figure 2.7 shows a summarizing schematic for the contributions to the friction angle for loose sand with decreasing confining pressure. Figure 2.7 defines the friction angle for the loose sand investigated as $\phi'_{cs} = 30°$ under typical confining pressures with no dilatant behavior observed. The friction angle then increases to a projected peak value of about $\phi'_p = 45°$ for negligible confining pressures. The mechanism causing the observed increase in peak friction angle is explained by the increased dilatancy effects of the loose sand sheared under low confining pressures. The theory that the contribution of particle rearranging decreases under low confinement indicates a complimentary decrease in the critical state friction angle, as depicted in Figure 2.7. The critical state friction angle is predicted by the authors to approach the sliding friction angle at negligible confining pressures.

Similar to the work of Ponce and Bell (1971), Stroud (1971) presents results of low confinement tests on sand, but performed in a fully instrumented Cambridge

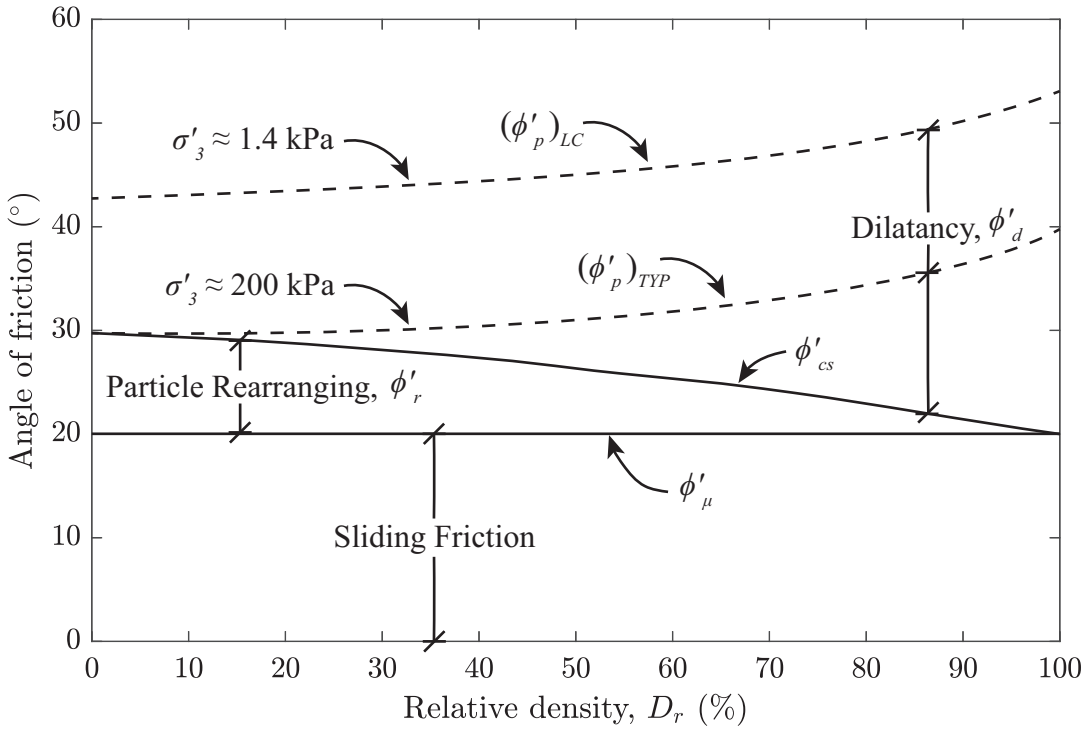

Figure 2.6: Components of shear strength for sand at typical and low confinement. Mobilized shear strength mechanisms, defined as friction angles, are presented (modified after Rowe, 1962; Ponce and Bell, 1971). Sliding friction and particle rearrangement are shown to be applicable for low or typical confining pressures, but the dilatancy component varies with confinement. The peak friction angle at typical confining pressures, $(\phi'_p)_{TYP}$, is said by Rowe (1962) to be the same as the critical state friction angle for loose sand (low relative densities of about $D_r = 0$ to 35%) and increases as relative density increases. The peak friction angle for extremely low confining pressures, $(\phi'_p)_{LC}$ is thought by Ponce and Bell (1971) to be $\approx 15°$ greater than the critical state friction angle for loose sand in the respective study and continues to increase as relative density increases. The curves representing $(\phi'_p)_{TYP}$ and $(\phi'_p)_{LC}$ are roughly parallel.

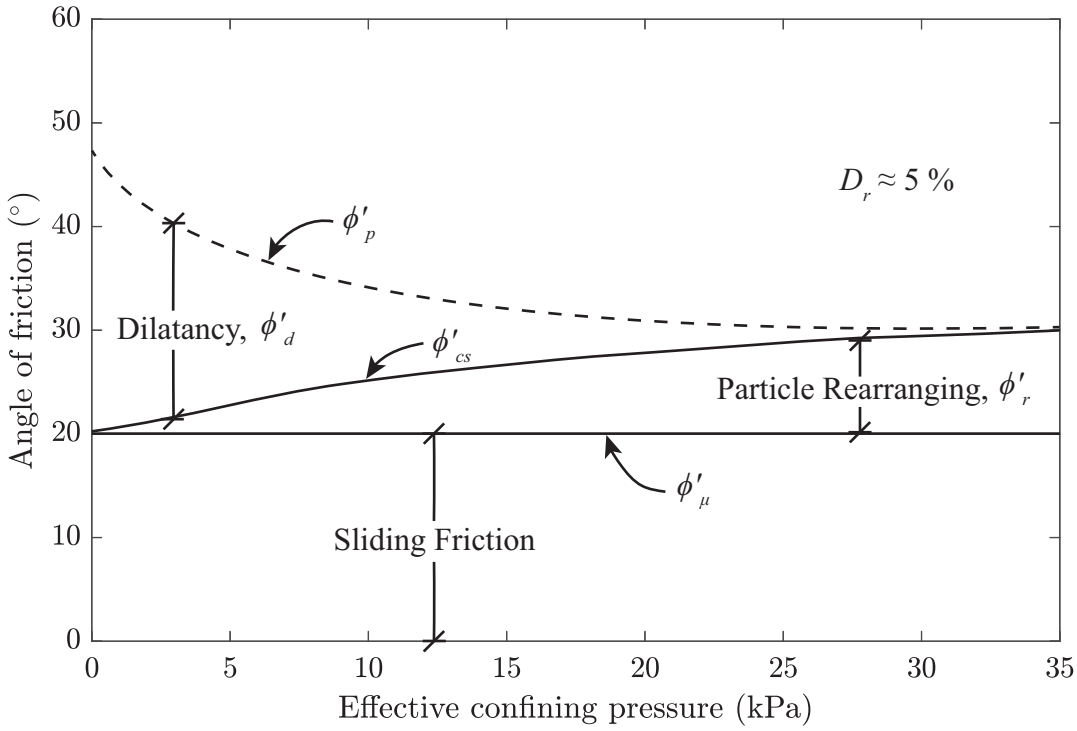

Figure 2.7: Components of strength of loose sand at decreasing confining pressures (after Ponce and Bell, 1971).

simple shear apparatus (i.e., a rectangular prism specimen). The dry sand utilized in the study ($d_{50} \approx 1$ mm) also portrays altered behavior when sheared under low confining pressures [down to approximately $\sigma'_v = 12$ kPa (1.7 psi)]. The shearing response of the sand shows a steeper increase of the stress ratio when sheared under low confining pressures, indicating an increase in stiffness of the sand specimen. The increase in soil stiffness at low confinement is also noted by Sture et al. (1998) from the results of low confinement triaxial tests on Ottawa quartz sand. The volumetric response of the sand investigated by Stroud (1971) shows that at shear strains as high as 50%, critical state is not yet achieved and dilation continues to occur as the sand

shears. Stroud (1971) states that specimens sheared under low confining pressures dilate further to reach critical state. The dependence of friction angle on confining pressures determined by Stroud (1971) is not as great as that found by Ponce and Bell (1971) for the range of confining pressures investigated.

The proposed conclusions of Ponce and Bell (1971) contributed to the motivation for Fukushima and Tatsuoka (1984) to perform low confinement CD triaxial tests on a different sand. Poorly graded, angular Toyoura sand is investigated in the respective study (d_{50} = 0.16 mm). Fukushima and Tatsuoka (1984) details the challenges of interpreting results from strength testing performed with low confining pressures that appear to have either large variations in apparent cohesion or friction angle over the transition between typical to low confining pressures. The respective study aims to further investigate and clarify low confinement shearing results on sands. The outcomes of the study show much different trends than those determined by Ponce and Bell (1971). With careful testing employed to limit adverse effects and corrections applied that account for membrane strength, self-weight, and other unintended forces, the authors find only a slight difference in the peak friction angle derived from typical to low confinement shearing responses. The uncorrected results show a difference in peak friction angle of about 5° to 8° for the loose and dense sand, respectively, for tests performed under typical ($\sigma_3' \approx 400$ kPa) to low ($\sigma_3' \approx 5$ kPa) confining pressures. Upon applying various correction to the results, a difference in peak friction angle of only 2° and 5° for loose and dense arrangements of sand is found, respectively, for the defined confining pressure range. The authors concluded that although there were small changes in the friction angle of the tested Toyoura sand over the transition from

typical to low confining pressures, no further changes were noted in friction angle or volumetric behavior for tests with confining pressures below about $\sigma'_3 = 50$ kPa.

The trends observed in the low confinement CD triaxial test results between Ponce and Bell (1971) and Fukushima and Tatsuoka (1984) are considerably different. The disagreement in trends can not be easily explained, and may be due to variations within the testing programs, or the differences could truly be attributed to the unique response of the specific materials under such low confinement. Importantly, Fukushima and Tatsuoka (1984) suggests that low confinement strength testing be performed for the sediment of interest, because the change in friction angle at these pressures is unpredictable and may vary greatly, even between comparable soils.

Sadrekarimi and Olson (2011) presents consolidated drained and undrained triaxial compression and constant volume and drained ring shear test results on three types of sand. The authors utilize the ring shear tests to apply large shear strains to the sand specimens and observe critical state behavior. The respective study shows that under the lowest confining pressures employed ($\sigma'_v \approx 30$ kPa), the critical state friction angle of the three sands investigated was notably larger. Below about $\sigma'_v \approx 100$ kPa, the critical state friction angle appears to be stress dependent. Sadrekarimi and Olson (2011) postulate that the increase in the critical state friction angle at low confining pressures is due to increased particle interlocking.

The noted works of low confinement behavior of the shearing response of sand stand as an example for possible trends observed and expose the challenges with geotechnical shearing tests with low confining pressures. From these works, it is

evident that the results are not straightforward. Different sands are thought to exhibit different responses when sheared under low confining pressures and the methods of analysis and correction may be very influential on the results.

Although the low confinement behavior of sands from previous works may not be consistent or considered predictable from the previous investigations in the literature, Chakraborty and Salgado (2010) analyzes the test results from studies by Fukushima and Tatsuoka (1984) and Tatsuoka et al. (1986) for low confinement triaxial and plane strain test data, respectively, to "quantify the dependence of dilatancy and friction angle on relative density and confining stress," extended to low confinement results (Chakraborty and Salgado, 2010, pg. 527). The relationship developed by Chakraborty and Salgado (2010) serves as a tool to predict the response of dilatant behavior at low confinements, much like Bolton (1986) has done for typical confining pressures in Equation 2.11. The relationship developed by Chakraborty and Salgado (2010), which is applicable for low confinement results, is given as,

$$\frac{\phi'_p - \phi'_{cs}}{3.8} + I_D \ln \frac{p'}{p_{ref}} = I_D Q - R, \tag{2.12}$$

where the parameters are the same as those presented by Bolton (1986). Chakraborty and Salgado (2010) assumed two different critical state friction angles as a constant value for all confining stress for triaxial and plane strain conditions. Similarly, Equation 2.12 assumes that the effects of low confinement are all captured with the peak friction angle.

In addition to observing shear strength and volumetric responses to understand

sediment behavior during shearing, estimated elastic relationships can be investigated (Bardet, 1997; Holtz et al., 2011). If a collection of soil particles are assumed to be elastic, then isotropic linearly-elastic stress-strain relationships can be estimated that describe the deformation of the sediment prior to failure. There are multiple types of moduli that define the stiffness of sediment, which are a part of the material's constitutive relations (Holtz et al., 2011). The modulus of elasticity (also known as Young's modulus), E, defines the relationship between normal stress and strain. Similarly, the shear modulus, G, defines the relationship between shear stress and strain. The modulus of elasticity and the shear modulus are related through Poisson's ratio, ν, which defines the relationship between axial and volumetric strains (Bardet, 1997). The constrained modulus, D, is the ratio of axial stress to axial strain for confined compression (Lambe and Whitman, 1969), and is defined as,

$$D = \frac{E(1-\nu)}{(1+\nu)(1-2\nu)}. \tag{2.13}$$

Initial and secant moduli can be determined from laboratory strength testing data. Typically, the slope of the tangent line of the initial portion of the response determines initial moduli, and the slope the secant line between the origin and a defined point of the response determines secant moduli. For example, a common secant modulus of elasticity, E_{50}, is determined from the slope of the secant line of stress-strain curve at from the origin to 50% of the maximum stress measured during the shearing of the soil (Holtz et al., 2011). For loose to dense sands, the modulus of elasticity normalized by atmospheric pressure ranges from about 100 to 1000 ($\approx$10

to 100 MPa) and Poisson's ratio ranges from about 0.2 to 0.4 (Bardet, 1997; Holtz et al., 2011). Values of elastic moduli are sensitive, because soil fabric is not truly elastic, so methods to obtain elastic estimations from the sediment loading response should be clearly detailed. Vucetic (1994) presents a study on threshold strains for the cyclic response of soils and shows that sandy sediments typically have threshold strains from about 0.01 to 0.03% upon which the response transitions from elastic to inelastic. The small strain thresholds presented by Vucetic (1994) are difficult to enforce for actual laboratory data to estimate elastic moduli, and larger strains are typically employed to obtain the estimated parameters. It should also be noted that the boundary strains measured during lab testing can lead to underestimations of soil stiffness (Holtz et al., 2011).

The consolidation of triaxial and simple shear devices are different and likely produce different initial stresses within the soil (e.g., isotropic consolidation versus K_0 consolidation, respectively). Several studies have determined the results of elastic moduli of sand tested in triaxial and simple shear apparatuses (Stroud, 1971; Rossato and Simonini, 1991). Soil stiffness typically increases with confining pressure. Rossato and Simonini (1991) shows that by employing the elastic relationship between E and G, as provided in Bardet (1997),

$$E = 2G(1 + \nu), \tag{2.14}$$

the ratio of G/E should theoretically be a constant value for a given value of ν. The respective data analyzed show that at certain strains, G/E produces the expected

constant value, occurring at lower strains for tests with lower confining pressures (e.g., around $\varepsilon_1 = 0.2\%$ for a vertical effective stress of 98 kPa in comparison with around $\varepsilon_1 = 0.7\%$ for a vertical effective stress of 392 kPa). Before the strains reach the expected trend, G is lower than the corresponding E expected. From the small strains of $\varepsilon_1 = 0.1$ to 1.0 %, the range of G/E did not vary over a range of more than 0.5, showing a small range for estimated elastic relationships through Equation 2.14. The study by Rossato and Simonini (1991) helps to demonstrate the degree of accuracy expected of Equation 2.14.

2.3.1 Triaxial Testing

The triaxial test is a popular strength test for soils. The details of specimen preparation and performance of the triaxial test are well established in the literature (e.g., Bishop and Henkel, 1962; Bardet, 1997; Head, 1998). Cylindrical specimens are tested in the triaxial device. The minimum recommended specimen diameter is 33 mm and the height to diameter ratio should be between 2 and 2.5. For a dry uniform sand, the specimen may be placed by air pluviation by pouring through a funnel then vibrated to obtain a greater density by gently tapping the side of the mold, as performed by Ponce and Bell (1971), similar to reconstituted triaxial specimen preparation recommended in ASTM D7181-11 (2011). Vacuum pressure ($\approx$ 35 kPa) is then applied to the specimen to stabilize the dry sand when the mold is removed to avoid slumping.

The specimen can be isotropically consolidated so that the cell pressure is equally applied all around the specimen. The effective confining pressure is defined as σ_3'.

During a consolidated drained (CD) strain-controlled triaxial test, the deviatoric stress, q', increases due to the the increase in axial stress (major principal stress), σ'_1, while the effective confining stress (minor principal stress), σ'_3, is kept constant by allowing volume change within the specimen and the cell. Drainage can be controlled with the triaxial testing apparatus and measurements of pressure and volume change can be obtained throughout the test. The axial strain rate should be sufficiently slow to ensure no excess pore-water pressure is generated within the specimen during shearing.

A standardized procedure for the CD triaxial compression test is provided by ASTM D7181-11 (2011). The loading and displacement mechanisms of the triaxial testing apparatus are shown in Figure 2.8. The axial (major principal) and volumetric strains throughout the shearing phase of CD triaxial compression tests are defined as,

$$\varepsilon_1 = \frac{\Delta h}{h_c}, \qquad \varepsilon_v = \frac{\Delta V}{V_c}, \tag{2.15}$$

respectively, where h_c is the height of the specimen after consolidation, Δh is the change in height of the specimen (positive for decreasing specimen height during shearing), V_c is the volume of the specimen after consolidation, and ΔV is the change in volume of the specimen (positive for decreasing specimen volume during shearing, i.e., contraction) (ASTM D7181-11, 2011). Holtz et al. (2011) shows that the friction angle can be determined from triaxial test results by developing Mohr circles, or by

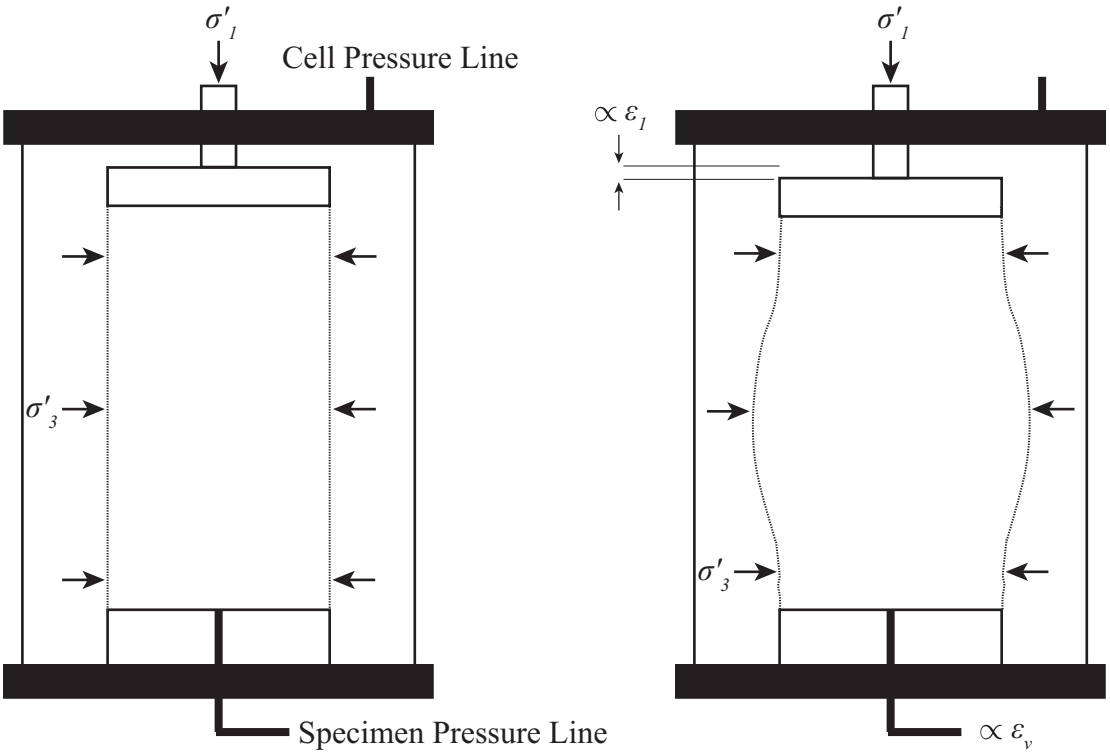

Figure 2.8: CD triaxial compression test loading schematic. The figure on the left shows the consolidated specimen prior to shearing ($\sigma'_1 = \sigma'_3$ for isotropic consolidation). The deformations during shearing shown in the right figure are measured through axial or volumetric strains, shown as proportional to the respective dimensions.

calculating ϕ' from stress obliquity relations (differences between σ'_1 and σ'_3), by,

$$\sin \phi' = \frac{\sigma'_1 - \sigma'_3}{\sigma'_1 + \sigma'_3}. \tag{2.16}$$

An important factor in triaxial testing is the degree of saturation of the specimen. The presence of air within the system decreases the accuracy of pressure and volume regulation and measurement (Skempton, 1954; Bishop and Henkel, 1962; Black and

Lee, 1973; Head, 1998). Initially, saturation should be improved by flowing deaired water through the system under vacuum pressure (Head, 1998). Skempton's B value (Skempton, 1954) aims to determine the degree of saturation within the specimen, defined as,

$$B = \frac{\Delta u}{\Delta \sigma_3}, \tag{2.17}$$

where u is the specimen pore-water pressure and σ_3 is the total confining stress, or triaxial cell pressure. To perform a B value check, the specimen drainage valves are closed and the cell pressure is increased by an incremental value [typical values of $\Delta\sigma_3$ are approximately equal to 70 kPa (ASTM D7181-11, 2011)] and Δu is measured. If the change in cell and specimen pressure are equal, the B value will equal one, indicating full specimen saturation. If the B value is less than one, the specimen may not be completely saturated. For soft soils, $B = 0.95$ would realistically indicate approximately 97% saturation. Confining pressures applied to a soil specimen create a stiffer soil fabric; stiffer soil (such as sands) could have a measured $B = 0.69$, but the degree of saturation may be up to 99.5% (Black and Lee, 1973). As implied, the B is dependent on the amount of air within a soil specimen. Once initial flushing of the specimen with deaired water has been performed, further saturation efforts aim to dissolve the remaining air bubbles into solution. Dissolving air into solution is a function of time and pressure (Black and Lee, 1973). Black and Lee (1973) shows that increasing back pressure (i.e., increasing absolute specimen and cell pressure simultaneously to maintain a constant effective stress) aides in producing a higher degree of specimen saturation. To determine if the degree of saturation is sufficient

prior to the shearing phase of a triaxial test, the B value check should be performed and, if a value of one is not achieved, the check should return the same B value with subsequent cell pressure increases to be determined as sufficient (Head, 1998).

During triaxial testing, principal stresses are not allowed to rotate. The vertical and lateral pressures applied are defined as principal stresses, because it is assumed that no shear stresses are present on the vertical and horizontal planes throughout the test. Although it is assumed that there are no shear stresses present on the vertical and horizontal planes during the test, the end restraints must impose some unintended friction at the specimen interfaces. The friction at the interfaces will limit the lateral deformations at the boundaries. The stresses and strains of the specimen become less uniform as the specimen deviates from the prepared cylindrical shape during shearing. The change in cross-sectional area during the shearing phase is somewhat addressed in analysis steps that calculate the central area during shearing (Bardet, 1997; ASTM D7181-11, 2011). The intermediate principal stress, σ'_2, is also neglected during triaxial testing by setting σ'_2 equal to σ'_3, which is equal to the cell pressure. Plane strain conditions that employ a unique intermediate principal stress are common in engineering problems, the exclusion of which may provide slightly lower friction angles resulting from triaxial testing.

2.3.2 Simple Shear Testing

The simple shear testing apparatus is similar to the direct shear test, except failure is not forced to occur on the horizontal plane; the vertical boundaries are allowed

to tilt and do not stay at 90° with the base. The specifics of the simple shear test are outlined by multiple works (e.g., Airey et al., 1985; Bardet, 1997; Kraupa, 2013). The non-uniform deformation generated during direct shear testing motivated the development of a test to employ uniform stresses and strains. Simple shear specimens are confined laterally and confining pressure is applied uniaxially. The specimen is sheared by displacing one end of the specimen horizontally while the specimen sides deforming in a tilting motion, allowing a more natural failure plane of the soil than in direct shear testing. The simple shear device allows rotation of principal stresses and aims to impose a plane strain shearing mode, unlike triaxial tests.

There are three common simple shear testing apparatuses: the Swedish Geotechnical Institute (SGI) device, the Norwegian Geotechnical Institute (NGI) device, and the Cambridge device. The testing apparatus used in the current investigation herein for simple shear testing most closely matches the SGI-type device, which was designed by Kjellman in 1936. The respective apparatus tests a confined specimen enclosed in a membrane surrounded by a stack of thin rings. Simple shear tests performed herein are strain-controlled, performed with the SGI-type device. The loading and displacement mechanisms of the simple shear testing apparatus are shown in Figure 2.9. The axial (vertical) and shear strains measured throughout shearing in the simple shear device are defined as,

$$\varepsilon = \frac{\Delta h}{h_c}, \qquad \gamma = \frac{l}{h_c}, \tag{2.18}$$

respectively, where Δh and h_c are the height of the specimen after consolidation and change in specimen height (as defined for triaxial testing), and l is the lateral dis-

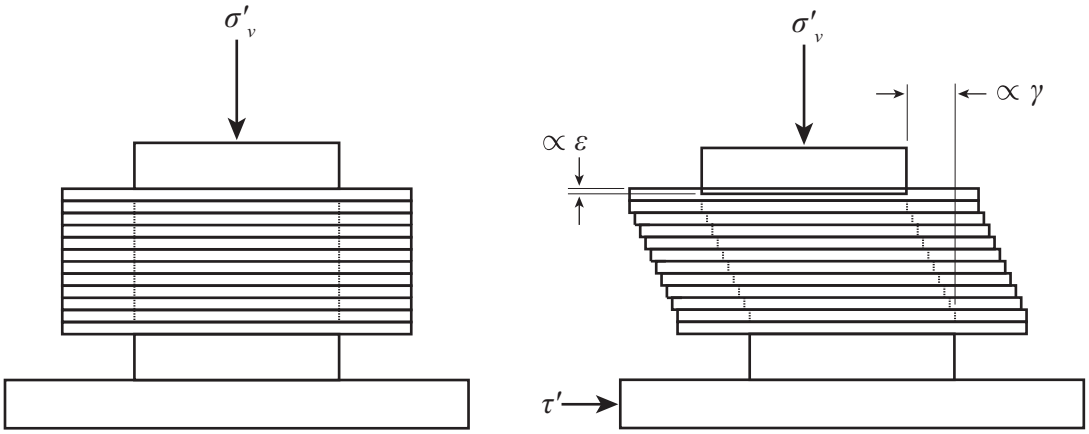

Figure 2.9: SGI-type simple shear test loading schematic. The left figure shows the specimen within the confining rings uniaxially consolidated. The figure on the right shows shearing loads imposed on a specimen. The measurements shown are proportional to the axial and shear strains, ε and γ, respectively.

placement. The volumetric response during simple shear testing is observed through plotting ε versus γ, because the specimen is confined laterally so volume changes can only be observed and measured vertically.

In a fully instrumented simple shear apparatus, such as the Cambridge device, sufficient load cells surrounding the sample can define the full stress path and all information of the central stress tensor. In testing apparatuses like the simple shear device used herein, only the boundary horizontal and vertical stress and strain measurements are available; therefore, the complete stress conditions of the specimen are not known (i.e., magnitudes and orientation of principal stresses). Typically, if stresses were measured in the center of the specimen, the horizontal shear and normal stresses would be larger than the averages measured on the boundaries (Airey et al., 1985). Accordingly, assumptions must be made to interpret the results of simple

shear tests.

Airey et al. (1985) presents that if the horizontal plane is assumed to be the plane of maximum stress obliquity, then the friction angle from simple shear tests is estimated as,

$$\phi' = \arctan \frac{\tau'}{\sigma'_v}, \tag{2.19}$$

but if the failure surface is assumed to be horizontal, then the friction angle is estimated as,

$$\phi' = \arcsin \frac{\tau'}{\sigma'_v}. \tag{2.20}$$

To determine if a specimen has reached critical state, Atkinson et al. (1991) recommends plotting the stress ratio, τ'/σ'_v, versus shear strain, γ, and observing the shearing response to note the point where constant shear stress is reached.

To aid in the verification of analysis methods to determine the appropriate friction angle from simple shear results, Wijewickreme et al. (2013) utilizes a discrete element method (DEM) to simulate a simple shear test, wherein the true modeled mobilized friction angle within the specimen is estimated. The modeled friction angle is then compared with estimations of the friction angle by Equations 2.19 and 2.20. Wijewickreme et al. (2013) determines that at larger shear strains, Equation 2.19 is a better estimation of the mobilized friction angle, because the horizontal plane nearly produces the maximum stress obliquity. At small shear strains (i.e., around $\gamma = 5\%$), the mobilized friction angle was more closely estimated by Equation 2.20, because the maximum shear stress was acting on the horizontal plane.

The results of the Wijewickreme et al. (2013) study show that there is a rotation

of the principal stresses during simple shear testing. Rossato and Simonini (1991) provide a relationship to estimate the principal strains from the measured shear and normal stresses during simple shear testing. The estimated principal strains are defined as,

$$\varepsilon_1 = \frac{1}{2}\left(\varepsilon + \sqrt{\varepsilon^2 + \gamma^2}\right), \qquad \varepsilon_3 = \frac{1}{2}\left(\varepsilon - \sqrt{\varepsilon^2 + \gamma^2}\right). \tag{2.21}$$

The estimation for ε_1 is given directly by Rossato and Simonini (1991), and the complimentary estimation for ε_3 is provided by Kraupa (2013). Houlsby (1991) provides an estimation of the dilation angle for simple shear tests from incremental principal strains, given as,

$$\sin(\phi'_d) = \frac{-(\delta\varepsilon_1 + \delta\varepsilon_3)}{\delta\varepsilon_1 - \delta\varepsilon_3}. \tag{2.22}$$

The principal strain values may be estimated from Equation 2.21, and incremental changes in the principal strains can be defined throughout simple shear testing to estimate the dilation angle at various shear strains during the response with Equation 2.22.

2.3.3 Surface Particle Testing

In addition to the friction angle determined with typical geotechnical testing equipment described in the previous sections, physical measurements of simple particle arrangements can be informative for strength observations, especially when concerned with the near-surface environment. Yang et al. (2009, pg. 685) states that, "the angle of repose is one of the most significant macroscopic parameters in describing

the behavior of granular materials. Under a static condition, the angle of repose is the steepest angle at which the sediment particles can stay without motion." The angle of repose of a collection of soil particles relates to the internal angle of friction. Several researchers have used the angle of repose to estimate the critical state friction angle (Santamarina and Cho, 2001; Sadrekarimi and Olson, 2011). More specifically, Sadrekarimi and Olson (2011) note that the angle of repose is a reasonable approximation for the critical state friction angles of sands under low confining pressures. Sadrekarimi and Olson (2011) found the angle of repose to be approximately 3° to 4° higher than the critical state friction angle at typical geotechnical confining pressures ($\sigma'_v \approx 200$ kPa for the cited study) for subrounded to subangular sands.

There are a number of methods used to estimate the angle of repose for sands. Researchers have investigated various methods in comparative studies (e.g., Train, 1958; Rousé, 2014). Train (1958) shows that for a specific sand, the angle of repose decreases as the height of the observed collection of particles increases, in either a heap formation or tilted table with a finite thickness of sediment. The range in angle of repose for the sand found with different testing methods was about 5° (i.e., 22.5° to 27.5°), with the lower bound corresponding to a mound created by sediment forming a mound that failed continuously until stable, and the upper bound corresponding to tilted table experiments.

In an evaluation of six different methods to determine the angle of repose, Rousé (2014) studies the responses of six sands with various gradations, including three river sands, two beach sands, and one manufactured sand. Rousé (2014) finds that the method for determining the angle of repose via ASTM C1444-00 (2000) is generally

the most consistent. It is noted that the standard provided by ASTM C1444-00 (2000) was withdrawn in 2005, due to limited use by industry. The method developed by Santamarina and Cho (2001) to estimate the critical state friction angle by the angle of repose measured as the inclination of sediment tilted in a graduated cylinder in wet and dry conditions is also evaluated by Rousé (2014). The results of the graduated cylinder test were less precise and showed lower values of the angle of repose than the ASTM C1444-00 (2000) method.

To determine the sediment bed-friction coefficient for use in sediment transport analyses, Shields (1936) recommends the procedure of adhering uniform grains to a flat board and then several particles of interest may be scattered on the fixed rough board. The board should then be gradually raised as an inclined plane and shaken slightly until incipient motion begins. As noted by Shields (1936), particle shape influences the bed-friction coefficient, and similarly the 'pocket-friction' angle (Booth et al., 2014) determined with the described inclined plane method.

Miller and Byrne (1966) determine the pocket-friction angle of various sediments by methods similar to the procedure recommended by Shields (1936). A tilted plate with a bed of adhered particles is utilized and particle motion is observed for individual free particles placed on the plate when inclined. The tilt tests are performed in dry and subaqueous environments. A binocular microscope fixed to the plate and a protractor allow observations of incipient particle motion. For each particle size under investigation in the respective study, the tilt test is performed approximately two hundred times. Sets of tests were performed for various sediment types, and on rough sediment beds of fixed particles of a distribution and uniform sized sediments. There

is no clear trend determined by Miller and Byrne (1966) for the difference between dry and submerged pocket-friction angles. Miller and Byrne (1966) summarize a range of pocket-friction angles from 45 to 70° were observed for free particles ranging from well rounded and nearly spherical tested on a fixed bed of uniform sediment, to low sphericity free particles of high angularity tested on a poorly sorted fixed sediment bed.

Similar to the observation of particle shape influence on the pocket-friction angle stated by Shields (1936), Yang et al. (2009) notes that the pocket-friction angle for a single free particle is likely a function of the geometry of the particle and respective grain pocket produced by the fixed particles on the testing plane. The pocket-friction angle is not likely affected by the interparticle or sliding friction angle, ϕ'_{μ}, because rolling will likely be the mechanism determining the failure angle.

Booth et al. (2014) states that the pocket-friction angle is a parameter that exhibits much larger variability than the Mohr-Coulomb friction angle. The investigation presented in Booth et al. (2014) studies the pocket-friction angle of subrounded gravel (d_{50} = 15 mm). The pocket-friction angle for a single particle was up to 15° larger than for the angle determined for a string of $\approx$ 20 particles. Increasing the length of the 'force-chain' by setting the gravel particulate in-line on the fixed gravel bed plane was performed to simulate the failure angle approaching the Mohr-Coulomb friction angle. The study by Booth et al. (2014) aims to clarify the transition of sediment strength from a single free particle on the surface of a sediment bed to the Mohr-Coulomb strength defined for a continuum of sediment. A logarithmic trend is observed for the increase of friction angle to the pocket-friction angle of a single par-

ticle. The work by Booth et al. (2014) provides an example of the changing strength properties of single particles to a collection of soil particles for a granular material. The gravel investigated allows for easier observations of failure and manipulation of free particle arrangement on the fixed sediment plane to inform the trends of the strength changes noted.

2.4 Near-Surface Stability Challenges

The respective background section will discuss why the granular sediment properties and response detailed in Chapter 2 are influential for near-surface engineering application. As introduced in Chapter 1, coastal sediment beds prone to large overflows, such as tsunamis, are important to characterize near the surface to improve the accuracy of sediment transport model predictions. There are many other applications for which understanding soil response at low confinement is important (Ponce and Bell, 1971; Stroud, 1971; Fukushima and Tatsuoka, 1984; Chakraborty and Salgado, 2010; Sadrekarimi and Olson, 2011). The accuracy of all low confinement geotechnical engineering applications that utilize the friction angle to define the shear strength of granular sediment would be improved by considering the true friction angle in the in situ environment, including shallow bearing capacity problems, shallow sand slope failure analysis, interpreting in situ tests performed at shallow depths, and simulating 1-g model tests (i.e., those not modeled in a centrifuge to alter gravitational forces). Another low-stress environment of interest may be the moon, as lunar construction becomes a more realistic venture (Chakraborty and Salgado, 2010). Perhaps many

other aspects of the typical approach of geotechnical engineering would have to be greatly altered to account for the negligible atmospheric pressure and reduced gravity that would act on lunar sediment, thus expanding the 'near-surface' zone. Herein, focus is given to the coastal and sediment transportation influences of the work, because the sediments obtained from the South Beach site are in an environment prone to tsunami hazard.

In sediment transport models, there are shortcomings in accounting for influential sediment properties. Index properties such as d_{50} and G_s may be considered to represent the sediment, as in the (Shields, 1936) approach, without implementing more information about the gradation, shape, and packing state of the sediment bed. As introduced, the onset of incipient sediment motion (the initiation of particle movement) caused by fluid flow can be predicted with the Shields (1936) approach. The Shields parameter, Θ, is defined as the ratio of the bed-shear stress to the buoyant unit weight of a sediment. To estimate incipient sediment motion, the calculated Shields parameter as well as the calculated boundary Reynolds number, $Re_\star$, defined by,

$$\Theta = \frac{\tau_0}{dg(\rho_s - \rho)}, \qquad Re_\star = \frac{\rho u_\star d}{\mu}, \tag{2.23}$$

are compared to a threshold curve, shown in Figure 2.10. The initiation of motion is expected of sediments with a calculated Shields parameter plotted above the threshold curve of the critical Shields parameter, Θ_c [more detailed empirical data and annotations are provided in Figure 6 of Shields (1936)]. Within Equation (2.23), τ_0 is the bed-shear stress induced by the fluid flow, d is the particle diameter of sediment

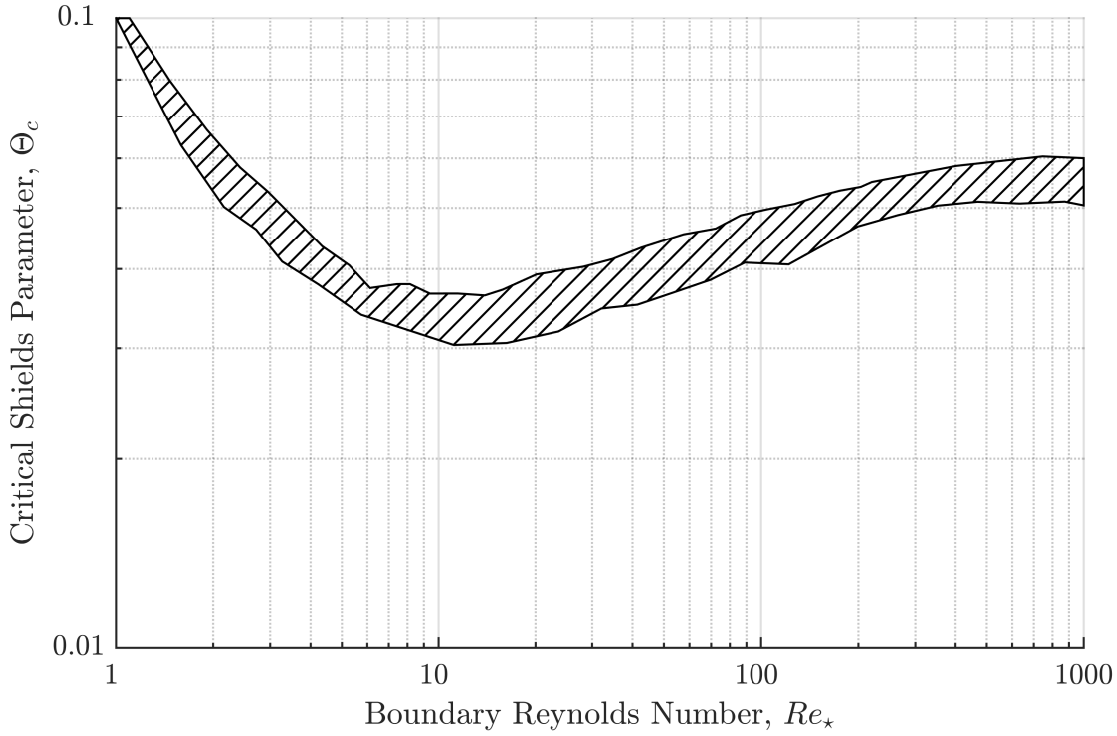

Figure 2.10: The Shields (1936) threshold curve. The double logarithmic scale plot shows the critical Shields parameter, Θ_c, against the boundary Reynolds number, $Re_\star$. Above the defined threshold curve, shown as the hatched region, incipient motion of particles is expected. The threshold curve is generated for a sediment bed of uniform grain size and angular shape for particles of various densities (modified after Shields, 1936).

(often assumed to be the mean grain-size diameter, d_{50}), g is the acceleration due to gravity, ρ_s is the mass density of the sediment grain, ρ is the mass density of water, $u_\star$ is the shear velocity $[u_\star = (\tau_0/\rho)^{0.5}]$, and μ is the dynamic viscosity of water. The development of the Shields threshold curve is based on bed-load movement in steady river flow applied to a rectangular river channel. The estimated bed-shear stress is determined by the principle of momentum. Empirical data is gathered by experiments performed in model flumes which demonstrate the interaction of the applied flow to the bed of uniform grain sizes and generalized grain properties.

Soulsby (1997) expanded upon the work of Shields (1936) for steady currents, so that the Shields parameter would be applicable to environments with waves and combined waves and currents. Soulsby (1997) presents the Shields threshold curve in a more convenient form, plotted as Θ_c against the dimensionless grain size of sediment particles, to avoid the shear velocity term being present in both axes values, as it influences the critical bed-shear stress and the boundary Reynolds number of particles.

Another form of sediment instability induced by overlying flow is plug formation. Plug formation is defined as the phenomena where the sediment of interest begins to move as a solid block upon flow reversal, as observed in experiments by Flores and Sleath (1998). Re-evaluation of the results presented in Dick and Sleath (1992) which executed experiments in severe conditions suggests that plug formation may have also occurred, but was not recognized at the time. Following the investigation of the conditions under which plug flow occurs, Sleath (1999) states that for oscillatory flow (i.e., waves), plug formation is governed by the Sleath parameter, Sl, and the

degree of compaction (i.e., packing density) of the sediment. The Sleath parameter is defined by the forces exerted on a sediment grain from the oscillatory pressure gradient and by gravity, given as,

$$Sl = \frac{\rho U_0 \omega}{(\rho_s - \rho)g}, \tag{2.24}$$

where U_0 is the amplitude of the oscillatory velocity outside the boundary layer, and ω is the angular frequency. Understanding the mechanism of plug formation is important because, as stated by Sleath (1999, pg. 1644), "it could have significant implications for those attempting to model the transport of sediment or calculate quantities such as the maximum depth of erosion," which is a major motivation of coastal engineers. The Sleath parameter accounts for the horizontal gradient induced by the oscillatory flow and utilizes the density of individual particulate. The Sleath parameter combined with the packing density state of the sediment bed is used to estimate sediment instability through plug formation.

Researchers have considered the effects of exacerbated sediment transport through 'enhanced scour' by considering pore-water pressure changes within the sediment bed during large overflow depth buildup and removal (e.g., Tonkin et al., 2003; Yeh and Mason, 2014); when considering a tsunami wave, the pressure buildup and removal imposed on the sediment bed due to the large wave height occurs during runup and draw-down stages, respectively.

When the excess pore-water pressures (those greater than the pore-water pressure during hydrostatic conditions of a saturated deposit) within the sediment bed become

sufficiently high, effective stresses within the bed become negligible, causing liquefaction. Liquefied soil exhibits a complete loss of shear strength. Tsunami inundation during the runup phase increases pore-water pressures within a saturated sediment bed. The pore-water pressures increase with the added total stress from the overlying wave height. The rapid reduction of water wave height during tsunami draw-down results in the removal of total stress and the built-up excess pore-water pressures within the sediment bed begin to dissipate. The dissipation of excess pore-water pressure create a pressure gradient producing upward seepage flow. The high excess pore-water pressures and upward flow within the sediment bed, which can cause a complete loss of effective stress, is called momentary liquefaction (Sumer and Fredsøe, 2002). Yeh and Mason (2014, pg. 132) suggest that, "momentary liquefaction is the most likely cause of excessive tsunami-induced soil instability." Momentary liquefaction also produces the 'enhanced scour' phenomena noted by Tonkin et al. (2003).

As noted, at the liquefied state soil possesses negligible shear strength. Substantial scouring can occur at or near this liquefied state. Tonkin et al. (2003) found when investigating enhanced scour surrounding coastal structures, that the instance of greatest scour depth occurs during draw-down, and does not coincide with the greatest flow velocity. In fact, in the noted study, the maximum scour was observed near termination of draw-down, when the flow was very shallow. With a shallow flow producing low overburden pressures on the sediment bed, this phase was suspected to have a sizable upward flow expelling from the bed in order to equilibrate with the decreased surface pressures. This observation justifies the importance of studying the effect of the vertical gradient within the soil bed. Yeh and Mason (2014) develops a

modified Shields parameter that considers the vertical gradient within the sediment bed induced by tsunami draw-down. The modified Shields parameter also considers the bulk density (i.e., packing density) of the respective sediment deposit, in addition to the mean grain-size diameter.

The noted sediment instability models, among others, employ characteristics of the fluid flow imposing shear stresses on the sediment bed in addition to basic soil properties (e.g., mean grain-size diameter, specific gravity, packing density). Although comparisons to empirical data from observed sediment transport occurrences is informed indirectly by sediment shear strength (in the form of observed resistance to displacement), making appropriate comparisons to the response of generalized sediments is an area of large uncertainty. There are many other contributors to the near-surface shear strength and response of sediment, as detailed herein, that are not considered when predicting the response of generalized sediment deposit.

Stark et al. (2014, pg. 469) reaffirms that, "the friction angle is known to be a major factor controlling the critical shear stress required to initiate particle motion." The authors also state that the friction angle is a function of grain size, sorting (i.e., gradation), packing density, particle arrangement, and particle shape (Stark et al., 2014). Characterictic friction angles, including the angle of repose and pocket-friction angle, also influence sediment instability. Yang et al. (2009, pg. 685) states that the angle of repose "is important in sediment movement like the bed-load transport, suspended-load transport, the scour of the channel and the incipient motion of sediment." As discussed by Booth et al. (2014), for some sediment transport problems, several particles may be interacting, not as single particles or a continuum of parti-

cles; therefore, the pocket-friction angle or the Mohr-Coulomb friction angle are not appropriate to estimate the sediment response. Clearly, there is a need to investigate and define intermediate friction angles for sediment in the near-surface zone.

The particle Reynolds number influences the drag of particles, as noted by Loth (2008), which would affect how particles move and transport once suspended in an overlying flow. Particle size and shape also affect the drag response Loth (2008) defines the the Corey shape function (factor), CSF, and the max-med-min area, $A^{\star}_{mmm}$, to characterize particle shape as a function of the minimum, intermediate, and maximum axis lengths of a particle. The noted parameters inform appropriate drag forces used in respective analyses. Additionally, particle size and gradation, shape, and packing density, affect the hydraulic conductivity, k. Hydraulic conductivity and soil stiffness determine the coefficeint of consolidation, c_v, which defines how water travels through a sediment deposit, and consequently, how pore-water pressures dissipate. As discussed, excess pore-water pressure dissipation can affect the stability of a sediment bed by altering the effective stresses, possibly leading to enhanced scour (Tonkin et al., 2003; Yeh and Mason, 2014). To simplify the estimation of pore-water pressure dissipation and determine the resulting pressure gradient, full saturation of a sediment bed is sometimes assumed to utilize estimations of the coefficient of consolidation to solve Terzaghi's 1D consolidation equation, as shown by Yeh and Mason (2014). The coefficient of consolidation can be defined as,

$$c_v = \frac{k}{\gamma_w m_v}, \tag{2.25}$$

where m_v is the coefficient of volume change, which is a function of the constrained modulus, D (note that $m_v = 1/D$), as shown in the relations provided by Lambe and Whitman (1969) and Holtz et al. (2011).

In conclusion of this literature synthesis, to accurately predict sediment response in the near-surface region, it is important to consider soil index properties and the appropriate strength parameters, because for a given sediment there are a multitude of characteristic friction angles. Increased adoption of the discussed soil properties of near-surface deposits in sediment instability and transport models will improve the accuracy of the analyses estimating incipient motion of particulate, plug flow, and enhanced scour.

Chapter 3: Laboratory Methods and Results

3.1 Sampling Program: South Beach, Newport, Oregon

A laboratory program was performed to characterize the beach sediment from South Beach, Newport, Oregon and investigate the mechanical behavior of the material. The sampling cross section of the beach was selected at a location just north of the beach outlet trail from the South Beach State Park parking lot. The selected location is south of the city of Newport and the Yaquina Bay jetty. Samples from the beach cross section were obtained on three dates spaced approximately six months apart in order to make observations about the morphology of the beach. Sampling efforts were performed on 1 March 2016, 10 September 2016, and 5 March 2017, and herein, are referred to as M1, S10, and M5, respectively.

Tide prediction tables published by the National Oceanic and Atmospheric Administration (NOAA) for South Beach, Newport, Oregon (Station ID: 9435380) were consulted. Sampling was performed at times corresponding to the daily low water level for each sampling effort. The selected sampling locations along the beach cross section correspond with tidal datums defined by NOAA (2013). Samples were obtained near the targeted tidal marks of Mean Lower-Low Water (MLLW), Diurnal Tide Level (DTL), the Mean Higher-High Water (MHHW), as well as at the termination of the beach designated as the base the sand dune region (referred to herein

as 'DUNE'). The desired sampling points were located by visual inspection of the beach. During the time of low water level, MLLW samples were obtained at the low point of wave recession. DTL samples were obtained at the edge of the wetting zone, located near the midpoint of the beach cross section. The DTL is defined by NOAA (2013) as the arithmetic mean of the MHHW and MLLW tidal datums. The MHHW samples were obtained at the point where the smooth sediment bed features of the swash zone ceased and debris deposits were observed, signifying the point that high tide waves reached. The DUNE samples were obtained at the base of the sand dune at the termination of beach cross section. Disturbed samples from the surface of the sediment bed at the locations described were obtained with a scoop to a depth of approximately 10 cm. Figures 3.1 and 3.2 show aerial views detailing the approximate points of the sampling locations. Figure 3.3 shows a photograph of the respective beach cross section taken during the M5 sampling effort.

The estimated sample location points shown in Figure 3.2 were determined by making observations of the beach cross section via Google Earth. Satellite imagery is available for the coastline at South Beach, Newport, Oregon on nine dates between 1994 and 2016 (5/5/1994, 8/7/2000, 4/18/2005, 6/28/2005, 8/1/2011, 6/26/2012, 6/19/2014, 7/17/2015, and 8/18/2016). The extent of the swash zone does not appear to substantially change, more than the expected daily variability of the tide levels, over the noted time frame. From the satellite imagery, MHHW and MLLW marks can be estimated by the observed high and low water levels, respectively, because the nine images appear to be captured during a wide variety of tide levels.

Once the sampling location estimates were established, coordinates of the swash

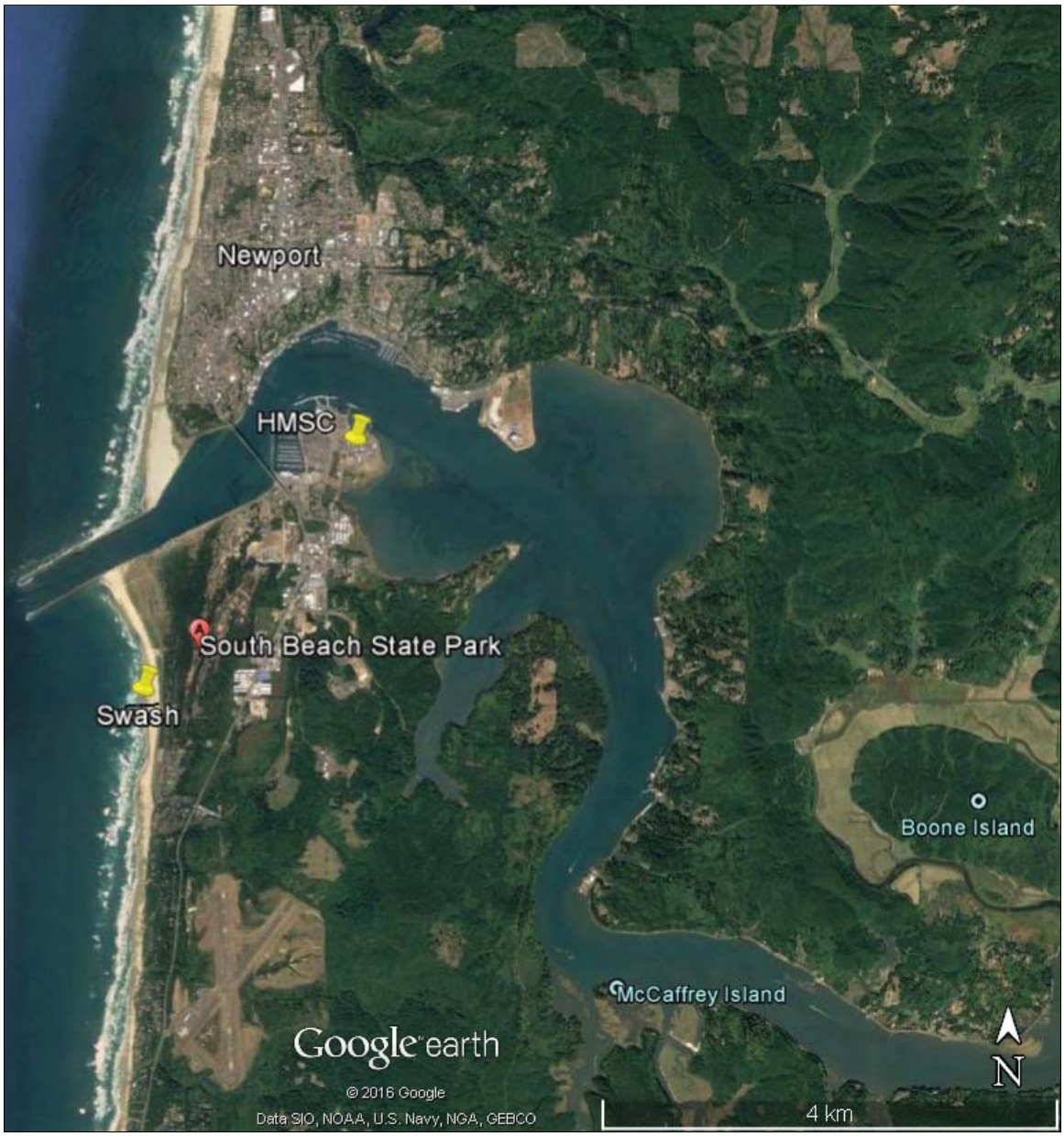

Figure 3.1: South Beach, Newport, Oregon vicinity map. The sampling swash zone cross section of the beach is shown located near South Beach State Park and south of Hatfield Marine Science Center (HMSC) and the city of Newport, Oregon. The WGS84 coordinates of the DTL sampling location along the beach cross section are approximately 44°36.100′ N, 124°4.160′ W (imagery date: 8/18/2016).

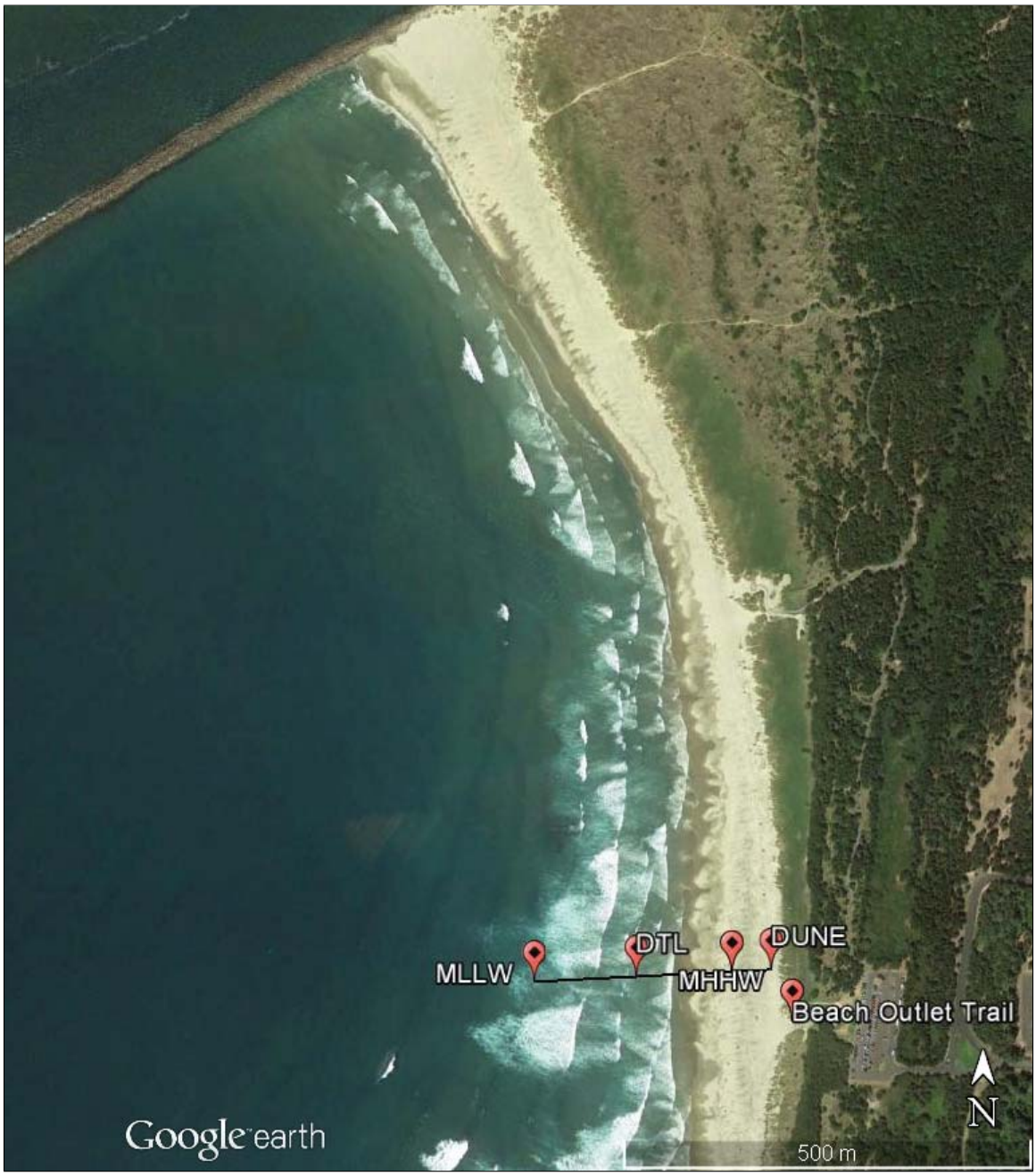

Figure 3.2: Schematic of sampling locations. Approximate cross section location shown for South Beach, Newport, Oregon (imagery date: 8/18/2016).

Figure 3.3: South Beach, Newport, Oregon cross section photograph. Image captured on 6 March 2017.

zone were estimated to the nearest meter in Google Earth to determine the average slope of the beach cross section. The estimated average beach slope is 1:80 (V:H) and the total length of the cross section sampled is approximately 300 m. The estimated slope is consistent with the historic beach profiles shown previously in Figure 2.1.

The estimations of beach topography are simplified considerably in the current study. A geologic survey with the use of total stations and lidar would increase the accuracy of important tidal elevations, coordinates, and the resulting beach slope. The visual identification of the desired sampling locations could be improved by observing the beach cross section for longer periods of time to better understand the trends of the daily tides and more confidently identify the tidal marks of interest. The WGS84 coordinates for the DTL sampling location of the beach cross section

are approximately 44°36.100′ N, 124°4.160′ W, estimated visually from Google Earth. The respective coordinates are provided in order to approximately identify the vicinity of beach cross section location. Specific coordinates of the sampling locations were not measured at the time of sampling and the locations were approximated from the beach features and tidal level estimates, as discussed. The purpose of the sampling program was to obtain beach sediment samples that were representative of the extent of the respective beach cross section at approximately the same locations on different sampling dates over the course of the current study to observe spatial and temporal variability. Exact coordinates and elevation data was not critical for the goals of this thesis.

The samples of beach sediment obtained from South Beach, Newport, Oregon were rinsed with distilled water over a No. 400 sieve (0.037 mm sieve openings) to cleanse the samples of the salt water. Rinsing the salt water from the samples was necessary to properly oven dry and prepare the testing specimens without corroding testing equipment. To verify that fines [i.e., particles passing the No. 200 sieve (0.075 mm sieve openings)] were not lost during rinsing, the rinse water was collected in a receptacle and inspected to ensure that notable amounts of sediment were not collected. In several instances, the rinse water was oven dried and only a thin film remained on the receptacle. It was concluded that only trace amounts of fines were lost during the rinsing process ($< 1\%$ of total sample mass). The rinsed and oven dried (drying oven maintained at $105 \pm 5°C$) sediment samples were subjected to sieve analyses, particle shape analyses, specific gravity testing, minimum and maximum packing density testing, consolidated-drained (CD) triaxial compression testing, constant vertical stress

simple shear compression testing, angle of repose testing, and inclined plane testing. The selected tests were included in the laboratory program to determine important characteristics of the beach sediment, as discussed in Chapter 1. The methods and results of the laboratory tests are detailed in the following sections.

3.2 Index Properties

3.2.1 Particle Size

A stack of standard 8 inch (20 cm) diameter US sieves was used to mechanically separate the particles constituting the sediment samples. Guidance from ASTM D6913-04 (2009), ASTM D422-63 (2007), and ASTM C136/C136M-14 (2014) was followed during sieve analyses. ASTM D6913-04 (2009) provides the most stringent guidelines to limit sieve overloading, and small specimen masses (75 g based on a maximum particle size of 0.425 mm) were recommended for sieve analyses of the sediment of interest. In cases where larger samples were tested, the specimens were hand sieved (tilted and jarred back and forth), following the minimum time of the stack being locked in the mechanical shaker, for an additional minute. Table 3.1 details the sizes of the sieve openings for the specific sieves utilized during the particle size analyses herein. Oven-dried samples were poured over the prepared sieve stack, which was then covered with the cap and locked into a mechanical shaker, as shown in Figure 3.4. The mechanical shaker was set for a minimum of ten minutes of shaking.

The majority of sediment mass was retained on the No. 70 (0.212 mm sieve open-

Table 3.1: Sieve sizes used in analysis.

US sieve number	10	25	40	70	100	140	170	200
Sieve openings (mm)	2.00	0.710	0.425	0.212	0.150	0.106	0.090	0.075

Figure 3.4: Sieve stack locked in a mechanical shaker.

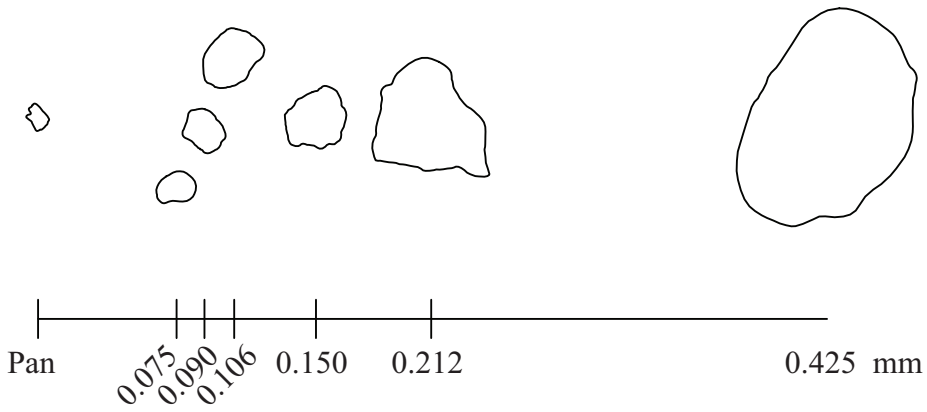

Figure 3.5: Visual representation of particle size range (recommended by Mitchell and Soga, 2005).

ings) and No. 100 (0.150 mm sieve openings) sieves. Sediment passing the No. 140 (0.106 mm sieve openings) sieve appeared dark gray and metallic in contrast to the tan particulate retained on larger sieves. An appreciation for the variety of sizes in the distribution of particles can be gained from a visual representation, as suggested by Mitchell and Soga (2005). Figure 3.5 shows scale particle outlines retained on respective sieve size openings. No particles were retained on the No. 10 sieve (2.00 mm sieve openings). For some specimens, several particles were retained on the No. 25 sieve (0.710 mm sieve openings), but the respective particle size drawing is not included in the visual representation in Figure 3.5 because the presence was minimal.

To investigate the repeatability of the sieve analyses, three tests were performed on specimens from each beach location from the M1 sampling effort. Figure 3.6 shows that the grain-size distribution curves for each beach location were well replicated by successive tests. The redundant sieve analyses showed that the testing methods were repeatable and that the prepared samples, from which testing specimens were

obtained, were sufficiently homogeneous. Accordingly, only one sieve analysis was performed on specimens from each beach location sample obtained during the S10 and M5 sampling efforts. Figures 3.7 to 3.9 show the grain-size distribution curves produced from the sieve analyses performed on M1, S10, and M5 samples, respectively (the median data set of the three sieve analyses performed on specimens from each beach location on M1 samples was selected for presentation in Figure 3.7). The data points in each semi-logarithmic plot represent the experimental measurements obtained directly from each sieve analysis, and the continuous lines were created by fitting the unimodal equation given by Fredlund et al. (2000), which was shown in Equation 2.2, to each data set. In MATLAB, the `lsqcurvefit` function was used to solve the non-linear least square problem to determine the unimodal fitting parameters: a_{gr}, n_{gr}, m_{gr}, d_{rgr}, and d_m. Figures 3.7 to 3.9 show that the unimodal equations fit the sieve analyses data well, as expected.

The grain-size distribution curves for each sediment sample were used to determine the characteristic particle diameters: d_{10}, d_{30}, d_{50}, and d_{60}. The characteristic particle diameters were used to calculate the coefficient of uniformity, C_u, and the coefficient of curvature, C_c, which were defined in Equation 2.1. Figure 3.10 shows the grain-size distribution curves for each sampling effort grouped by location of the beach cross section. Table 3.2 summarizes the particle size parameters determined from each grain-size distribution curve.

The arithmetic means of the particle size parameters shown in Table 3.2 were also calculated. The arithmetic mean of the mean grain-size for all samples of beach sediment is $\bar{d_{50}} = 0.21$ mm. The arithmetic means of the coefficient of uniformity and

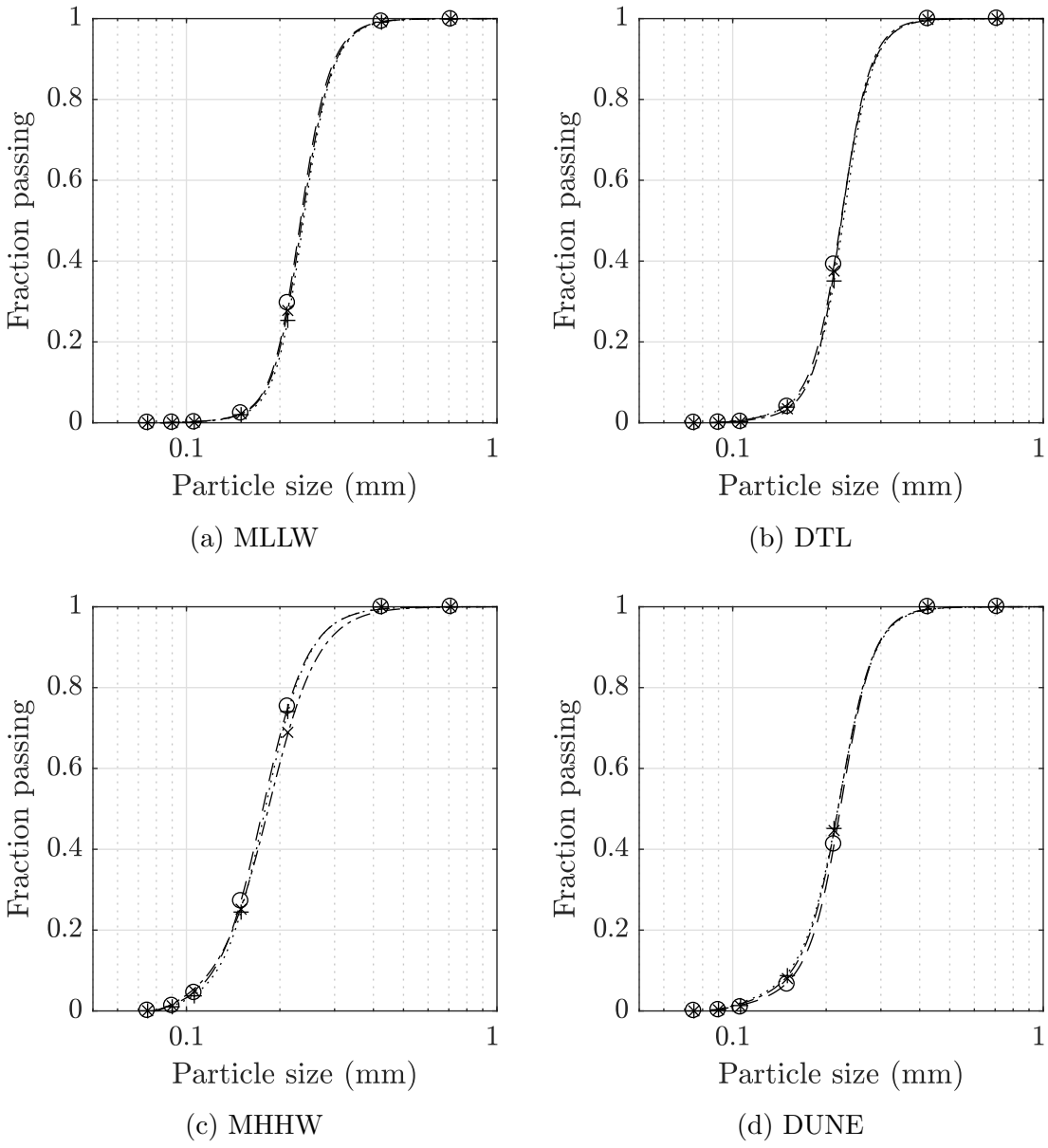

(a) MLLW (b) DTL

(c) MHHW (d) DUNE

Figure 3.6: M1 repeatability check grain-size distribution curves. Each subfigure portrays data points and the corresponding unimodal equation fit for three sieve analyses performed on samples from the specific beach location noted. The three grain-size distribution curves show the repeatability of the sieve analyses performed herein.

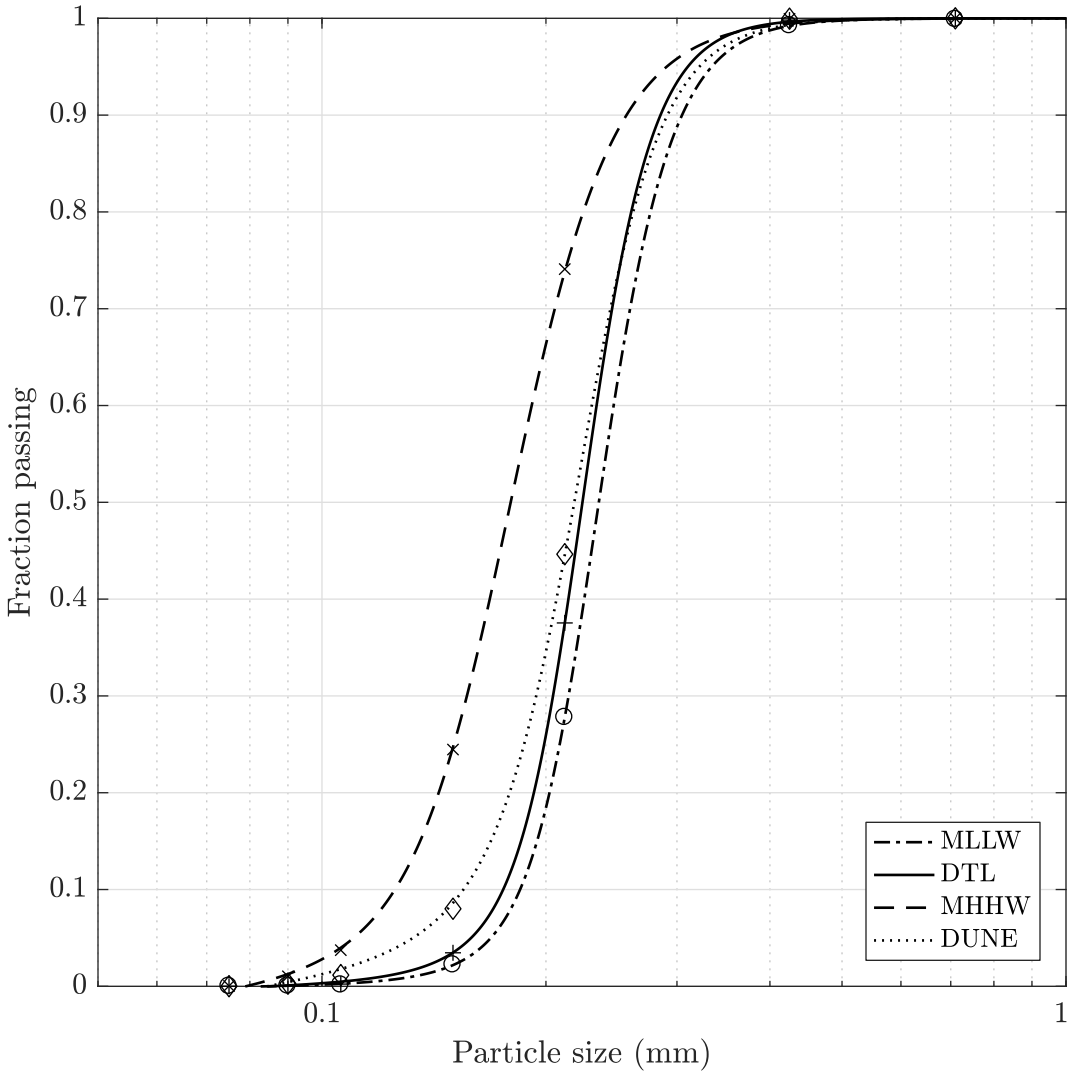

Figure 3.7: M1 grain-size distribution curves.

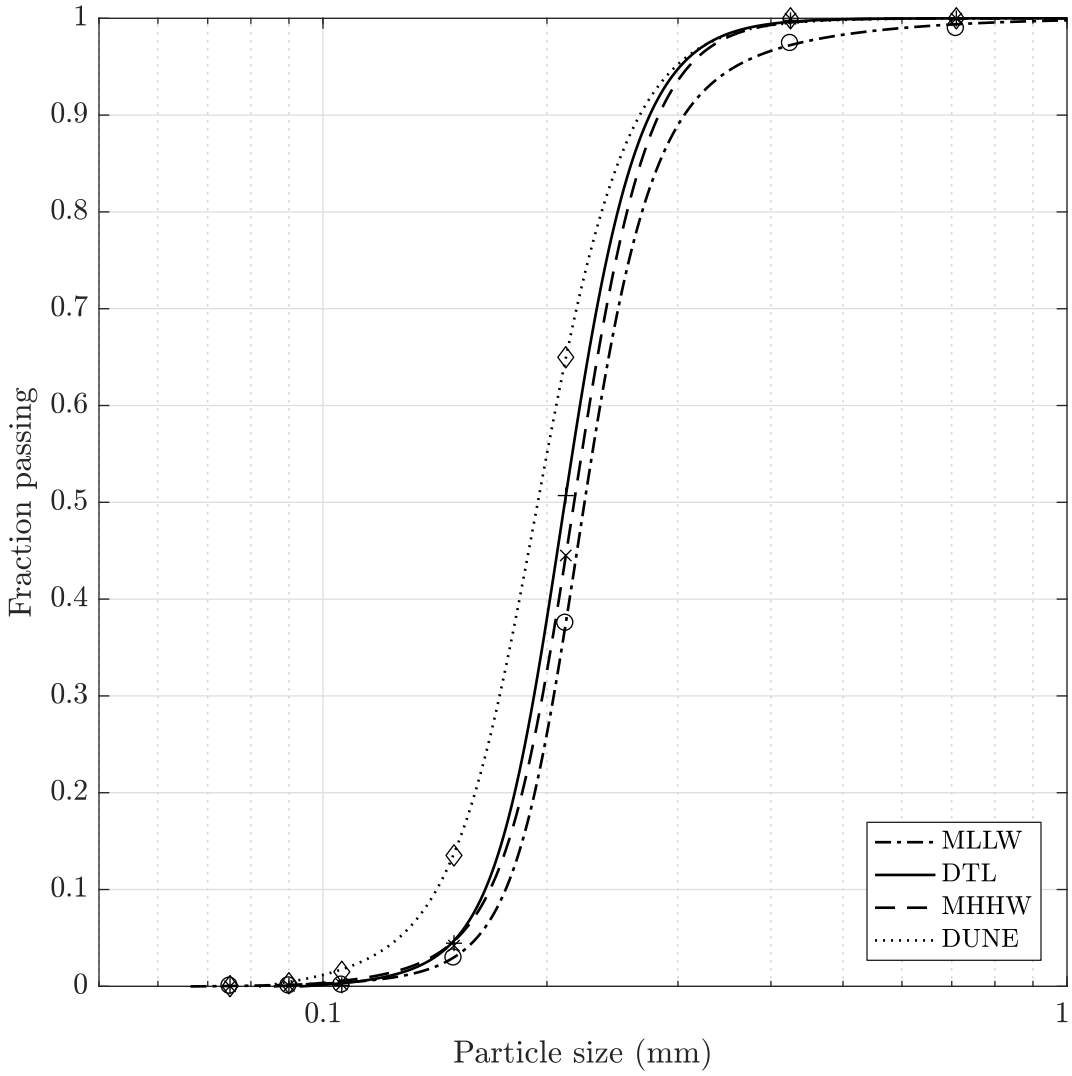

Figure 3.8: S10 grain-size distribution curves.

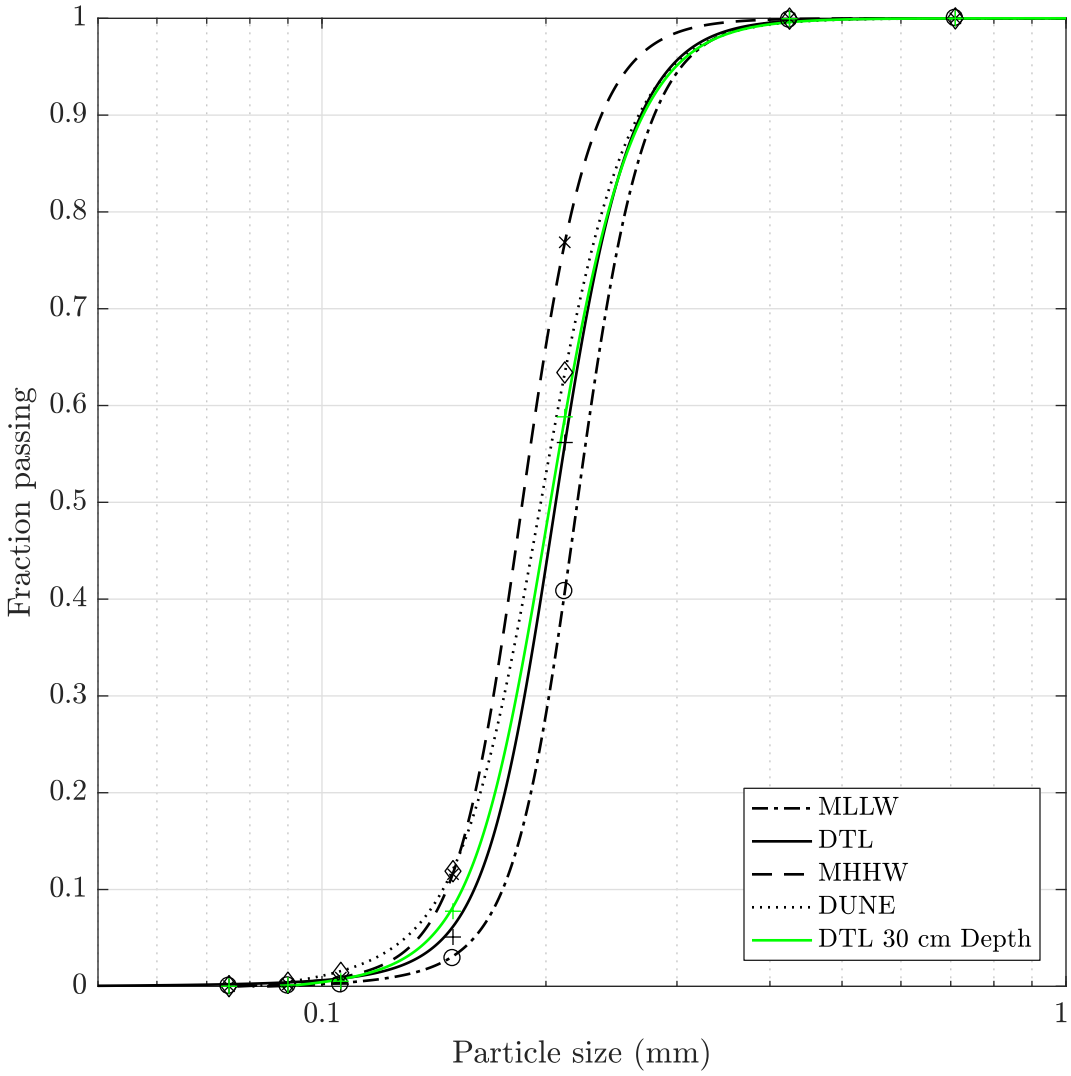

Figure 3.9: M5 grain-size distribution curves.

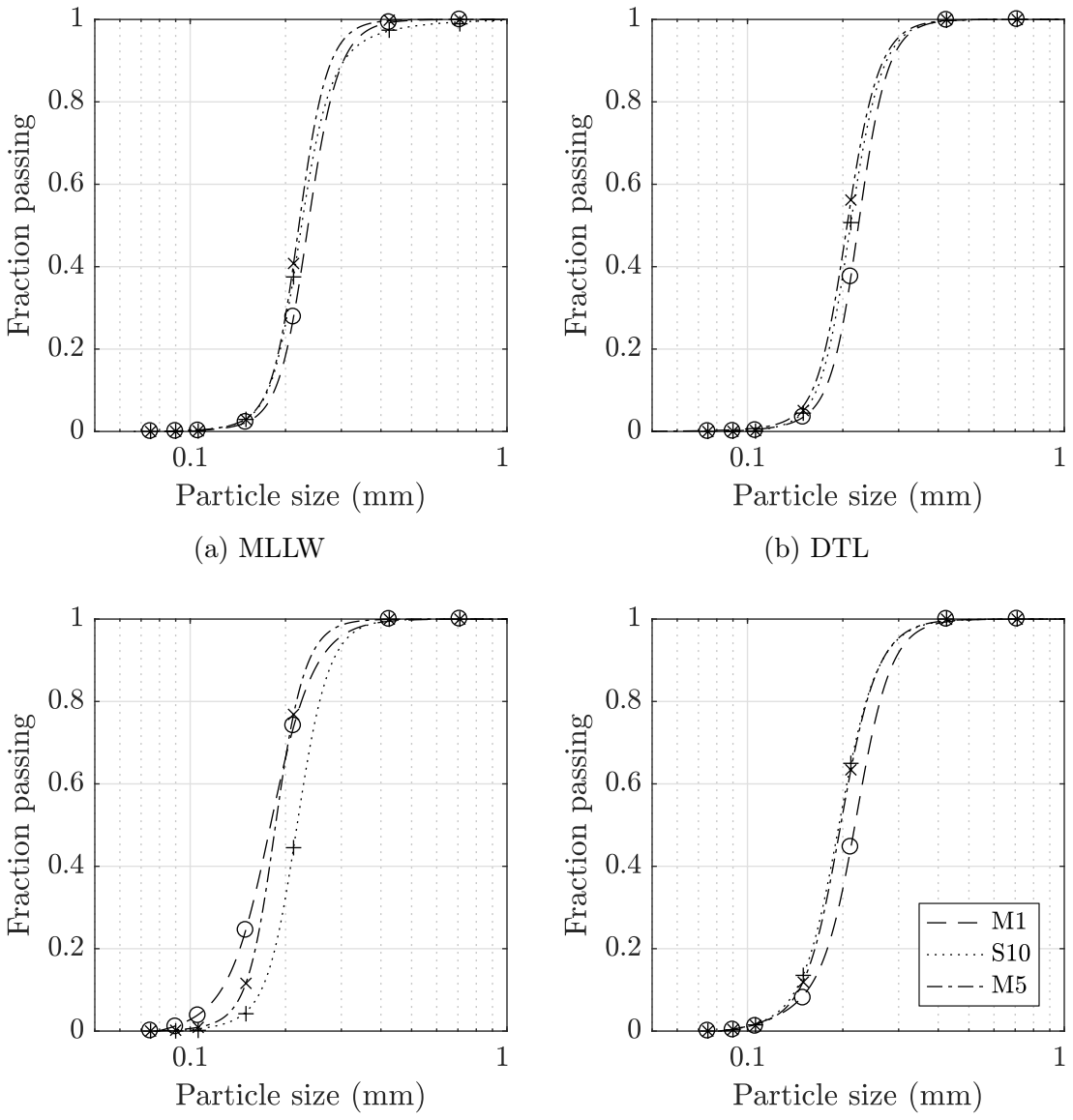

(a) MLLW (b) DTL

(c) MHHW (d) DUNE

Figure 3.10: Grain-size distribution curves for each beach cross section location. Each subfigure portrays data and the corresponding unimodal equation fit for sieve analyses performed on samples from the specified beach location.

Table 3.2: Summary of particle size characteristics. d_{10}, d_{30}, d_{50}, and d_{60} are in units of millimeters, and C_u and C_c are dimensionless ratios.

	MLLW			DTL			MHHW			DUNE		
	M1	S10	M5	M1	S10	M5	M1	S10	M5	M1	S10	M5
d_{10}	0.19	0.18	0.18	0.18	0.17	0.16	0.13	0.17	0.15	0.16	0.14	0.15
d_{30}	0.22	0.20	0.20	0.20	0.19	0.19	0.16	0.20	0.17	0.19	0.17	0.18
d_{50}	0.24	0.23	0.22	0.22	0.21	0.21	0.18	0.22	0.19	0.22	0.19	0.20
d_{60}	0.25	0.24	0.23	0.23	0.22	0.22	0.19	0.23	0.19	0.23	0.21	0.21
C_u	1.34	1.34	1.31	1.34	1.35	1.35	1.53	1.36	1.32	1.48	1.45	1.43
C_c	1.01	1.00	1.01	1.02	1.01	1.01	1.03	1.01	1.01	1.06	1.02	1.03

the coefficient of curvature are $\bar{C}_u = 1.38$ and $\bar{C}_c = 1.02$, respectively. The deviation from these average values is small (i.e., range of values is 0.06 mm for d_{50}, 0.15 for C_u, and 0.04 for C_c). The particle size index properties indicate that the South Beach sediment is a clean, poorly graded, fine sand, classified as 'SP' (ASTM D2487-11, 2011).

Figures 3.7 to 3.9 show that MLLW samples consistently have a distribution of slightly larger particle sizes than samples taken from other locations of the beach cross section. In addition, Figure 3.10 shows that the MHHW samples exhibit greater variability between sampling efforts than the other beach locations (range of d_{50} equal to 0.04 mm for MHHW samples, in comparison with 0.02 mm for MLLW samples, 0.01 mm for DTL samples, and 0.03 mm for DUNE samples). During the M5 sampling effort, a sample was obtained from approximately 30 cm below the ground surface at the DTL location to check particle size consistency with depth. Figure 3.8 shows that the grain-size distribution curve for the DTL surface sample closely represents that of the DTL sample at approximately 30 cm depth. This investigation of the sediment

at a certain depth supports the current assumption that the surface samples are a good representation of the sediments in the near surface region of interest.

Although there are limitations to the accuracy of sieve analyses, the relationships between the gradations of beach sampling locations are likely still representative of the slight spatial and seasonal trends for South Beach, Newport, Oregon. Standard ASTM procedures were followed for the data collected, followed by hand sieving when sieve overloading was observed. As shown in Figure 3.6, when the same procedures are followed for sieve analysis, the resulting grain-size distribution plots are very similar. A discussion focused on the accuracy of sieve analyses is presented in §4.1.1.

The completion of the sieve analyses on all sediment samples obtained from South Beach informs the conclusion that although slight variations are present seasonally and at different beach locations, particle sizes and gradations do not vary appreciably at the investigated beach cross section. The following particle shape investigation further details the characteristics of the beach sediments at various locations of the beach.

3.2.2 Particle Shape

Due to the small dimensions of the fine sand investigated, microscopic imagery was necessary to observe particle shape parameters. A Leica DMRM microscope with QImaging® MicroPublisher 3.3 RTV digital image capture was utilized to obtain two-dimensional sediment particle images using 6.3x magnification (product of the 10x objective lens and 0.63x C-mount). Thirty-five particle images were captured for each

beach cross section location sampled during the S10 sampling effort. The September samples were selected as a representative sediment, because the gradation of samples obtained on the three sampling dates did not appear to differ appreciably, as discussed in §3.2.1. Particle shape analyses were performed to observe the differences in particle shape at different locations of the beach cross section for the S10 samples, although the gradations at the different beach cross sections were observed to vary minimally as well.

The images were scaled with a dimensional stamp that was applied to each captured image. The accuracy of the dimensional stamp was verified by capturing an image of a 1mm x 1mm grid and comparing the measurements of the two image features. With the accuracy of the dimensional stamp verified, the 1mm x 1mm grid paper was not necessary to process the particle images. Accordingly, glass slides were used for particle imaging, because glass slides provided clearer particle images than grid paper when used as a background.

When imaging was performed, the sand sample of interest was homogenized by mixing. Then, a small scoop was taken from the sample and placed on a glass slide. Upon initial placement of the sand particles onto the glass slide, many particles overlapped, which made imaging a complete outline of each particle difficult. To disperse the particles, the slide was released from a very low drop height, which aided in spreading out the particles. In efforts to image a representative portion of the particles within each sand sample, the microscope was focused to an initial location along the upper edge of the slide, then images were taken of particles along a straight path until the bottom edge of the slide was reached. At this point, the microscope was

adjusted laterally and images were taken along a straight path until the microscope had again reached the upper edge of the slide. The noted methodology ensured that no particles images would be duplicated and that every particle type (size and shape) would be imaged in proportion to the sampled scoop, limiting the user bias of particle selection.

Herein, methods were employed to characterize particle shape that produced comparable results for sphericity and roundness, as detailed in §2.2.2, with values ranging between zero and one. Visual inspection of the thirty-five images captured for each location of the beach cross section was performed; more specifically, the particles were compared to the Krumbein and Sloss (1963) roundness-sphericity chart, as recommended by Santamarina and Cho (2004) and Cho et al. (2006). Values of roundness and sphericity were estimated from the Krumbein and Sloss (1963) chart to the nearest 0.1 value, which allowed midpoints between the designations in the chart to be used if the particle appeared to be in between two designations. Figure 3.11 shows an example of a particle being compared with the roundness-sphericity chart. Table 3.3 shows the arithmetic means of the visually-determined roundness and sphericity values for the collection of particles from each beach cross section location. Table 3.3 shows that the arithmetic mean values of roundness and sphericity do not vary more than 0.1 between different beach cross section locations, which is likely within the uncertainty of the process of visually classifying particles (Santamarina and Cho, 2004). The range of roundness values determined (r=0.36 to 0.46) indicates that the South Beach sand is subrounded (Powers, 1953).

Following the visual inspection of each particle, the digital image was copied

Table 3.3: Visual roundness and sphericity estimations for beach cross section locations (S10 sampling effort). The estimations shown are the arithmetic mean of thirty-five particles investigated from each location and classified with the Krumbein and Sloss (1963) roundness-sphericity plot.

	MLLW	DTL	MHHW	DUNE
s	0.73	0.77	0.76	0.73
r	0.41	0.36	0.42	0.46

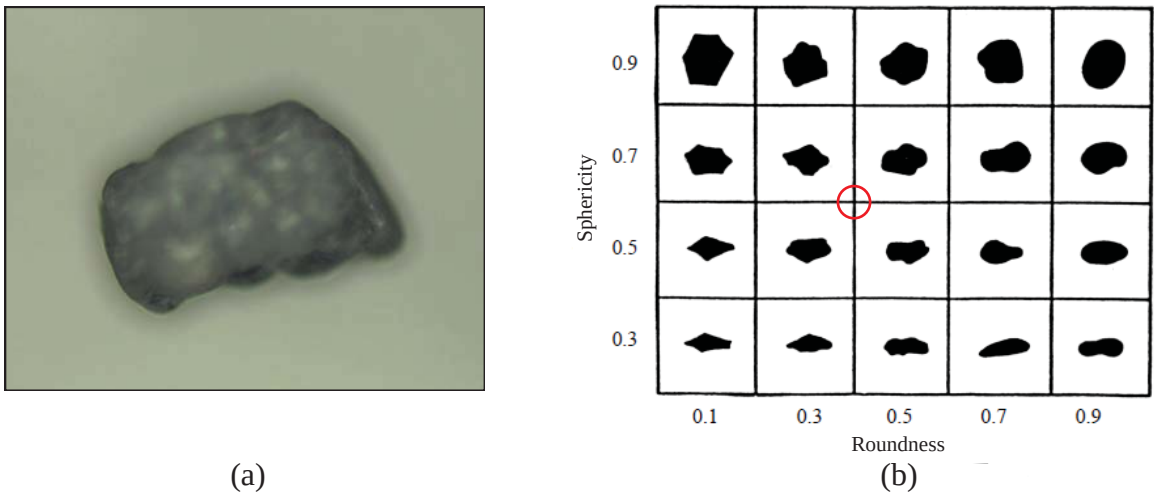

(a) (b)

Figure 3.11: Visual particle shape classification process. Example of a particle image (a), and classifying the particle shape by comparing with the Krumbein and Sloss (1963) roundness-sphericity chart (b). The example particle is classified as $s = 0.6$ and $r = 0.4$ (chart b. modified from Santamarina and Cho, 2004).

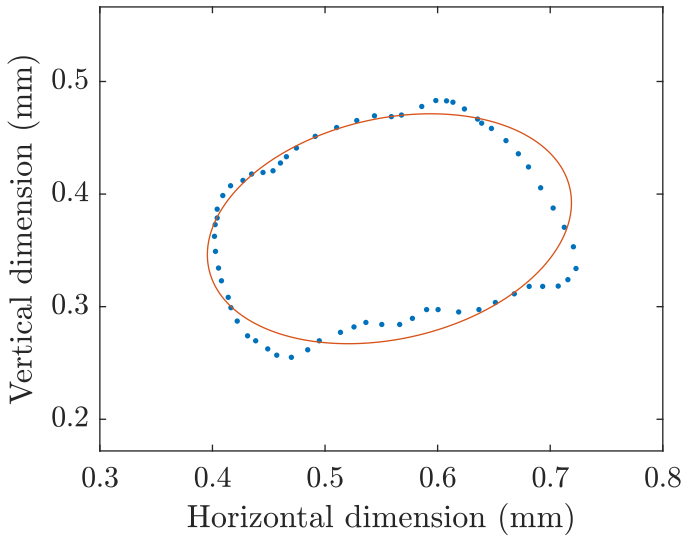

Figure 3.12: Ellipse fitted to particle outline vertex points.

to AutoCAD, and a polyline was created to estimate the particle outline. Vertex points were used to capture surface features of the particle as accurately as image resolution would allow. Capturing an in-focus image for every aspect of the particles is difficult, because the particles have some depth in the third dimension, which cannot be captured in the imagery. The final level of focus during imaging was selected by noting when the majority of the particle outline was clear. The vertex points of the polylines traced around the particle outlines were used to fit ellipses to the data sets, as discussed in S2.2.2. Figure 3.12 shows an example of an ellipse fitted to a particle outline. The major and minor axes of the fitted ellipses are utilized in §4.1 to create ellipsoidal models for each particle in efforts to recreate the grain-size distribution of each sediment sample.

Upon observing the narrow range of shape parameters in Table 3.3 for the sediment samples from the S10 sampling effort, the image analysis was expanded to one hundred

particles for the DTL sediment. The One hundred DTL particle images were used to investigate differences in shape characterization techniques for the fine beach sand of interest, with greater confidence in the statistical significance of the increased sample size of the particulate. Only shape analyses that produce comparable shape parameters between zero and one were employed for this investigation. In addition to the visual classification and fitted ellipse models of the one hundred DTL particles, measurements of the particles were made by fitting circles to the projection outlines, as was shown in Figure 2.3, and described by previous researchers (e.g., Santamarina et al., 2001; Santamarina and Cho, 2004; Mitchell and Soga, 2005; Cho et al., 2006). Figure 3.13 shows an example of a particle subjected to the measurement processes demonstrated in Figure 2.3.

The quantitative method described utilizing fitted circles to features of the particle outline to determine the inscribed circle sphericity and roundness was used to compare to visual estimations of roundness and sphericity. The shape classification comparison was employed to test the claim that various methods of defining roundness and sphericity do not vary significantly (resulting average values likely within 0.1, not exceeding 0.2 as stated by Santamarina and Cho (2004)). Visual shape classification and fitted ellipses were produced for the remainder of the one hundred DTL particle images (in addition to the original thirty-five particle images analyzed). Table 3.4 shows the arithmetic means of the shape parameters produced with visual shape classification from the Krumbein and Sloss (1963) roundness-sphericity chart, the measured circles approach, and the aspect ratio of the fitted ellipses (note that roundness cannot be determined from a fitted ellipse model).

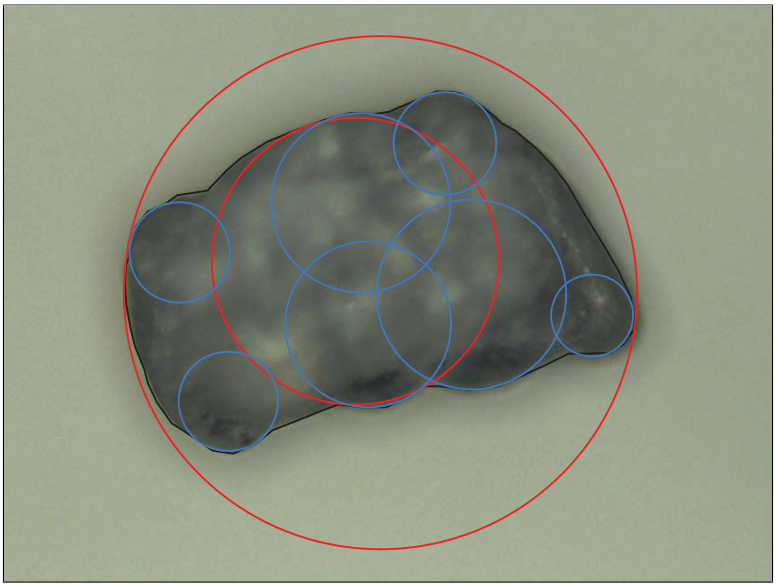

Figure 3.13: Circles fit to the surface features of a particle image in AutoCAD. Red circles show the largest inscribed circle and the smallest circumscribed circle possible for the particle geometry. Blue circles show circles fit to curvature features of the particle outline.

Table 3.4 shows that the ellipse aspect ratio exactly matches the visual classification of sphericity. The measured circles approach produces a lower value for sphericity, but remains within 0.1 of the values determined with the other classification methods. The visual and measured approaches to determine roundness are in close agreement. The evaluation of the shape analyses performed herein is presented in §4.1.2. The detailed particle shape analyses also inform the evaluation of correlations defined for shape parameters to other soil properties, including limiting void ratios and critical state friction angle.

DTL sediment from the S10 sampling effort is utilized for the remainder of the laboratory program to complete the characterization of the South Beach sand. Al-

Table 3.4: Roundness and sphericity estimations derived with various methods. The results shown are for one hundred DTL particles from the S10 sampling effort.

	Visual	Measured	Ellipse aspect ratio
s	0.74	0.66	0.74
r	0.36	0.39	-

though it is noted that beach sediments from the different sampling efforts and beach cross section locations exhibit slight variations, the sediment response is likely not greatly affected by the slight differences. The DTL sediment serves as one, consistent material to define the South Beach sediment as completely as possible in the remaining laboratory investigation.

3.2.3 Specific Gravity

As noted in §2.2.3, there is a narrow range of specific gravity values for typical soil constituents. To increase the accuracy of the selection of G_s for specimen packing density determination, as well as for providing the value for use in sediment transport applications, laboratory determination of specific gravity was performed. Guidance from ASTM D854-10 (2010) was followed to determine G_s for the South Beach sand. A triplicate test was performed on oven-dried DTL samples. The specific gravity was determined to be $G_s = 2.69$ (rounded from 2.6851). This results is reasonable in comparison with beach sands noted in the literature (see typical values provided in §2.2.3).

The environment in which the specific gravity tests were performed provided some limitations and slight deviations from procedures detailed in ASTM D854-10 (2010).

The temperature during testing was controlled as much as possible within the insulated container in which the pycnometers were placed, but the varying temperatures of the outer laboratory environment could not be regulated. The water quality used during testing may also not be of the specified quality. Distilled, deaired water is preferred in the ASTM standard. Deairing was performed by a combination of vacuum and heat applied to the water, but the purity of the available laboratory water was not verified. Varying water quality could slightly alter the resulting specific gravity value, but the reasonable range provided in the literature improves the confidence in the determined value.

3.2.4 Minimum and Maximum Void Ratio

To consistently prepare sand specimens of a specified packing density for strength testing (i.e., triaxial and simple shear testing), it is necessary to define the range of limiting void ratios. Defining the packing density range allows measurement of prepared specimens to define the density of the initially prepared state (i.e., the initial void ratio) before testing. The initial void ratio is a key contributor to the response of the material during shearing, because it specifies whether sediment is in a loose or dense arrangement. The influence of specimen density on the shearing response is detailed in §2.3.

The minimum and maximum void ratios were determined with guidance from ASTM D4253-16 (2016) and ASTM D4254-16 (2016), respectively, and are $e_{min} = 0.67$ and $e_{max} = 0.90$. Inadequate equipment and materials were available to perform

the standard ASTM procedure without deviation. A vertically vibrating table and weighted mold cover were not available in the respective laboratory, so the minimum void ratio was determined by horizontal tapping with a rubber mallet on test mold that had been filled with sand. The modified procedure may result in a higher value of minimum void ratio. The option to use a 'special mold' by ASTM D4253-16 (2016) was exercised, which is smaller than the standard mold and utilizes less sand during tests.

A sand (Southport sand) very similar in gradation and specific gravity is studied by Holubec and D'Appolonia (1973). The e_{min} value determined for the Southport sand with vibration by horizontal tapping, as well as e_{max}, agree very well with the results found for the South Beach sand. The results in Holubec and D'Appolonia (1973) show that the determination of the minimum void ratio with compaction vibration yields a lower value of the comparable sand by about 0.1. The study informs the prediction that the minimum void ratio found in true accordance with ASTM D4253-16 (2016) may be a lower value. The special mold was utilized to determine the maximum void ratio of the South Beach sand as well, but the air pluviation technique employed is thought to produce a reasonable value. The relationships presented in §2.3 allow the calculation of other measures of sediment packing density. The density classes ranging from very loose to very dense are presented in Table 3.5 along with the void ratio ranges and equivalent relative densities, D_r, porosities, n, and dry unit weights, γ_d (Lambe and Whitman, 1969).

Table 3.5: Packing density relationships. State classes after Lambe and Whitman (1969).

State	D_r (%)		e		n		γ_d (kN/m^3)	
Very loose	0	15	0.90	0.87	0.47	0.46	13.9	14.1
Loose	15	35	0.87	0.82	0.46	0.45	14.1	14.5
Medium	35	65	0.82	0.75	0.45	0.43	14.5	15.1
Dense	65	85	0.75	0.70	0.43	0.41	15.1	15.5
Very dense	85	100	0.70	0.67	0.41	0.40	15.5	15.8

3.3 Strength Testing

In addition to investigating the basic index properties of the beach sand from South Beach, Newport, Oregon, the response of the sediment to perturbation was also studied to determine the sediment strength properties. All strength tests were performed on DTL samples obtained during the S10 sampling effort. Consolidated-drained (CD) triaxial compression testing was performed under typical geotechnical confining pressures in order to observe the response and determine the general critical state friction angle of the South Beach sediment, which is a unique shear strength parameter, as discussed in §2.3. Simple shear tests were performed to observe the response of the sediment when subjected to a alternate shearing mechanism. Simple shear testing aims to mimic the type of shearing caused by bed-shear stresses, such as tsunami-induced bed-shear stresses. Simple shear tests on South Beach sediment were performed under typical geotechnical confining pressures, similar to the triaxial tests, to observe the general response of the sand at greater simulated depths. Consistent specimen preparation methods were performed for triaxial and simple shear testing in efforts to produce comparable results. In particular, specimens were air pluviated

using a funnel with minimal drop height. The specimen molds were then vibrated by tapping with a rubber mallet to reach the desired density conditions.

Simple shear tests were also performed under low confining pressures. Low confining pressures were employed to observe the altered response to perturbation of the South Beach sediment for a simulated state of the deposit approaching the surface (i.e., depths $\approx$ 3 m to 0.5 m). Additional methods for testing South Beach sediment were performed to observe the response of exposed sediment near the surface, including two different angle of repose testing techniques as well as inclined plane testing. As postulated by Sadrekarimi and Olson (2011), the angle of repose may estimate the critical state friction angle under low confinement. The proposed relationship is evaluated herein for South Beach sand in §4.2. Similarly, Booth et al. (2014) shows that the pocket-friction angle determined with inclined plane testing decreases as the number of particles interacting on the sediment bed increase. The investigation of gravel particles performed in the Booth et al. (2014) study simulated increasing particle interactions by lining up gravel particulate in a 'force-chain'. Herein, the pocket-friction angle of individual free particles is determined. The pocket-friction angle is then compared with peak frictions angles determined from low confinement simple shear testing in §4.2, in an attempt to observe the response as in situ conditions deviate from a continuum of soil particles.

Only the drained response (effective stress analysis) of the South Beach sand is studied herein. The effective stress analyses allow comparison between fully saturated (CD triaxial) and dry (simple shear) shearing test results, as well as the response of the dry sediment utilized in angle of repose and inclined plane testing. Neglecting

the undrained or partially drained response simplifies the respective investigation and allows meaningful comparisons of the sediment properties determined herein. As discussed in Chapter 1, the most relevant applications of the results of the current study are sediment instability and transport models for South Beach, Newport, Oregon. The nature of extreme overflow events, such as tsunamis, imposed on the South Beach sediment bed may result in a partially saturated environment, and the results of the sediment response determined herein should be utilized appropriately.

3.3.1 Triaxial Testing

The loading response of the South Beach, Newport, Oregon sand samples was initially investigated via consolidated drained (CD) strain-controlled triaxial compression tests on reconstituted samples using a GeoTac Sigma 1 device. Three tests at confining pressures, $\sigma'_3 = 50$, 100, 200 kPa, were performed. The noted confining pressures are near the lower range of typical geotechnical testing pressures, as discussed in §2.3. The oven-dried specimens were prepared by air pluviation using a funnel with minimal drop height followed by impact vibration with a rubber mallet on the specimen mold to obtain a loose relative density of about $D_r = 20\%$. A loose arrangement was desirable for triaxial testing so that the critical state response could be observed. The limited extent of strains possible with a triaxial device informed the decision to prepare loose specimens to limit the peak conditions during the loading response of the sediment, similar to the methods employed by Sadrekarimi and Olson (2011). The response of the loose specimens provided greater confidence in defining a critical

state friction angle, assuming that negligible dilation effects would be present at the termination of the test. The dry specimens (approximate initial height, $h_0 = 140$ mm, initial diameter, $d_0 = 71.5$ mm, and corresponding height to depth ratio of about 2) were saturated, as described in §2.3.1, under vacuum by slowly flowing approximately 500 ml of deaired water through the specimen (Head, 1998). Following the circulation of deaired water, back pressure within the specimen was increased to improve the degree of saturation, as recommended by Black and Lee (1973). The B values measured for the tests ranged between 0.90 to 0.96, measured with approximately 45 kPa effective stress to ensure that the specimen remained stable.

The discussion in §2.3.1 presents details of obtaining sufficient B values for triaxial testing. As noted by Black and Lee (1973), it may be impossible to obtain measured B values of one for soils other than soft clays. Black and Lee (1973) shows that a measured B value of only 0.69 for sands indicates approximately 99.5% saturation, which is stated to be satisfactory to perform soil tests with the assumption of full specimen saturation. For each test, the soil specimen was held at back pressure overnight to improve saturation. No additional increases of back pressure were performed once two B value checks produced results with a negligible difference, as suggested by Head (1998). The range of measured B values of the South Beach sand specimens herein ($B = 0.90$ to 0.96) were within the acceptable range defined by Black and Lee (1973) for the sand specimens to be considered as greater than 99.5% saturated and acceptable to test.

Once the specimens were sufficiently saturated, the cell pressure was increased until the desired consolidation stress was achieved. The altered height and density

Figure 3.14: Specimen at termination of triaxial test.

state of the specimen after consolidation was considered for the 100 and 200 kPa confining pressure tests, by observing the volume change during the consolidation phase. To complete saturation for the 50 kPa test specimen, the confining pressures were near the desired consolidation stress (45 kPa), so a difference in state between the saturation and consolidation phases could not be observed (i.e., $h_c \approx h_0$). Note that the volume change of specimens during saturation is very difficult to measure (Bardet, 1997).

The consolidated specimens were then subjected to shearing, and the specimens were allowed to drain, as noted in ASTM D7181-11 (2011, pg. 1) for CD triaxial testing, "specimens are consolidated and sheared in compression with drainage at a constant rate of axial deformation". The strain rate employed during shearing was 15%/hr ($\approx$ 0.35 mm/min), which produced a one hour shearing phase when termina-

Table 3.6: Estimated elastic moduli from the CD triaxial compression test responses.

Test	σ_3' (kPa)	ν	E_i (MPa)	E_{sec} (MPa)
T1	50	0.32	33.4	19.7
T2	100	0.30	57.4	38.5
T3	200	0.29	68.9	48.7

tion of the test is designated at 15% axial strain, as recommended by ASTM D7181-11 (2011). Figure 3.14 shows an example of a tested specimen at the termination of the CD triaxial test. The Mohr-Coulomb strength envelope is developed from the triaxial testing.

Figure 3.15 shows the stress-strain loading response and Figure 3.16 shows the volumetric response from the CD triaxial compression tests on South Beach sand specimens. Estimated elastic moduli are determined from the loading responses. As outlined in §2.3, the initial and secant slopes of the stress-strain responses, which were used to estimate the respective modulus of elasticity values, are shown Figure 3.15. E_i and E_{sec} are determined as the slopes between the origin and the axial strain at 10 and 50% of the maximum deviatoric stress, respectively. The average initial slope of the volumetric responses was utilized to estimate Poisson's ratio, as shown in Figure 3.16. Specific slopes of the initial portion of the volumetric responses were developed in preparation of producing the average Poisson ratio of $\nu = 0.3$. As discussed in §2.3, only deformations at very small strains should be employed to estimate elastic moduli. The determination of elastic moduli from the CD triaxial compression test results herein were estimated for small axial strains (i.e., $\varepsilon_1 < 1\%$). Table 3.6 shows the summary of estimated elastic moduli from the CD triaxial compression tests.

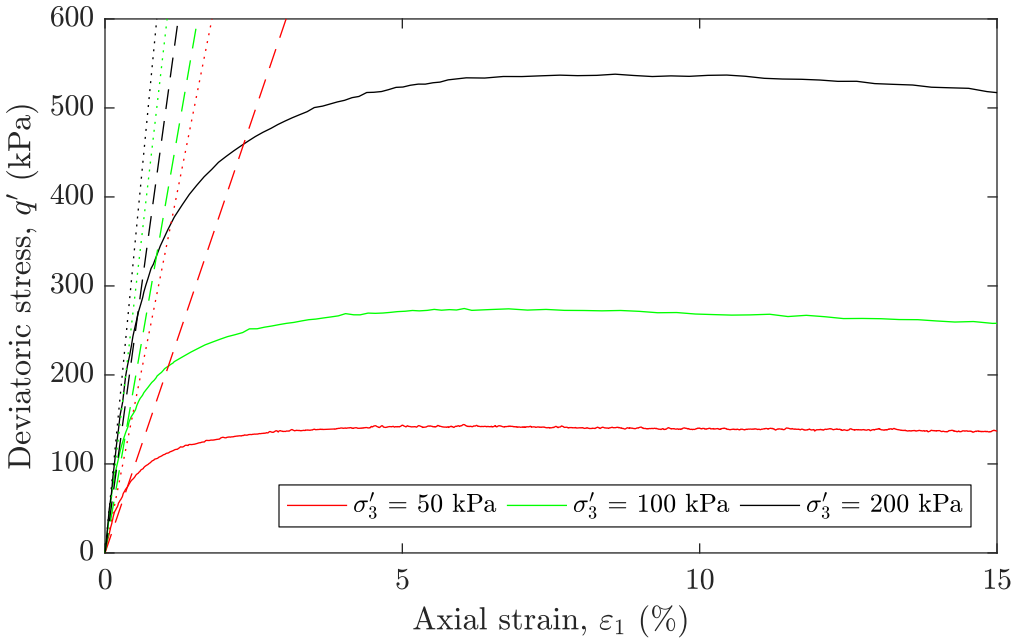

(a) Loading response during CD triaxial compression testing. Dotted lines of corresponding color show the slope for the initial modulus of elasticity for the respective response, E_i, and dashed lines show the slope for the secant modulus of elasticity, E_{sec}.

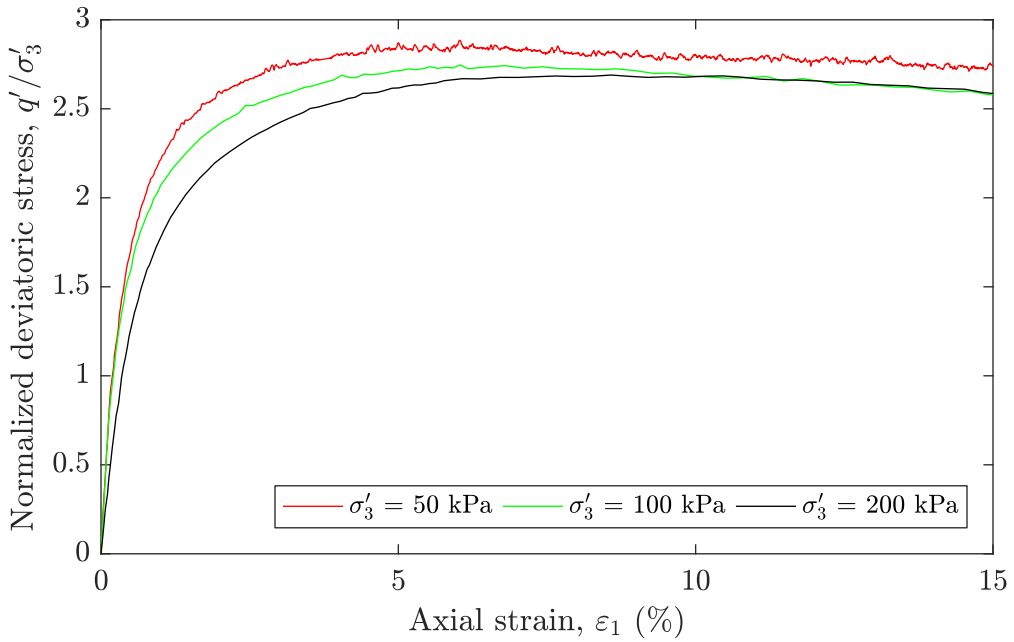

(b) Normalized loading response of the CD triaxial compression tests.

Figure 3.15: Loading responses from the triaxial tests.

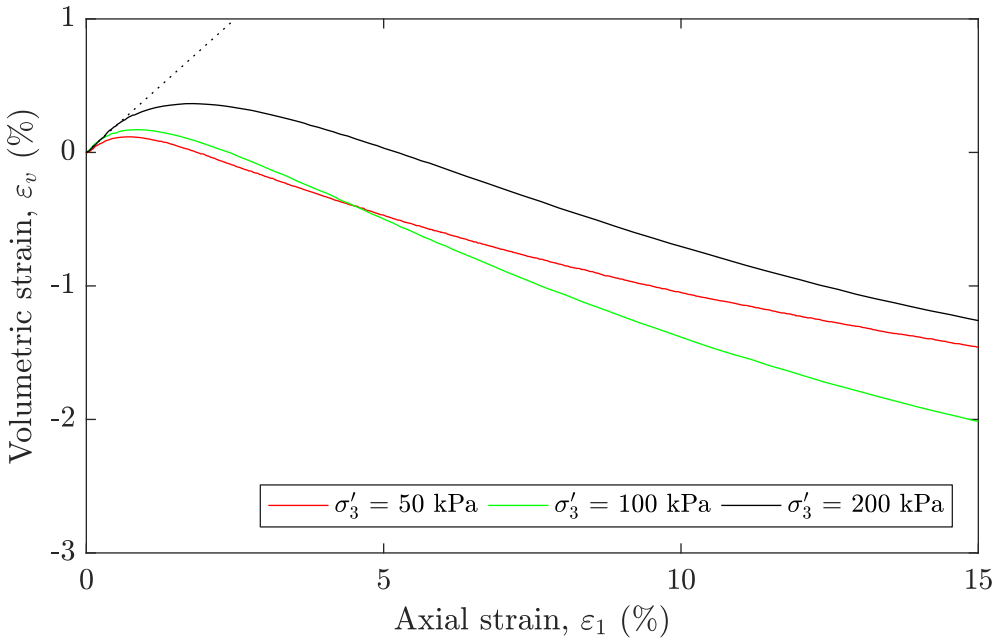

Figure 3.16: Volumetric responses from the triaxial tests. The dotted line shows the average initial slope of the responses to estimate Poisson's ratio, ν.

As expected, the loading response during CD triaxial compression testing did not exhibit significant dilation during shearing, because the tests were performed on relatively loose specimens under typical geotechnical confining pressures. Figure 3.16 shows that there is some dilation (negative volumetric strain) during shearing of the specimens; however, the response at the end of shearing ($\varepsilon_1 = 15\%$) appears relatively constant, which is sufficient to estimate critical state strength parameters. Figure 3.15b shows the normalized response of the CD triaxial compression tests, and notably, the $\sigma_3' = 100$ and 200 kPa tests collapse to the same value near the end of shearing. The $\sigma_3' = 50$ kPa test approaches a slightly higher constant value at the end of shearing. The difference in response of the $\sigma_3' = 50$ kPa test can likely be attributed

to the test being performed under confining pressures near the lower bound of typical geotechnical confining pressures, the effects of which will be discussed in detail in §4.2. Mohr circles were created from the three CD triaxial test results by plotting the respective major and minor effective principal stresses at 15% axial strain. Figure 3.17 shows the developed Mohr circles and corresponding friction envelope, assuming zero cohesion for the South Beach sand. The critical state friction angle for triaxial testing was determined to be $\phi'_{cs} = 34°$.

3.3.2 Simple Shear Testing

Strain-controlled, SGI-type simple shear testing was also performed on DTL samples from the S10 sampling effort to investigate the loading response of South Beach sand. Specimen preparation was performed with the same method (i.e., air pluviation with horizontal tapping on the specimen mold to densify) as triaxial testing; however, the target relative density of testing specimens was slightly greater for simple shear tests. As discussed in §2.2.3, the study by Atkins and McBride (1992) informs the assumption that a medium relative density is the approximated average in situ state of a variety of beach sands. Medium density sand specimens are also less sensitive to disturbance during testing preparation. It is desired herein to observe the loading response of South Beach sand for conditions similar to the in situ state, including the peak response and altered response under low confining pressures (i.e., shallow depths of embedment). The noted response observations are highly dependent on the state of the testing specimen, or the relative density.

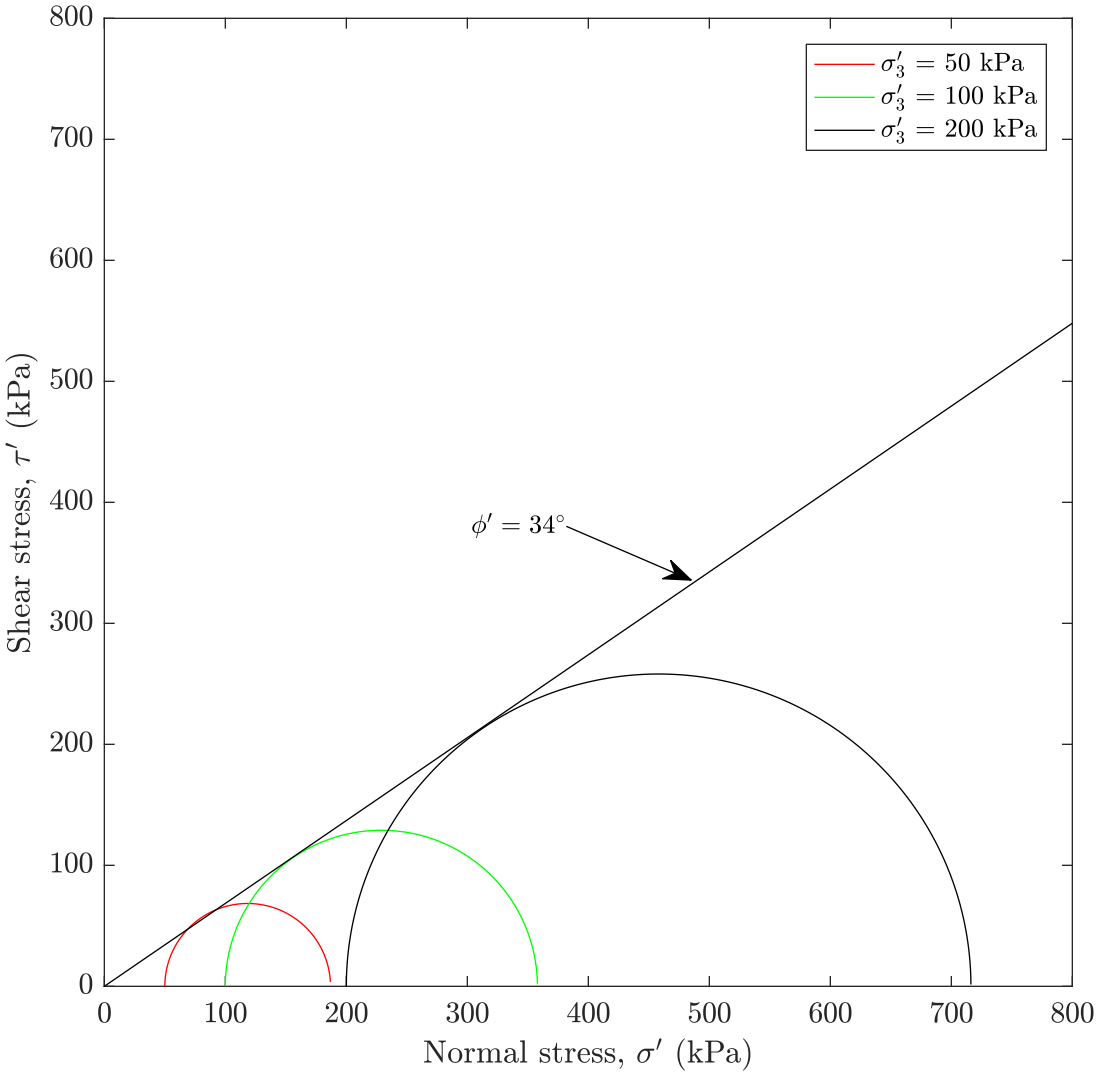

Figure 3.17: Mohr circles and failure envelope developed from the triaxial tests.

The Shear Trac II apparatus was assembled for simple shear testing (the device is also capable of direct shear testing) of dry sand specimens. The simple shear testing apparatus utilizes 29 Teflon coated confining rings to surround the specimen, each approximately 0.9 mm thick. The stack of rings rest on the specimen base surrounding the bottom porous stone platen. A specimen prepared within the confining rings and latex membrane had a diameter and height of approximately 64 mm and 24 mm, respectively. Deviations were made from the previous instructions developed for simple shear testing with the Shear Trac II apparatus, which utilized silicone vacuum grease to coat the sliding surface of the confining rings and adhere the membrane to the inner diameter of the confining rings (Kraupa, 2013). The confining rings coated with the silicone vacuum grease appeared to stick together and not allow a uniform specimen failure to occur.

All vacuum grease residue was removed from the confining rings and the Teflon coating on each ring was inspected. The surface of the rings were free of defects. The clean and dry rings could easily slide over each other when stacked and sheared. Lubrication of the rings with other substances, such as graphite lubricant, was considered herein [similar to the lubrication applied to stacked rings in a cyclic simple shear testing performed by Kwan and El Mohtar (2014)], but because the Teflon coating was intact on the SS confining rings, which have a low coefficient of friction [$\mu = 0.04$ for Teflon on Teflon (Tam, 2004)], no additional coating was applied. Application of an added lubrication layer to the confining rings raised concerns of repeatability and consistency between tests, especially when comparing results of tests under very low confinement pressures. If uneven lubrication was applied and varied with each

test, it could be difficult to determine consistent sediment response trends. Herein, a vacuum chamber was developed for specimen preparation, similar to the triaxial specimen mold apparatus that utilizes vacuum pressure. The specimen apparatus was placed in the vacuum chamber with the latex membrane sealed around the top opening and a low level of vacuum pressure was applied. The vacuum pressure slightly expanded the membrane to fit the inner diameter of the confining rings so that the inner surface was free of ridges and gaps. The noted process is similar to the specimen preparation technique performed for cyclic simple shear tests by Kwan and El Mohtar (2014).

As discussed, medium relative density specimens were used for simple shear testing. The specific target specimen relative density was defined as $Dr = 40\%$ (estimated range of prepared specimens was approximately between $D_r = 35$ to 45%, with corresponding void ratios of approximately $e = 0.82$ to 0.80). It should be noted that with such a small testing speciment utilized in the simple shear tests, differences in height measurements (≈ 1 mm) produced notably different relative density estimations. To limit the uncertainty produced by sensitive specimen height measurements, the average specimen height was determined via depth measurements from the surface of the confining ring stack to the specimen surface in four locations around the specimen perimeter.

The preparation and execution of simple shear tests is less involved than triaxial tests (i.e., 2 hour testing period versus 2 days). For this reason, more simple shear tests could be completed within the current study. A generally consistent initial specimen state allowed for peak and constant volume conditions to be compared between

simple shear test responses (especially important for observing trends from the low confinement testing). Unlike the triaxial compression testing performed in §3.3.1, the prepared specimens were not saturated. The Shear Trac II apparatus does not have the ability to regulate and measure water pressure within the specimen. Additionally, the surrounding water bath cannot be pressurized. To avoid the challenges involved with testing partially saturated specimens, dry testing specimens were used to ensure that the loading responses would be consistent and comparable.

Once the testing specimens were prepared and placed in the simple shear testing apparatus, a consolidation load was applied. Dry sand requires minimal time to consolidate; therefore, as soon as the extent of the vertical consolidation load was applied to the specimen and the system remained stable (i.e., vertical displacements stabilized), the shearing phase could begin. For consistency, the samples were consolidated for a minimum of five minutes before the shearing phase began. A shearing rate similar to that used in triaxial testing was selected (i.e., 0.3 mm/min), which corresponded to a shearing duration of approximately one hour. The final lateral displacement reached during simple shear testing was approximately $l = 14.5$ mm ($\gamma \approx 60\%$).

Initially, simple shear tests were performed with the same vertical effective confining pressures applied to the testing specimen as the isotropic confining pressures applied for triaxial tests, i.e., $\sigma'_v = 50$, 100, and 200 kPa, with an additional test performed at $\sigma'_v = 300$ kPa to ensure sufficient observation of the sediment response under typical confining pressures in the simple shear testing device. To determine the vertical load necessary to apply the desired vertical effective stress to the specimen,

components of the simple shear apparatus that would add weight to the specimen were accounted for. The loads that would be applied by the specimen cap, the plate used to obtain vertical displacement measurements with a linear variable differential transformer (LVDT), and the connecting rod, were determined and the applied vertical stress calculations were adjusted to ensure that the applied confining pressure during simple shear testing was not greater than anticipated.

Following the tests performed at typical geotechnical confining pressures (i.e., $\sigma'_v = 50$ kPa to 300 kPa), lower confinement pressures were applied to the specimens to simulate sediment response at shallower depths (i.e., $\sigma'_v = 6$ kPa to 40 kPa). As discussed in §2.3.2, there are challenges with low confinement testing. The response data becomes increasingly scattered and difficult to interpret with decreased confining pressures applied to testing specimens, which is a contributing factor to why low confining pressures are not typically employed in geotechnical laboratory tests. Figure 3.18 demonstrates the differences in the loading response for tests performed with typical confinement pressures (e.g., $\sigma'_v = 200$ kPa) and low confinement pressures (e.g., $\sigma'_v = 20$ kPa). Appendix A shows the response for each simple shear test performed herein. Figure 3.19 summarizes the shear stress measured during shearing (a), and the axial strain (i.e., volumetric response) measured during shearing (b), for all simple shear tests.

Figure 3.19a shows that generally, the measured shear stress is proportional to the vertical effective stress, and the response curves are sorted from top to bottom of the plot, from the largest confinement tests to the smallest confinement tests. A similar trend can be observed in Fig 3.19b. Generally, from top to bottom of the

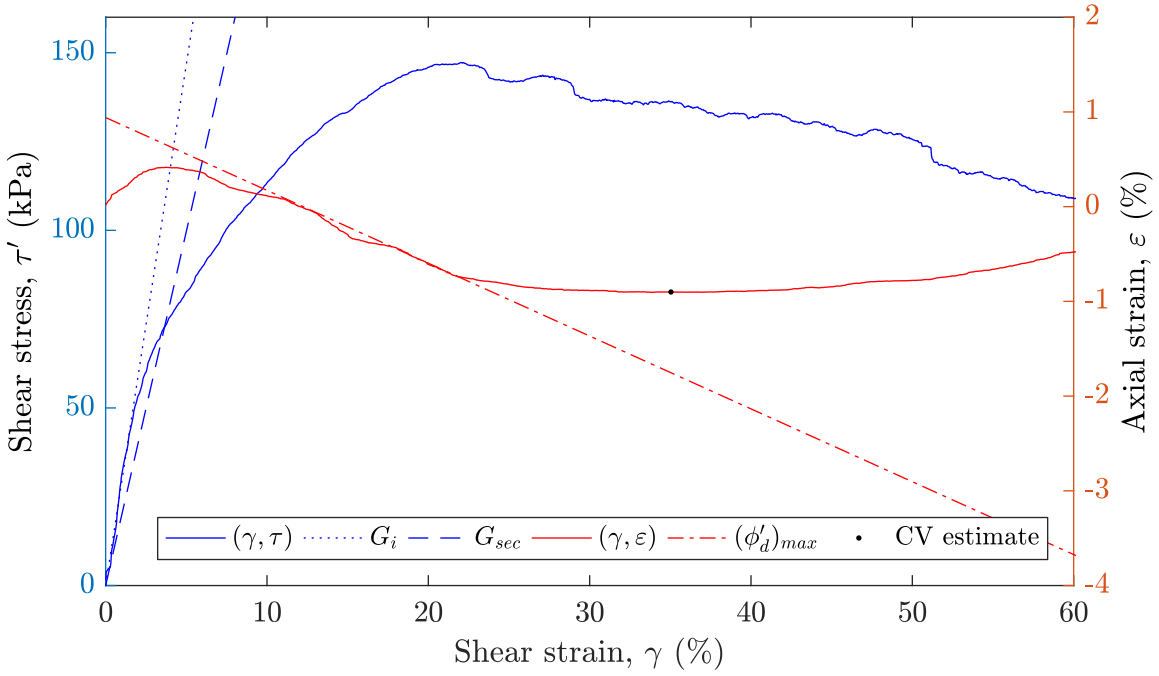

(a) $\sigma'_v = 200$ kPa simple shear test results

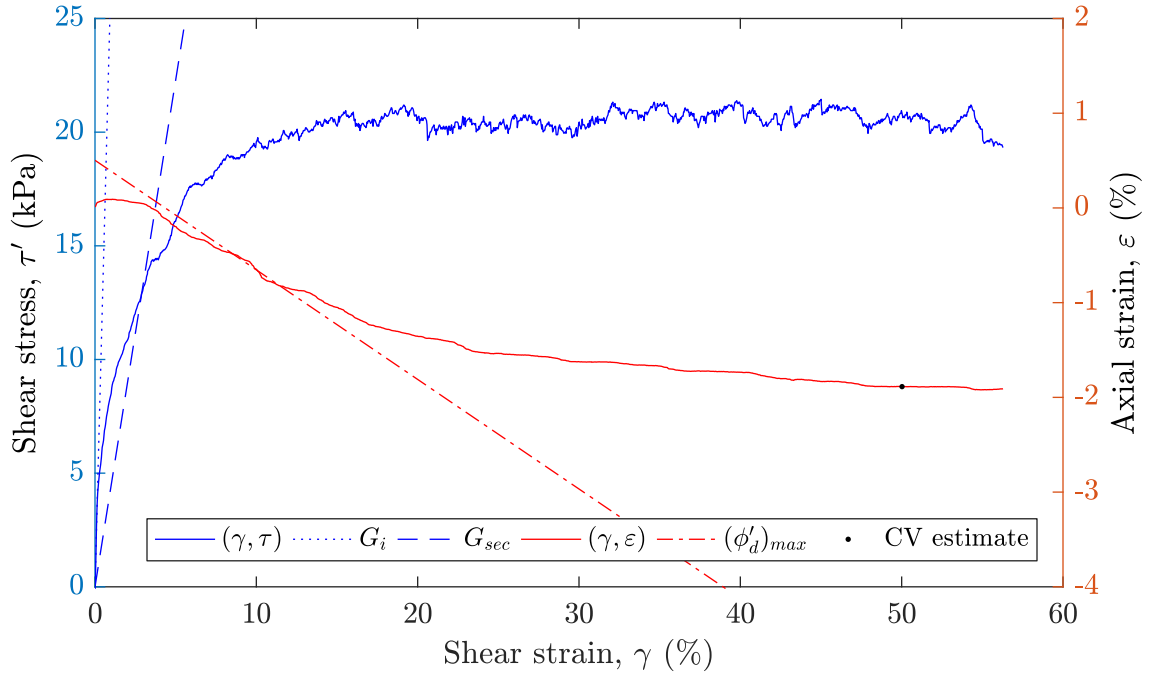

(b) $\sigma'_v = 20$ kPa simple shear test results

Figure 3.18: Example simple shear test responses.

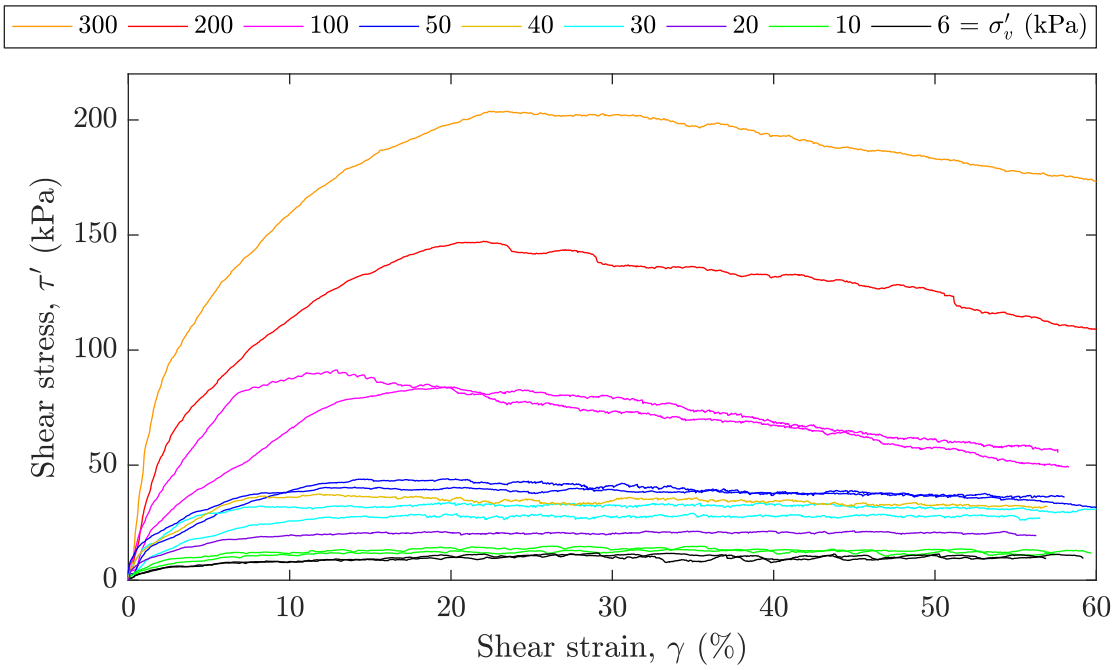

(a) Loading responses measured during shear

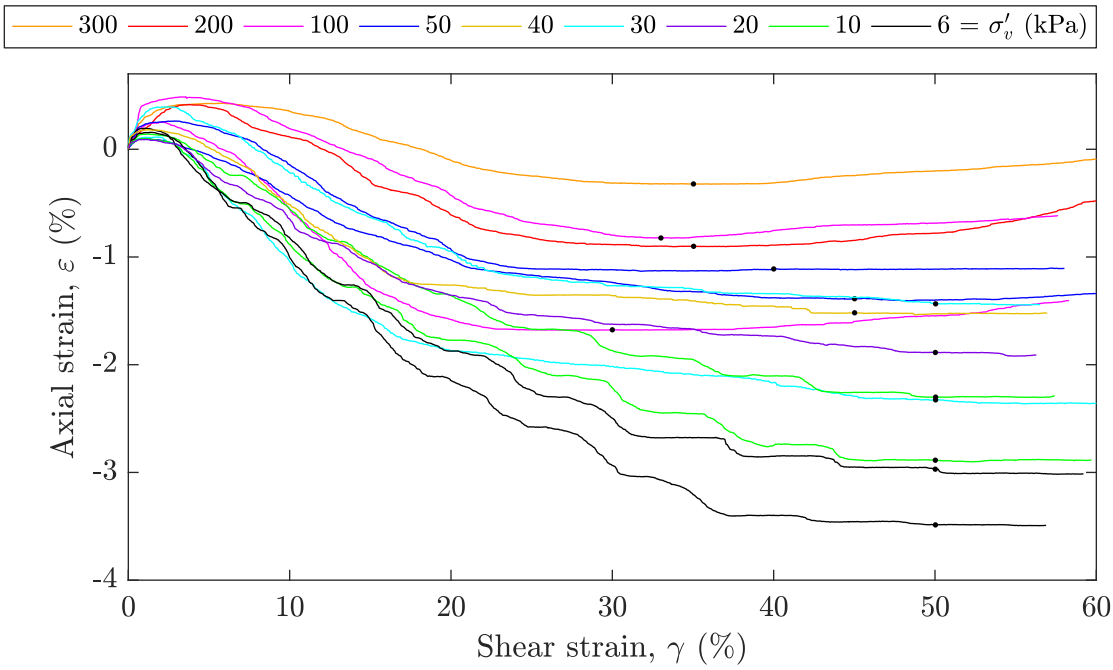

(b) Volumetric responses measured during shear

Figure 3.19: Summary of simple shear test responses.

plot, the highest confinement tests exhibit the least dilation, and the low confinement tests exhibit the most dilation. The axial strains (i.e., the volumetric responses) also show that to reach a constant volume state, the low confinement tests require more shearing (i.e., constant volume state occurs at greater shear strains). The trend of higher shear strains required to reach a state of constant volume was also observed by Stroud (1971) for tests on dry sands performed in the Cambridge simple shear device. Fig 3.19b shows the estimated points of constant volume for each simple shear test response, denoted with a black dot. A somewhat perplexing trend is seen in the volume change near the end of shearing for the typical confining pressure tests: the specimens appear to be contracting after fully dilating. The observed response could be caused by particle crushing, which was observed by Sadrekarimi and Olson (2011) during ring shear tests at high strains, but the corresponding shear stresses are not increasing during this phase, and during particle crushing, the shear stresses are expected to increase. The secondary contraction phenomena could also be due to further particle rearranging at large shear strains, because the higher confinement tests reach constant volume state at lower strains, and may require reorganization to reestablish constant volume shearing as the specimen experiences continued lateral displacement.

The linear relationship defined by the Mohr-Coulomb failure criterion, which was discussed in §2.3, informs the expectation that the measured shear stress normalized by the vertical effective stress should produce the same value at critical state. Figure 3.20 shows the normalized shear stress response for all simple shear tests. Tests performed with confining pressures between $\sigma'_v = 100$ and 300 kPa approach nearly

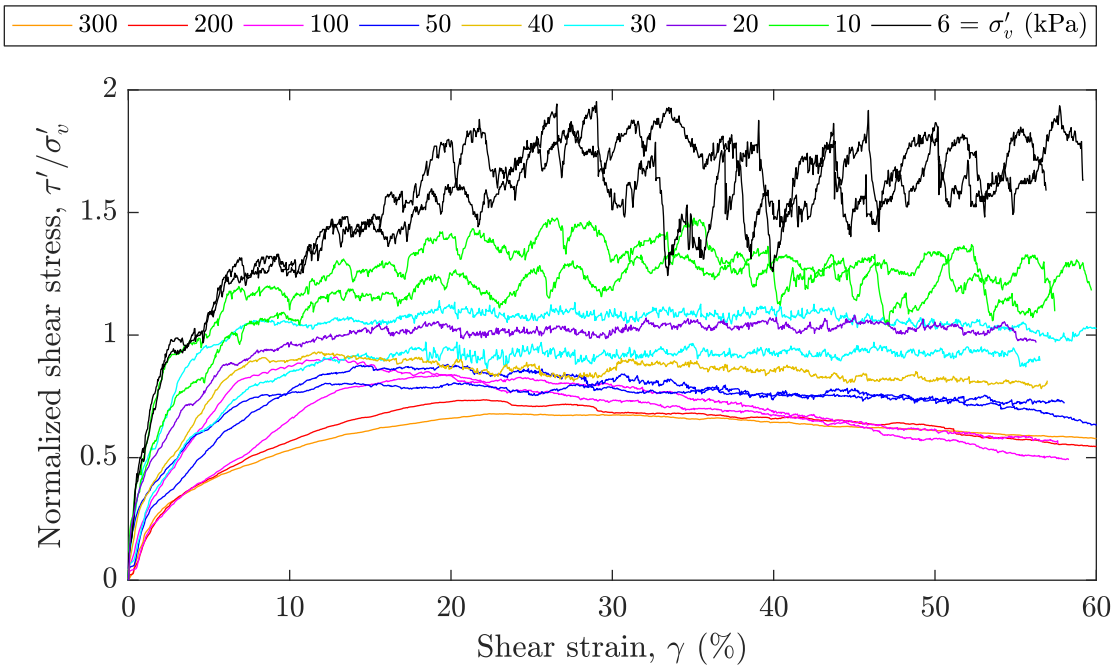

Figure 3.20: Normalized loading responses for all simple shear tests.

the same value of normalized shear stress towards the end of the shearing phase ($\gamma \approx 40\%$). For tests performed at confining pressures $\sigma'_v = 50$ kPa and below, the normalized shear stresses throughout the responses become much larger (normalized shear stress increasing with decreasing confinement). The increase in normalized shear stress for low confinement test results indicates an increase in friction angle, thus deviating from the linear Mohr-Coulomb failure criterion.

Simple shear testing with the SGI-type device does not determine the complete stress path and stress tensor within the specimen throughout shearing, as discussed in §2.3.2. The major principal stresses at the beginning of the test is defined as the applied vertical effective confining stress, but no measurements of the minor principal stress can be obtained. Normal and shear stresses throughout simple shear testing

are measured at the specimen apparatus boundaries, but the orientation of the failure plane is not known. A unique Mohr circle of stress cannot be constructed for simple shear test responses, because the principal stresses and the orientation of the failure plane throughout the test are not defined.

To obtain an estimation of the friction angle from simple shear results, assumptions must be made about the failure plane, as discussed in §2.3.2. Herein, Equation 2.19 is utilized to estimate the friction angle from the simple shear test responses, which assumes that the horizontal plane is the plane of maximum stress obliquity (Airey et al., 1985). The study performed by Wijewickreme et al. (2013) aides in verifying that the friction angle determined from simple shear tests is well estimated by Equation 2.19, especially for larger shear strains. Figure 3.21 shows the estimated mobilized friction angle calculated by Equation 2.19 throughout shearing. The shape of the curves in Figures 3.20 and 3.21 are very similar, because the estimated friction angle is the inverse tangent of the normalized shear stress.

To obtain comparable values of the mobilized friction angle, values for two conditions of the simple shear tests were compared: peak and constant volume. The peak friction angle can be determined by observing Figure 3.21; however, the estimated friction angles from low confinement tests responses become increasingly variable, and the identification of a single peak value is difficult. As observed by the constant volume points plotted in Figure 3.19b, the constant volume state is reached at various shear strains for the simple shear tests. The simple shear specimens appear to reach constant volume between $\gamma = 30$ to 40% for the typical confining pressure tests, and near $\gamma = 50\%$ for the low confining pressure tests. To make the selection of mobilized

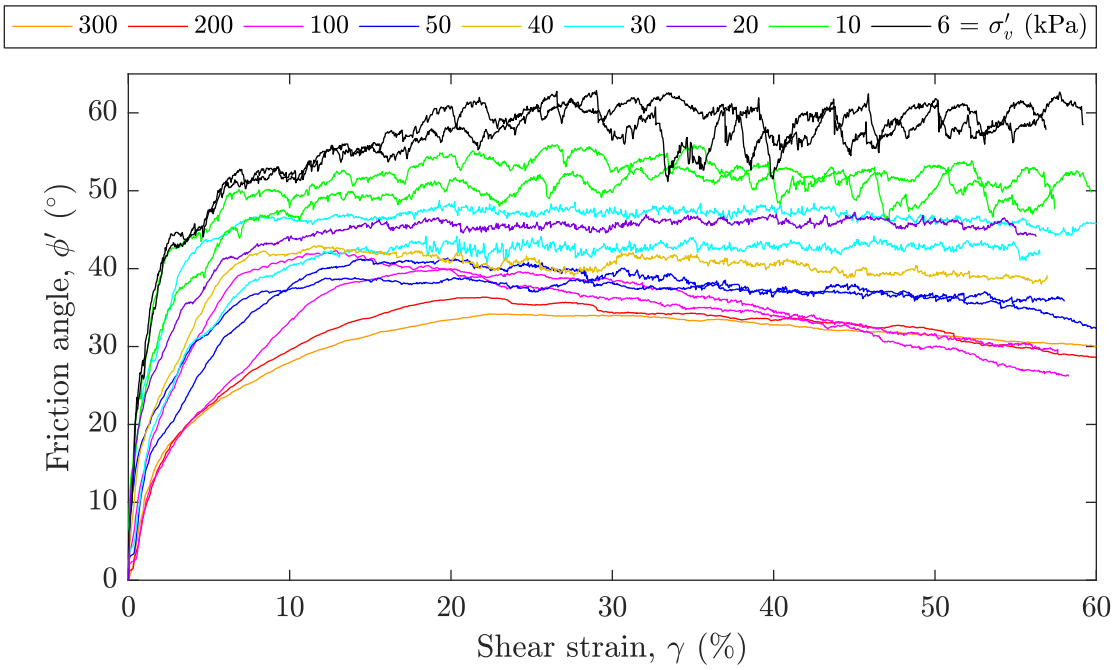

Figure 3.21: Estimated mobilized friction angle from simple shear test responses.

friction angle at constant volume state less variable between narrow ranges of shear strain, a median filter considering one hundred and one datapoints was applied to the estimated friction angles shown in Figure 3.21 to smooth the results. Figure 3.22 shows the smoothed estimation of mobilized friction angle throughout shearing for each simple shear test.

From Figure 3.22, the peak mobilized friction angle was defined as the maximum observed friction angle, ϕ'_p, and the mobilized friction angle value at the shear strain corresponding to constant volume state for each test was defined as the constant volume friction angle, ϕ'_{cv}. If the applied vertical consolidation stress is correlated to an equivalent depth below the surface of a simulated dry, medium density sediment bed (calculated by dividing the vertical effective stress by an average dry density

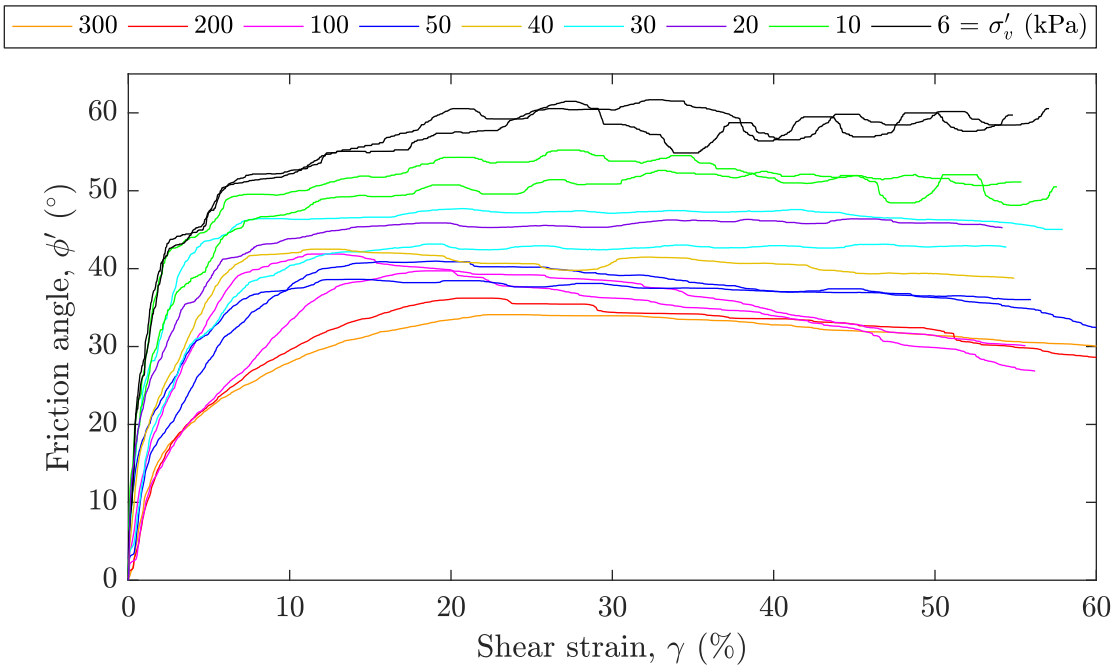

Figure 3.22: Estimated mobilized friction angle from simple shear test responses (Median filter N = 101).

value of γ_{dry} = 14.5 kN/m^3 for D_r = 40% conditions), then the estimated friction angles described previously may be plotted as a function of depth. Figure 3.23 shows the peak and constant volume friction angles as a function of depth below the ground surface.

As discussed in §2.3, the dilation angle is defined as the difference between critical state and peak friction angles. If the constant volume friction angle is assumed to be critical state, then the dilation angle can be estimated from the difference between the corresponding points in Figure 3.23. The dilation angle can also be estimated from the volumetric response during specimen shearing (Bolton, 1986). To determine the maximum dilation angle from the volumetric responses shown in Figure 3.19b,

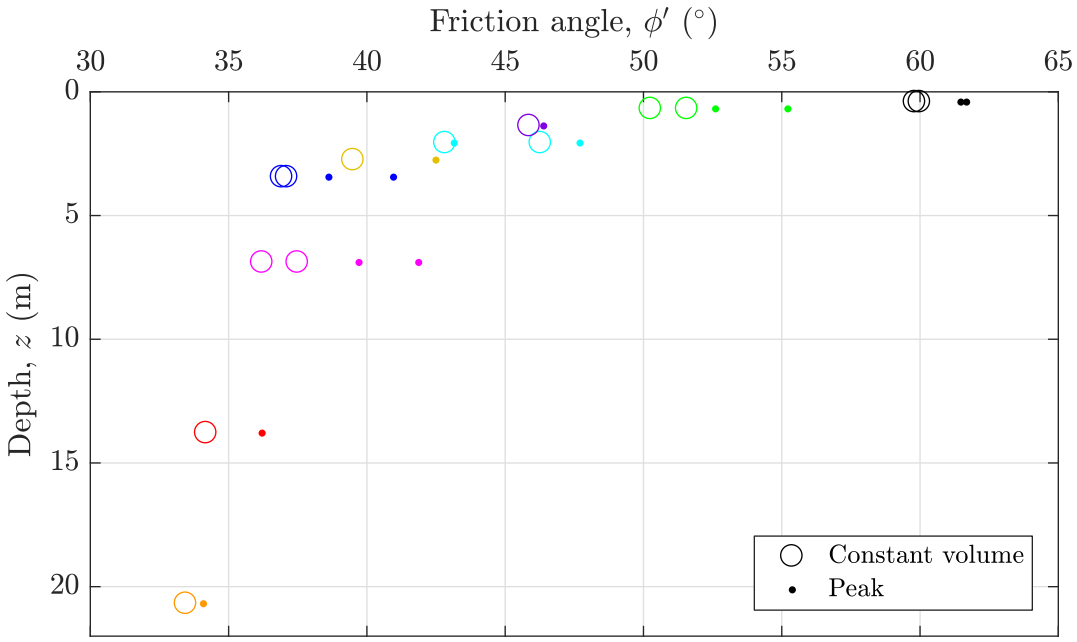

Figure 3.23: Estimated friction angles from simple shear test responses as a function of depth.

the maximum slope during specimen dilation was estimated with a linear fit. The maximum dilation angle is defined as the inverse tangent of the maximum dilative slope of the volumetric response. Examples of the determination of the maximum dilative slope of the volumetric response for simple shear tests are shown in Figure 3.18 as the $(\phi'_d)_{max}$ line (the process is shown for all simple shear test responses in Appendix A).

A similar estimation of the dilation angle from the volumetric responses of the simple shear tests can be determined from Equations 2.21 and 2.22, given by Rossato and Simonini (1991) and Houlsby (1991), respectively. From the axial and shear strains measured during simple shear responses, Equation 2.21 estimates the principal

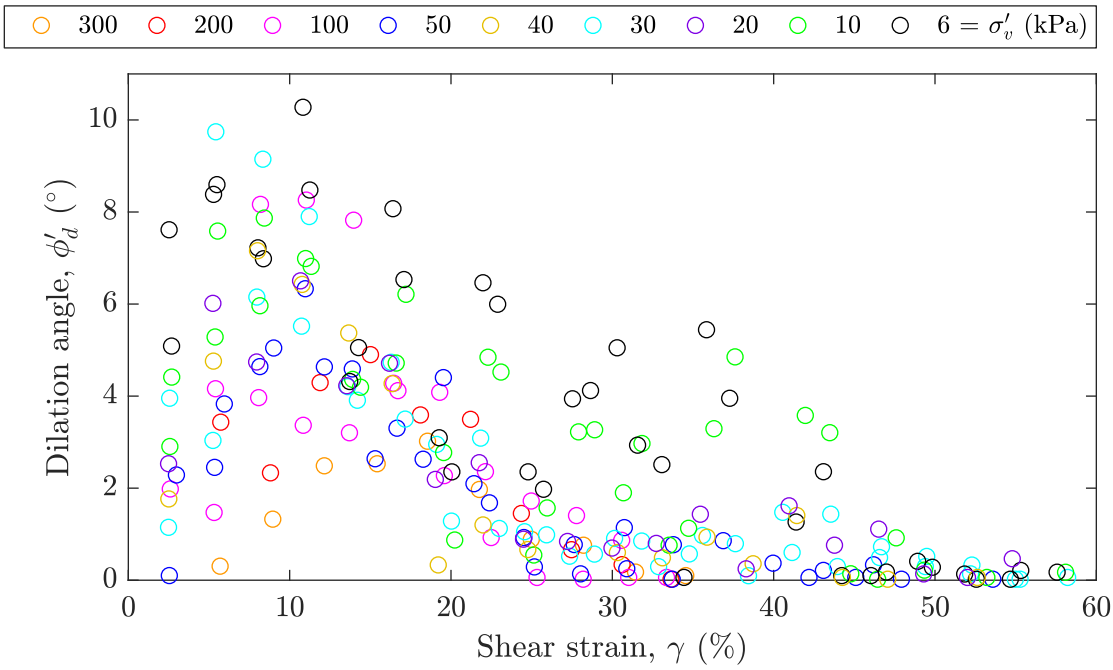

Figure 3.24: Incremental dilation angles throughout simple shear test responses.

strains throughout the tests. Then, Equation 2.22 can be utilized with incremental principal strain inputs to determine estimated dilation angles throughout the simple shear test responses. The estimation of incremental dilation angles using Equation 2.22 is determined by considering a span of sixty principal strain estimations from Equation 2.21 centered at twenty strain increments throughout the response. This process designates values of incremental strains as inputs to Equation 2.22. Figure 3.24 shows the estimated incremental dilation angles throughout the shearing phase for each simple shear test response. Generally, larger dilation angles were observed with lower confining stresses, indicating that the specimens confined with less vertical effective stress experienced more dilation during shearing, a trend which is supported by the axial strains observed in the volumetric response shown in Figure 3.19b.

The maximum dilation angles determined by the methods of determining the maximum slope of the volumetric responses and by the use of Equation 2.22 given by Houlsby (1991) are tabulated for each simple shear test in Table 3.7 as $\phi'_d = f(\gamma, \varepsilon)$ and $\phi'_d = f(\varepsilon_1, \varepsilon_3)$, respectively. The trends in dilation angles that are derived as a function of the volumetric strains appear to be notably larger than the difference between peak and constant volume friction angles observed in Figure 3.23. The maximum dilation angles reported in Table 3.7 show increasing dilative trends for simple shear tests with low confining pressures, up to about $\phi'_d = 11°$. With notable dilative behavior observed in the volumetric responses, the loading response showing measurements of shear stresses throughout the simple shear tests shown in Figure 3.19a or 3.20 should show defined peak and post-peak behavior. However, it appears that the simple shear testing apparatus fails to capture the dilative response in the shear stress measurements of low confinement tests.

The two sets of maximum dilation angles reported in Table 3.7 agree within 1°. As shown in Figure 3.24, the incremental dilation angles determined from Equation 2.22 show high variability, and because the prescribed increments are based off of constant shear strain ranges, important features of the volumetric response may be neglected. Maximum dilation angles estimated by determining the maximum slope of the volumetric response allows discretion when fitting a linear trend to the shear strain range where maximum dilation is observed, which also requires less assumptions than utilizing Equation 2.22.

If the estimated peak friction angles shown in Figure 3.23 are used in combination with the maximum dilation angle estimated from the more straightforward approach

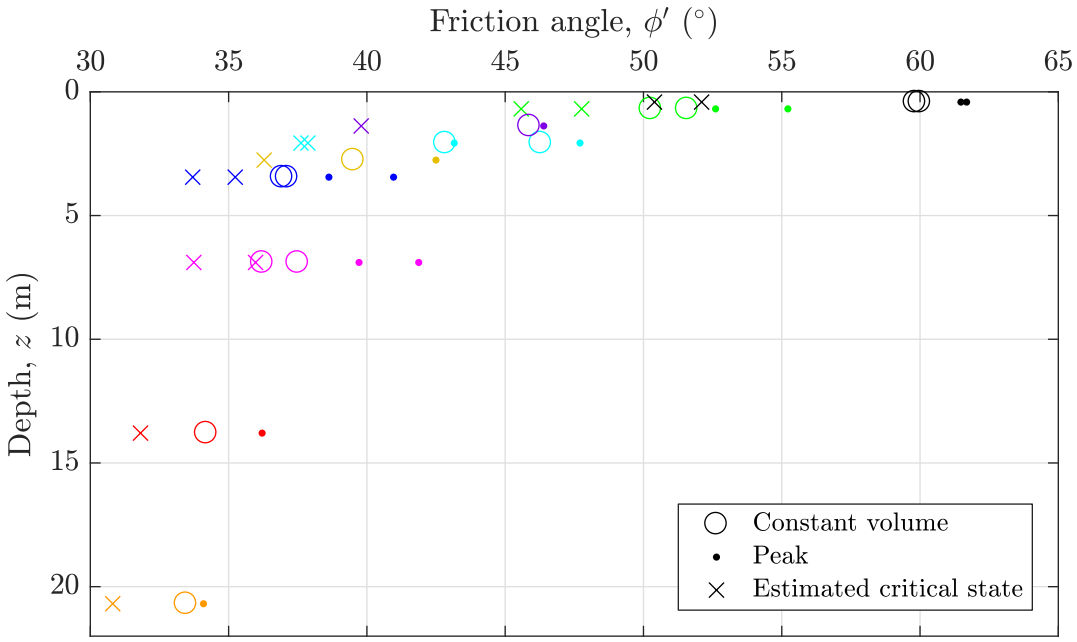

Figure 3.25: Estimations of critical state friction angle.

of determining the maximum slope of the volumetric responses, then the critical state friction angle can be estimated by deducting corresponding maximum dilation angles from estimated peak friction angle. Figure 3.25 shows the estimated friction angles presented in Figure 3.23, with the addition of the critical state friction angle estimated with this simplified approach.

Elastic moduli describing the deformation of the specimens before failure for each simple shear test response were estimated. As shown in Figure 3.18, the initial and secant shear moduli, G_i and G_{sec}, are determined from the average slope of the (γ, τ') curves, from the origin to 10% and 50% of the maximum shear stress, respectively. In addition to the simple shear test response examples shown in Figure 3.18, the estimation of the elastic moduli for each simple shear test is shown graphically in

Table 3.7: Elastic moduli and maximum dilation angles derived from simple shear responses.

Test	σ'_v (kPa)	G_i (MPa)	G_{sec} (MPa)	$\phi'_d = f(\gamma, \varepsilon)$ (°)	$\phi'_d = f(\varepsilon_1, \varepsilon_3)$ (°)
SS1	300	5.62	3.36	3.3	3.0
SS2	200	2.93	1.99	4.4	4.9
SS3	100	2.52	1.48	8.1	8.2
SS4	100	1.44	0.80	3.7	4.3
SS5	50	4.44	0.81	4.9	5.0
SS6	50	0.91	0.53	5.7	6.3
SS13	40	1.65	0.69	6.2	7.1
SS7	30	1.84	0.87	9.8	9.7
SS8	30	0.63	0.48	5.5	6.1
SS14	20	2.72	0.45	6.6	6.5
SS9	10	0.77	0.38	7.5	7.8
SS10	10	0.54	0.23	7.0	7.0
SS11	6	0.37	0.20	9.4	8.6
SS12	6	0.40	0.19	11.3	10.3

Appendix A. The estimated shear moduli generally decrease with decreasing simple shear confining pressures. Table 3.7 shows the estimated elastic moduli for each simple shear test response.

It should be noted that herein, some simple shear tests were performed with the same confining pressures. It was beneficial to observe the consistency, or lack thereof, of duplicate tests. It is also important to note that a contribution to the measured data is likely from unintended forces applied from the resistance of the simple shear testing device. This effect is especially important for low confinement results, because the unintended system resistance forces produce a larger contribution to the small shear stresses measured throughout the simple shear test response. The effects of system resistance on the simple shear test responses is investigated in §4.2.

A number of additional factors may affect the simple shear test responses. During specimen preparation, it was necessary to slightly adjust the specimen top cap to create a level surface so that the prepared specimen apparatus would fit properly into the simple shear testing apparatus. The minor specimen top cap adjustments likely imposed slight pressures on the specimen. It is assumed that the pressures imposed on the testing specimens from the specimen top cap adjustments during testing preparations were less than the pressures imposed during the specimen consolidation. This assumption becomes less robust with low confinement testing, because lower consolidation stresses are applied to the specimen; therefore, possible overconsolidation of the specimen may have occurred. The repetition of some low confinement simple shear tests helps to improve confidence in the results as well as demonstrates the extent of the effects of potential uncertainties on the simple shear test responses.

During specimen preparation, some initial displacements could be imposed, even when the stack of confining rings are locked in position with the stabilizing pins. Slight shifting of the ring stack could also occur during system alignment to allow the loading rod to properly thread into the specimen top cap. During the threading of the loading rod into the specimen top cap, a slight rotation and resulting torsional force may be imposed on the specimen. The possible specimen disturbances during testing preparation limit the confidence that simple shear testing specimens remain at the desired initial state prior to the consolidation and shearing phases. The limitations are especially important when postulating trends from low confinement simple shear test responses.

The analysis of the simple shear results also employs many assumptions, as dis-

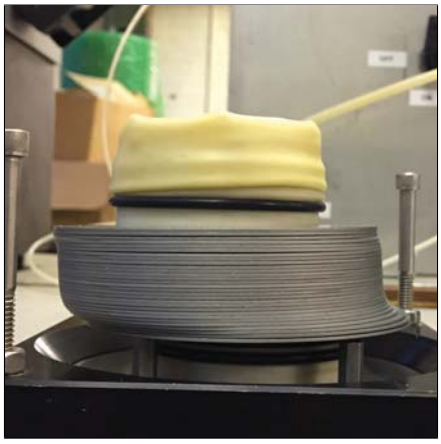

(a) Specimen with rings

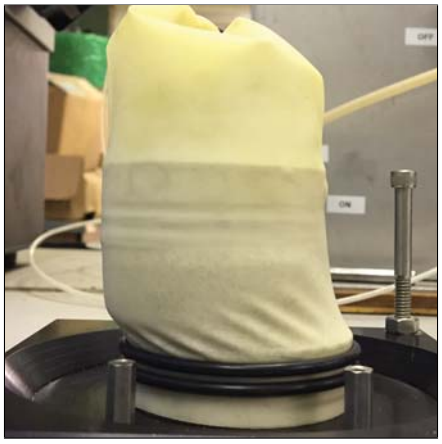

(b) Specimen without rings

Figure 3.26: Specimen after termination of simple shear test.

cussed in §2.3.2. The analysis of simple shear testing assumes that plane strain conditions are valid throughout the testing. There are also some assumptions about the symmetry of how the specimen shears during testing. Figure 3.26 shows a tested specimen, with and without the confining rings. To obtain the image of the tested specimens without confining rings, the rings were removed one at a time, without greatly disturbing the specimen. It is evident that the SGI-type simple shear apparatus utilized herein does not symmetrically shear the testing specimens.

3.3.3 Angle of Repose Testing

Several methods are available to determine the angle of repose of granular materials, as discussed in §2.3.3. Guidance from the literature suggests that ASTM C1444-00 (2000) is a consistent method that produces the angle of repose (Rousé, 2014), and the procedures developed by Santamarina and Cho (2001) produce an estimation of the

critical state friction angle through an angle of repose estimation measured by tilting a graduated cylinder filled with sediment and measuring the angle once stabilized. To determine the angle of repose herein, the two noted methods were performed and are pictured in Figure 3.27.

ASTM C1444 determines the angle of repose for free flowing powders. The standard notes that particle size, shape, and bulk density have an effect on the flowability of powder material. A funnel with a spout diameter of about 9 mm was used and and secured in position with the bottom of the spout approximately 38 mm above the flat counter top surface, with a sheet of gridded copier paper secured in place. The distance between the bottom of the funnel spout and the gridded paper was measured at three places along the spout perimeter to ensure the 38 mm target distance. While blocking the spout outlet, the funnel was filled about one third to one half full (mass of approximately 200 g) of South Beach sand. The funnel spout was then exposed to allow the sand to flow from the funnel. More sand was added to the funnel continuously to maintain a steady flow from the spout opening. The addition of sand to the funnel was ceased when the top of the developing sand cone reached the bottom of the funnel spout, thus stabilizing the cone.

A caliper was used to take four diameter measurements of the base of the cone. The procedure described was repeated three times for each angle of repose calculation. The complete ASTM C1444-00 (2000) angle of repose test was performed ten times (i.e., thirty individual sand cones formed) to increase the confidence in the results and determine the consistency of the test. The arithmetic mean of the angle of repose determined with ASTM C1444-00 (2000) procedures is 38° with a standard deviation

(a) ASTM C1444 (b) Santamarina and Cho (2001)

Figure 3.27: Angle of repose testing apparatuses.

of 1° for the investigated South Beach sand.

It was observed that the fixed funnel, which the sand was poured into, moved slightly with the weight of the sand shifting throughout the test. The slight movement of the funnel could affect the actual height of the spout above the gridded paper surface, thus deviating from the 38 mm specification. As noted by Train (1958), the cone formed during this method often shifted during the cone measurement process, thus creating a larger diameter cone, resulting in calculations of lower angle of repose. Efforts were made to not disturb the sand cone while measuring the diameter at the cone base, and only very slight shifts of the sand cone were observed during measurements. During several tests, the sand flow from the funnel ceased prior to the tip of the developing sand cone reaching the bottom of the funnel spout. The funnel

was tapped slightly to resume the flow, but cones created following the ceased flow condition often produced a slightly larger sand cone diameter.

The method described by Santamarina and Cho (2001) was also utilized to estimate the angle of repose of South Beach sand. The procedures to determine the angle of repose, which aimed to estimate the critical state friction angle of the sediment, required that the South Beach sand be poured into a graduated cylinder filled with water. The graduated cylinder is then tilted at least 60° then slowly returned to the vertical position. The angle that the sediment forms in the graduated cylinder at rest is then measured at the middle region of the slope as the angle of repose. Santamarina and Cho (2001) states that a transparent rectangular container used as the graduated cylinder is preferred; however, this type of graduated cylinder is not typical and was not available in the geotechnical laboratory where testing was performed.

The respective submerged angle of repose testing did not appear to be appropriate or provide accurate results for the South Beach sand investigated. Santamarina and Cho (2001) notes that the measurement of the angle of repose under water is preferred to avoid capillary forces influencing the results. However, it was also noted that procedures determining the angle of repose under water may be inappropriate for liquefiable soil specimens, because the soils may liquefy during tilting of the graduated cylinder, resulting in a lower value of the angle of repose. The South Beach sand was observed to liquefy during the described procedure, and produced a lower angle of repose, typically less than 30° [lower than the critical state friction angle determined with CD triaxial compression testing and the angle of repose determined via ASTM C1444-00 (2000)].

To determine the angle of repose for liquefiable soils, Santamarina and Cho (2001) suggest an equivalent dry procedures. Oven dried South Beach sand was poured into a clean and dry graduated cylinder and then tilted as previously described. Twenty measured angles of repose with the dry procedure resulted in a higher measured angle of repose of 36°, with a standard deviation of 5.5°. The angle of repose resulting from the dry approach of tilting a graduated cylinder is notably more variable than the angle of repose estimates determined with ASTM C1444-00 (2000) procedures. With a cylindrical container, as utilized herein, it is difficult to measure the angle of repose. Photos were taken of the stabilized South Beach sand within the graduated cylinder, and AutoCAD was utilized to draft lines over the images that produced angular measurements of the slopes. The horizontal markings on the graduated cylinder served as guides to compare with the drafted AutoCAD lines to obtain the angles of repose. The curvature of the graduated cylinder made the measurement somewhat subjective.

Herein, the reported angle of repose is that resulting from ASTM C1444-00 (2000) procedures, given as $\phi'_{Rep} = 38°$.

3.3.4 Inclined Plane Testing

Inclined plane testing was performed to determine the pocket-friction angle of the South Beach sand investigated. To prepare the rough boards of fixed sand particles to serve as 'inclined planes', flat wooden boards were sanded slightly to smooth the surface and wiped clean. A thin layer of spray adhesive was then applied to the clean

Figure 3.28: Inclined plane apparatus.

and dry boards. Oven dried South Beach sand was then poured over the adhesive to cover the surface of the boards. Excess sand was removed and the boards were left to dry overnight. The prepared boards were tapping against the counter slightly to remove any additional excess sand. Two boards were prepared for testing herein to observe the variation in results. The described preparation of the rough boards of fixed sand particles is similar to the methods performed by Miller and Byrne (1966). The prepared boards could then be placed into position for testing, by aligning an edge of the board with a secured protractor at the edge of a flat counter surface. Another edge of the board was then aligned with a stop-pad to hold the board in place during inclination. Figure 3.28 shows a prepared rough board of fixed sand particles set into position.

Initial testing trials utilizing the prepared boards with free sand particles placed

on the rough surfaces showed that no particles were displaced from their position on the tilted rough board before an inclination angle of about 40°. Following the initial observation of incipient motion of the free particles (i.e., initiation of particle movement from the at-rest position), the boards could be propped to begin testing at 40°. The stand used to prop a rough board in the fixed position could then be slowly advanced towards the base of the board, terminating at the stop-pad, to increase the inclination angle. An average rate of inclination was determined to be approximately 0.5°/s, determined from recorded video footage of inclined plane tests. For all inclined plane tests, a camera was fixed in position to observe the angle when free particle incipient motion began. To make this observation, a clean sheet of paper was placed at the base of the rough board so that the camera could capture sediment particles against the white background.

Previous works that have performed similar inclined plane tests (e.g., Miller and Byrne, 1966; Booth et al., 2014) tracked free particle incipient motion by observing microscopic images of the rough board, focusing on the movement of the free particles. Herein, a simplified approach for inclined plane testing was performed that utilized a video camera to capture the displacement of free particles from the rough board. It is assumed that the board was advanced slowly enough that the moment at which the particle appeared on the clean sheet of paper was representative of failure angle for the initial motion of the particle, or slightly after the actual moment of failure, which would lead to a slightly larger observed failure angle ($\leq 1°$). The definition of free particle incipient motion, or failure, is shown visually in Figure 3.29. To perform inclined plane testing for the free particles of interest, a small scoop of oven-dried

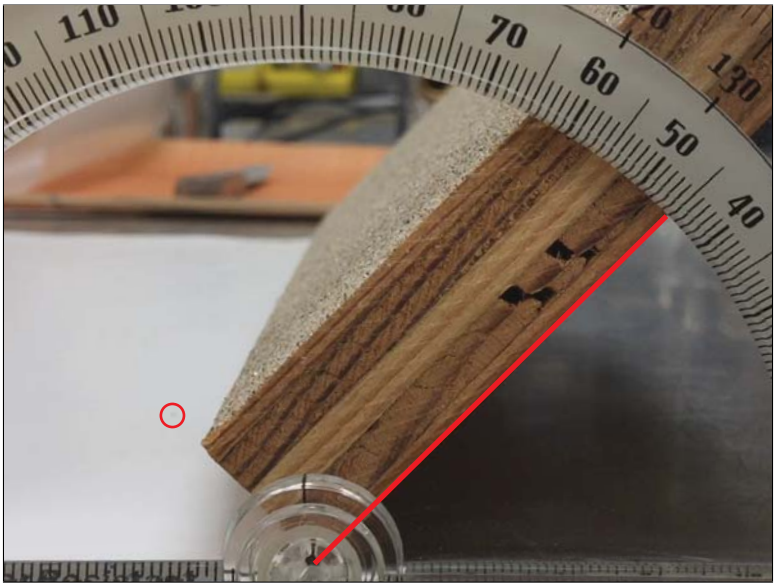

Figure 3.29: Inclined plane failure definition.

South Beach sand was dispersed over the rough board of fixed sand particles. It is assumed that the individual particles from the small scoop were dispersed evenly over a cross section of the rough board so that free particle interaction was minimal. From the video footage, the angle at which the first free particles appeared on the clean sheet of paper was observed at recorded, which defined the pocket-friction angle of the displaced particles. The average pocket-friction angle from these observations thus defines the failure of the least stable free particles on the rough sediment bed. Additional incipient motion of free particles was observed with continued inclination of the rough board, in some instances, up to angles of 90°.

The video footage, which defined the incipient motion of free particles during inclined plane testing, was supplemented with imagery from a high speed camera to observe particle movement more closely, in attempts to define the failure mechanism of

the free particles. It was assumed that the incipient motion of individual free particles starts by rolling, not sliding, which was similarly assumed in Yang et al. (2009). From the high speed camera video observations, the free particles appeared to begin motion by rolling, then bouncing quickly down the board, where particles were responding individually or combined into groups of particulate as motion down the rough board continued. Microscopic imagery was not available with the current apparatus to more closely observe the failure mechanism of free particles for the fine South Beach sand, and define incipient motion more accurately from direct observations of the rough board.

In the investigation performed in Booth et al. (2014), it was noted during inclined plane testing of gravel particulate that there is a much larger variation in the pocket-friction angle than the typical Mohr-Coulomb friction angle. The wide range in the pocket-friction angles is likely due to the inherent variability of the free particles, both in size and shape features within the complete distribution of the collection of soil particles. Additionally, variability of the rough board of fixed particles creates different voids for free particles to fall into upon dispersion, with the geometry of some voids creating a much more stable condition for the free particles than others.

While testing was being performed, temperature and humidity of the room were being monitored with a USB-502 (MeasurementComputing USB-502 RH/Temperature Data Logger). The range in average room temperature during the inclined plane testing varied from 22°C to 23°C with relative humidity ranging from 35% to 41%. No trends were observed for resulting pocket-friction angle results for the range of relative humidity measured during testing. Future researchers comparing to the results de-

termined herein may desire to ensure similar room conditions or consider this aspect as a point of possible discrepancy.

As discussed, inclined plane testing includes inherent variability. The porosity over the entire surface of the rough board of fixed sand particles varies, as well as the shape and size of each fixed and free particle. Repetitive testing was performed to obtain average values of the pocket-friction angle as well as the standard deviation. For each of the prepared rough boards with fixed sand particles, twenty inclined plane tests were performed. The average pocket-friction angle from inclined plane tests was determined to be $\phi'_{IP} = 47^\circ$ with a standard deviation of 5°. The results did not vary appreciably for the two boards prepared. The board that possessed a lighter coat of spray adhesive had an average inclined plane angle of 46°, and the second board with a thicker coat of spray adhesive produced an angle of 48°.

Chapter 4: Analysis and Discussion

The aims of Chapter 4 are to utilize the laboratory results presented in Chapter 3 for the South Beach sand investigated, in combination with knowledge gleaned from the literature synthesis provided in Chapter 2, to answer the research questions proposed in the current study. The following sections will evaluate methods, further reduce data, analyze trends, and hypothesize relationships for the index properties and loading response of South Beach sand. The results of sediment index testing will be examined with correlations employed to observe the applicability of methods and analysis techniques specifically for the subrounded, fine, poorly-graded, clean sand investigated. The response of the sand to perturbation under typical geotechnical confining pressures, and the altered response under low confining pressures, will be compared. The response of the sediment tested in standard geotechnical testing equipment will also be compared to the response of exposed sediment near the surface, simulated by angle of repose and inclined plane testing. Chapter 2 will inform the trends observed and help provide justification for the importance of the results for sediment instability applications. A database of soil properties for South Beach, Newport, Oregon sediment, and suggested laboratory methods, will be provided as outcomes of the current study. The noted outcomes will be useful for future researchers studying various engineering applications. The final responses to the proposed research questions addressed herein will be concisely summarized within Chapter 5.

4.1 Evaluation of Basic Granular Sediment Properties

4.1.1 Particle Size and Gradation Determined by Sieve Analysis

The results of sieve analyses performed herein were used to develop grain-size distribution curves for the surficial sediments sampled from South Beach, Newport, Oregon. As discussed in §3.1, sediment samples were obtained from four beach cross section locations, corresponding to approximate daily tidal levels at roughly six month time intervals. Temporal and spatial gradation trends were postulated in §3.2.1 by comparing the grain-size distribution curves for each tested specimen. The confidence in the slight trends observed are now evaluated, and the resulting implications noted.

The size and gradation of a collection of soil particles affects the response of the soil to perturbation, as discussed in §2.2.1. The development of grain-size distribution curves by sieve analyses is the standard method to determine the size and gradation of the soil particles, though there are notable shortcomings of the procedures (Hryciw et al., 2014). The sieve analysis test, a seemingly straightforward procedure, has multiple standards detailing appropriate procedures which provide guidance for determining grain-size distributions. To accurately define the gradation of a soil, ASTM D6913-04 (2009, pg. 1) states that "there are vast testing variations required due to soil types and conditions. The test is more complicated and complex than would be expected". ASTM D422-63 (2007) (withdrawn in 2016 due to lack of an updated version provided within the eight year cuttoff) states that 115 g of sandy soil be portioned from a larger sample for particle size testing. ASTM C136/C136M-14 (2014) states that standard 8 inches (20 cm) sieves shall not individually have more than 200

g of material retained to avoid overloading. ASTM D6913-04 (2009) gives more attention and specific guidance to avoid sieve overloading. In particular, ASTM D6913-04 (2009) lists the maximum mass allowed on designated sieves to avoid overloading of the sieve, with the threshold masses decreasing as sieve openings become smaller. During the sieve analyses reported herein, it is observed that even when the minimum allowable sample size for South Beach sand was utilized in sieve analyses (75 g for a maximum sample particle size of 0.425 mm), with the mechanical shaker set to a twenty minute shake time (the upper bound of the suggested shaking time range), particles were observed to pass respective sieves during subsequent hand sieving.

In a trial to investigate the phenomena of sieve overloading, sieves No. 70 and 100, which retained the majority of the specimen particles, were hand sieved extensively. In particular, sieving took place longer than suggested by ASTM D6913-04 (2009), which states that one additional minute of hand sieving be performed (this specific suggestion was adopted herein during the sieve analyses performed in §3.2.1). During hand sieving, particles were shifted in the respective sieve from side to side and jarred up and down. Of the 75 g sample portioned for the sieve analysis, 5 g of additional material passed the noted sieves after hand sieving (6.7% of the original mass). It appears that guidance from any of the prospective standards would result in the overloading of sieve and consequently, overestimate the size of particles within the fine sand samples investigated herein. The overestimation of particles sizes leads to a courser estimation of gradation. It appears to be good practice to perform additional hand sieving, following mechanical shaking of a sieve stack, to ensure that large amounts of material do not continue to pass the sieves. The improved accuracy

from employing additional hand sieving may not, however, completely eliminate sieve overloading from occurring during the sieve analysis of find sand, similar to that investigated herein.

The possibility of sieve overloading in possibly different capacities during sieve analyses may inform a lack of confidence in the slight trends noted from the comparisons between the gradations of the sediment samples investigated. The extent of hand sieving that should be performed is a somewhat qualitative and individualistic procedure, and it cannot be definitely stated that during the additional hand sieving performed herein, the effect of overloading was completely eliminated, or that the effect was decreased by the same degree for each sieve analysis. Sieve analyses were performed on different laboratory testing dates with slightly different masses of individual specimens prepared and some extent of the differences in specimen gradation could be a function of the possible variations noted. Figure 3.6 in §3.2.1 does provide some confidence that the procedures employed herein were consistent, because the triplicate sieve analyses perform on the same samples showed good agreement of the resulting grain-size distribution curves. The slight trends in beach morphology in the form of sediment bed particle size is not completely undermined by the limitations discussed, but more investigation of specific beach gradation should be performed before considering the postulated trends as influential factors in respective applications. Clearly, with the presence of possible overloading for fine sands, and likely other sediment types, it is important to choose and disclose appropriate procedures for the determination of sediment gradation.

4.1.2 Particle Shape Determined by Various Methods

As detailed in §3.2.2, several methods were performed to determine the shape characteristics of the South Beach, Newport, Oregon particulate. There is some distribution of particle shapes that result in the arithmetic mean values for roundness and sphericity reported for respective particulate samples in §3.2.2. Although the variation of particle shapes within a sediment sample contributes to the uncertainty of mean shape parameters, as noted by Santamarina and Cho (2004), the bias of particle shape classification methods also contributes to the uncertainty. Table 3.4 shows that for the same one hundred DTL particle image projections analyzed, slightly different values of roundness and sphericity were obtained. Although the reported mean values are within the 0.1 threshold discussed by Santamarina and Cho (2004), and are likely within the variability of particles within the sample, a discussion of the differences in results from the various particle shape analysis methods is provided to understand why the results vary, and determine which method is preferred for future work.

The particle shape analysis method that utilizes the measurements of circles fit to the particle projection outline features is a subjective procedure, especially for roundness estimations. When choosing how to fit circles to the surface curvature, the analyst can determine how many circles to fit to the particle surface outline, and the distinction between roundness and roughness features is sometimes difficult to determine. Additionally, observations of the visual Krumbein and Sloss (1963) roundness-sphericity chart show that as the particle shape becomes less elongated, sphericity approaches one, regardless of the roundness features of the respective par-

ticle. By this reasoning, a square-shaped projection outline should yield a sphericity value of one, because squares are not elongated in any direction. The visual classification method and a fitted ellipse estimation of a square projection (which creates a sphere), would both yield $s = 1$. However, the measured circles method would yield a substantially lower estimate. From the definition of the inscribed circle sphericity, the ratio of the largest inscribed circle to the smallest circumscribed circle of the square projection would yield the ratio of the side lengths of the square to the length of the diagonal (for a 1x1 unit square, $1{:}\sqrt{2}$), yielding $s = 0.71$. As detailed in §2.2.2, the three classes of shape parameters for the three size scales, sphericity, roundness, and roughness, should be independent of each other. The example provided of the square projection proves that for the measurement method, the sphericity estimate can be affected by roundness, because a square should be a shape of high sphericity and low roundness. Particle shape analysis of angular, spherical particles produce an underestimation of sphericity by approximately 0.3 if the method of inscribed circle sphericity is employed. This difference for some particle types provides a disagreement with the claim of Santamarina and Cho (2001) that the method used to estimate shape parameters does not vary more than 0.2.

Roundness values derived with the visual Krumbein and Sloss (1963) roundness-sphericity chart and measured circles fit to particle projection surface features are in close relation (within 0.03), as shown in Table 3.4. The agreement in roundness values provides confidence in the results for the South Beach sand, although both methods are subject to some user and technical bias.

In summary, with regards to the evaluation of particle shape analysis methods,

the method employing measurements of fitted circles to the particle projection outline to determine particle shape parameters is not justified. The respective method requires far greater user efforts than the other methods evaluated herein, and the sphericity estimates of angular spherical particles are underestimated. Particle shape analysis performed with the visual Krumbein and Sloss (1963) chart is suggested for future researchers characterizing similar sediments. The respective method is easily performed and the resulting roundness and sphericity values are determined to be accurate for analysis performed herein. It is also recommended to create fitted ellipses to the particle outline projection, because the aspect ratio of the minor and major axes provide a quick check of sphericity and the simple ellipse models may be utilized for subsequent application, as detailed for an example analysis technique in the following section.

4.1.3 Gradation Approximated by Ellipsoidal Particle Models

When fitted ellipses are created as part of a particle shape analysis, ellipsoidal models of the respective particles may be developed to obtain simplified three-dimensional, massive entities. Herein, ellipsoidal models were employed to produce an estimate of grain-size distribution to compare to the results of the sieve analyses performed herein, similarly performed by Simpson and Evans (2015). The major and minor axes dimensions of the fitted ellipses were utilized to generate prolate and oblate spheroids. Oblate spheroid were produced by rotating the ellipse around the minor axis, and prolate spheroids were produces by rotating the ellipse around the major

axis. The derived volumes of the oblate and prolate spheroids were then used in combination with specific gravity of the South Beach sand to obtain the respective ellipsoid masses.

Ellipsoid models were created for the thirty-five particles analyzed from each sample of the beach cross section from the S10 sampling effort. Figure 4.1 shows the the resulting estimation of the grain-size distribution from the ellipsoids. Various methods were utilized to produce the equivalent particle shape as determined with a sieve analysis to observe the best agreement of the grain-size distributions. As performed in Hryciw et al. (2014) and Simpson and Evans (2015), the equivalent sieve size, d_{equiv}, was determined using Equation 2.3. The major and minor axis lengths, as measures of particle size, were also employed for oblate and prolate spheroids, respectively. The grain-size distributions determined by sieve analyses are compared to those generated by the ellipsoidal models.

Figure 4.1 shows that all grain-size distributions produced from the ellipsoidal particle models estimate a finer gradation than the respective (Fredlund et al., 2000) fits developed from sieve analyses; the oblate spheroids plotted with the particle size estimated as the maximum axis length of the respective ellipses produces the closest approximation. The grain-size distributions estimated from oblate and prolate spheroids with particle sizes represented as d_{equiv} appeared to be nearly identical. The oblate spheroids are more massive than the prolate spheroids, but the proportion of masses finer than given particle sizes are based on the same size parameter, so the mass distributions plotted with respect to d_{equiv} are expected to have good agreement. Hryciw et al. (2014) and Simpson and Evans (2015) show that, theoretically, d_{equiv} is

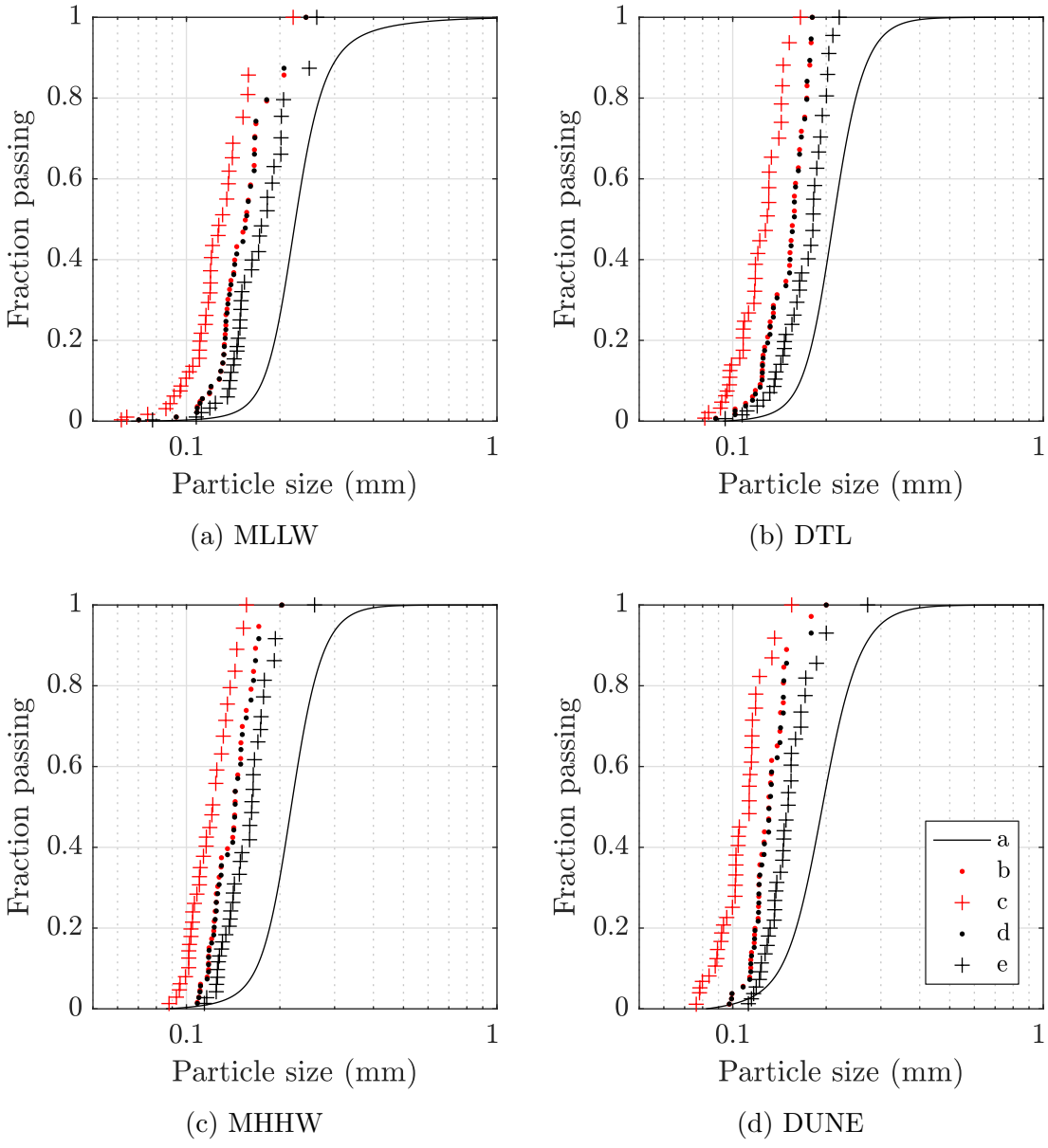

(a) MLLW (b) DTL

(c) MHHW (d) DUNE

Figure 4.1: Comparison of grain-size distributions produced by sieve analyses and ellipsoidal particle models for samples from the S10 sampling effort. For each subplot, curve a. depicts the Fredlund et al. (2000) fit of the sieve analysis, curves b. and d. show the prolate and oblate spheroids generated with d_{equiv} used as the equivalent sieve size, respectively, and curves c. and e. show the prolate and oblate spheroids with the minimum and maximum axes lengths as the estimated particle size, respectively.

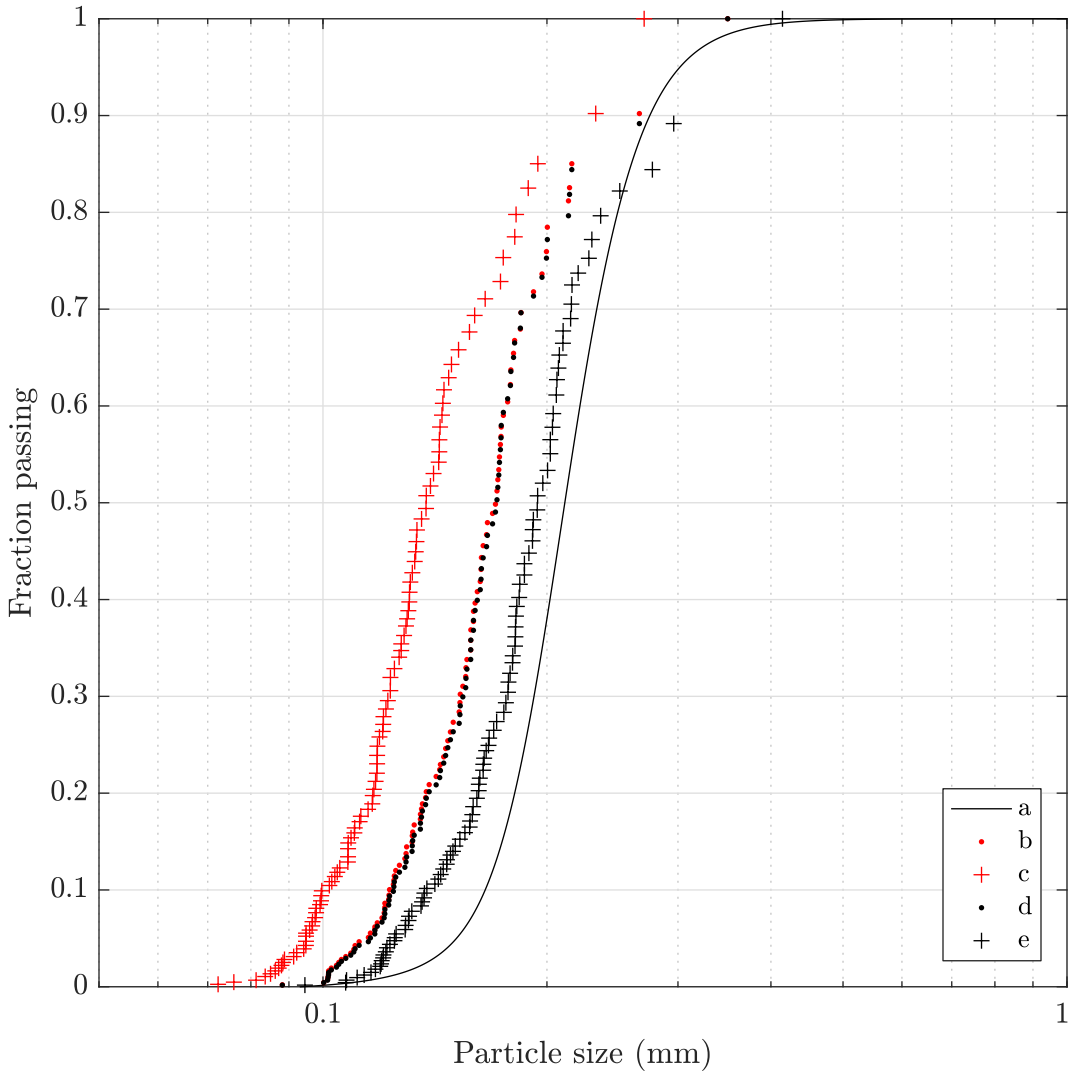

Figure 4.2: Comparison of grain-size distributions produced by sieve analyses and ellipsoidal particle models for one hundred particles from the DTL samples from the S10 sampling effort. Curve a. depicts the Fredlund et al. (2000) fit of the sieve analysis, curves b. and d. show the prolate and oblate spheroids generated with d_{equiv} used as the equivalent sieve size, respectively, and curves c. and e. show the prolate and oblate spheroids with the minimum and maximum axes lengths as the estimated particle size, respectively.

the square sieve opening size that a respective ellipse could pass, due to the geometry of the scenario. Therefore, ellipsoids employing d_{equiv} as the equivalent particle size are expected to match the Fredlund et al. (2000) curves fit to sieve analysis data best.

Upon observation of Figure 4.1, it appeared that during microscopic imaging of the sediment particles, the largest particles of the distribution were not being captured. The largest particles would be the most massive, so it was predicted that if the extent of the grain-size distribution of the samples was better represented by the particle images captured, including the largest particles present, the fit of the grain-size distributions generated from ellipsoid models would have better agreement with the Fredlund et al. (2000) curve fits of the sieve analysis data. Figure 4.2 shows that when the ellipses produced from the one hundred DTL particles analyzed in the particle shape analysis are modeled as ellipsoids, the estimation of the grain-size distribution curve produced from the sieve analysis improves. The comparison of the DTL sample shows that the difference in d_{50} reduces from 0.05 to 0.04 mm between the ellipsoidal approximation with particle sizes represented as d_{equiv} and the Fredlund et al. (2000) fit as the sample size increases from thirty-five to one hundred.

As noted by Hryciw et al. (2014), any method used to approximate the grain-size distribution of a collection of soil must agree with the results of sieve analyses to be viable. The comparison to other data sets, where sieve analyses were used, justifies that the results of shape characterization methods must produce agreeable results to be comparable. The trends noted between the ellipsoidal estimations of the grain-size distributions and those produced by sieve analyses are different than those found in Simpson and Evans (2015), which employed very similar methods

to those employed herein. The sand investigated in the Simpson and Evans (2015) study was a manufactured sand, Ottawa 50/70, which is rounded to well-rounded silica sand (d_{50} = 0.264 mm) constituted of particle sizes retained on No. 50 and No. 70 sieves. The results of Simpson and Evans (2015) show very good agreement for oblate spheroids with particle sizes represented as d_{equiv} used to generate the grain-size distribution determined by sieve analysis. Twenty-four fitted ellipses of particle projection images were used in the respective study to generate the oblate spheroid models for the distribution.

Estimation of grain-size distribution generated by ellipsoidal particle models for the fine, natural South Beach sand investigated herein may not be appropriate. Based on observations, the subrounded sand is not as well represented by the ellipsoidal particle models, and the resulting grain-size distributions underestimate those produced by sieve analyses. The natural South Beach sand also has different particle densities for different sized particles throughout the distribution, as predicted by observations of the sieve analyses where metallic particles were observed to pass the No. 140 sieve. The difference in specific gravity values of individual particles skews the resulting grain-size distributions. The limitation of performing sieve analyses on the respective fine sand is also considered, and the possible sieve overloading discussed in §4.1.1 likely contributes to the differences between the grain-size distributions produced by ellipsoidal particle models and sieve analyses.

Table 4.1: Packing density comparisons. The range of packing densities, as defined by limiting void ratios, e_{min} and e_{max}, are reported from laboratory testing measurements in comparison with estimates determined with Equation 2.4 via visual and measured roundness values, $r = 0.36$ and $r = 0.39$, respectively.

Parameter	Laboratory	Via $r = 0.36$	Via $r = 0.39$
e_{min}	0.67	0.59	0.57
e_{max}	0.90	0.98	0.95

4.1.4 Limiting Packing Densities Determined by Various Methods

Equation 2.4 was employed to estimate the limiting void ratios from particle shape. More specifically, roundness values determined in §3.2.2 are used to calculate the predicted minimum and maximum void ratios and are compared to values measured in the laboratory with guidance from ASTM D4253-16 (2016) and ASTM D4254-16 (2016), as detailed in §3.2.4. Table 4.1 shows the measured and estimated values for e_{min} and e_{max}. The measured and estimated packing densities are reported for DTL samples. The image analysis performed on one hundred DTL particles produced the roundness values reported in Table 3.4, by visual classification with the Krumbein and Sloss (1963) roundness-sphericity chart ($r = 0.36$), and by measurements of fitted circles to the particle projection outlines ($r = 0.39$).

Estimates of e_{min} and e_{max} derived from Equation 2.4 assume that $C_u = 1$, rather than the actual reported value of $C_u = 1.35$ for the respective DTL sample. The estimates also do not account for the unique specific gravity of various sediments, which would affect the resulting void ratios. Table 4.1 shows that the limiting void ratios predicted from the roundness values are within 0.1 of those determined in the laboratory.

The range of limiting void ratios is larger for the estimations produced from particle roundness than those measured in the laboratory. As discussed in §3.2.4, the minimum void ratio was not determined strictly in accordance with ASTM D4253-16 (2016). A vibratory table was not employed, nor the application of a confining pressure to the surface of the specimen mold. The deviation from standard procedure to determine e_{min} is predicted to produce a higher value. Comparisons made in §3.2.4 with the work of Holubec and D'Appolonia (1973) help to confirm this prediction, as tests were performed on similar sediment to South Beach sand, and produced similar ranges of e_{min} and e_{max}. Holubec and D'Appolonia (1973) shows a decrease in e_{min} of about 0.1 when procedures similar to ASTM D4253-16 (2016) are employed. The value of $e_{min} = 0.59$ determined with Equation 2.4 is near the expected value of the minimum void ratio determined if the procedures provided by ASTM D4253-16 (2016) had been followed directly. It is also plausible that there is some uncertainty in the maximum void ratio measurements performed in the laboratory, and thus a higher value of $e_{max} = 0.98$ is reasonable [also a higher value, but comparable to $e_{max} = 0.88$ determined by Holubec and D'Appolonia (1973)]. It is concluded herein that the limiting void ratios resulting from particle roundness values determined via Equation 2.4 provide a good approximation for South Beach sand. Notably, small changes in the range between e_{min} and e_max produce noticeable changes for the estimated relative density of a sand specimen, which is important for the laboratory strength testing presented herein.

4.1.5 Friction Angle Approximated by Particle Shape

As discussed in §2.2.2, Equation 2.5 aims to estimate the critical state friction angle as a function of roundness. The estimated friction angle, from Equation 2.5, of the DTL sediment obtained during the S10 sampling effort, is between $\phi' = 35$ and $36°$, depending on the r value utilized (i.e., $r = 0.36$ from visual classification or $r = 0.39$ from the measured roundness features, as discussed in §3.2.2). Equation 2.5 was developed to correlate with the critical state friction angle as measured by the angle of repose, by the method of tilting sediment in a graduated cylinder (Santamarina and Cho, 2004). As discussed in §2.3, the angle of repose has been found to be several degrees higher than the critical state friction angle at typical geotechnical confining pressures (Sadrekarimi and Olson, 2011).

Herein, the method of approximating the angle of repose with South Beach sand in a graduated cylinder did not yield very reasonable results for the wet method, or repeatable results for the dry method, as discussed in §3.3.3. However, the average angle of repose with the respective method did produce a value of $\phi'_{Rep} = 36°$. The result of Equation 2.5 yields a lower value than the angle of repose via ASTM C1444-00 (2000) determined herein, $\phi'_{Rep} = 38°$, and slightly higher than the critical state friction angle determined with triaxial testing, $\phi'_{cs} = 34°$. The use of Equation 2.5 to estimate the critical state friction angle for South Beach sand is thought to provide a reasonable estimate of the critical state friction angle.

4.2 Comparison and Explanation of Strength Properties

As detailed in Chapter 3, triaxial and simple shear tests were employed to determine the friction angle of the South Beach, Newport, Oregon sand at various confining pressures. Tests with similar confining pressures applied to specimens were performed to obtain comparable results between the two testing apparatuses. As discussed throughout, the current study has a vested interest in the near-surface response of the South Beach sand investigated. However, it is important to define the response of the sediment to perturbation under typical confining pressures to establish baseline results. The friction angles determined via triaxial and simple shear test results exhibit good agreement for tests performed with typical confining pressures. As discussed in §2.3, plane strain conditions are expected to yield slightly higher friction angles than triaxial conditions for tests performed on the same material, because the intermediate principal stress influences the plane strain response. Shearing in triaxial tests was ceased at 15% axial strain, as suggested by ASTM D7181-11 (2011). The specimens were assumed to be near critical state at the termination of the triaxial tests. Although the volumetric response had not yet plateaued at 15% axial strain, the deviatoric stress appeared to reach a constant value. It is assumed that the friction angle determined with triaxial testing is accurate within about 1°, as noted by Bolton (1986) on the confidence of geotechnical strength tests. The estimation at 15% axial strain would generally be the critical state friction angle reported, because higher strains with triaxial tests are not typically employed (ASTM D7181-11, 2011; Sadrekarimi and Olson, 2011).

Although higher friction angles are expected for plane strain conditions, which the simple shear device aims to replicate, the constant volume friction angles estimated at typical confining pressures (σ'_v = 200 to 300 kPa), were very near the critical state friction angle estimated from the triaxial test results. It should be noted that the constant volume friction angles estimated from simple shear test results were obtained at high shear strains, when specimen volume change had plateaued. Had the tests been terminated at shear strains of $\gamma = 15$ or 20%, more typical of geotechnical shearing tests, the angles would have generally been several degrees higher. Figure 3.23 shows this effect in the difference between peak and constant volume friction angles, because the peak conditions under these confining pressures were near $\gamma = 20\%$. Equation 2.19 may also provide an underestimation of the friction angle, especially at small shear strains, but as shown by Wijewickreme et al. (2013), the approximation is likely appropriate at large strains. The interpretation of the results of the triaxial and simple shear tests show that for the South Beach, Newport, Oregon sand (DTL sediment from the S10 sampling effort), the critical state friction angle for typical geotechnical confining pressures is $\phi'_{cs} = 34°$.

Because the relative density of the simple shear test specimens was greater than the relative density of the triaxial test specimens (i.e., 40% versus 20%), the soil stiffness during shearing in the simple shear device is expected to be greater. However, the shearing mechanisms of the testing apparatuses are different and elastic moduli estimated from the responses can not be directly compared. The elastic relationship given in Equation 2.14 relates ν, E, and G, which allows the stiffness of the testing specimens used in the triaxial and simple shear devices to be compared. Equation

2.14 is based on Hooke's law, which defines isotropic linearly-elastic stress-strain relationships (Bardet, 1997). Although soil does not truly conform to the assumptions of Hooke's law, the initial shearing response of soil is typically assumed to simulate elastic conditions, but the uncertainties due to these simplifications should be recognized.

Poisson's ratio was estimated as the mean value determined from the triaxial test responses, $\nu = 0.30$. As discussed, specimens in the triaxial device were tested at $D_r \approx 20\%$. The slightly greater relative density of specimens used in simple shear testing ($D_r \approx 40\%$) may have resulted in a higher Poisson's ratio (i.e., $\nu \approx 0.35$). However, there is no direct way to measure Poisson's ratio in simple shear testing, which is defined as $\nu = -d\varepsilon_y/d\varepsilon_x$, or the ratio of the measure of compression of one axis, to the expansion of the perpendicular axes. Poisson's ratio is not defined with respect to the volumetric strains experienced when a material undergoes shear strains, i.e., simple shear deformations. Herein, the use of Equation 2.14 does not provide good agreement between E and G values determined from triaxial and simple shear test results, respectively (provided in Tables 3.6 and 3.7), even when a range of ν is investigated. The responses measured in the simple shear apparatus appear to underestimate the soil stiffness, which estimates modulus of elasticity values that are uncommonly low for the sediment investigated. Similar magnitudes of shear moduli are determined by Kraupa (2013), in which the same simple shear testing device is used for evaluating ecoroof material. Typical values of the modulus of elasticity for loose to dense sands are between 10 to 100 MPa, as discussed in §2.3. The low estimates of the elastic modulus for the South Beach sand tested in the simple shear

device are perhaps due to the moduli being calculated from the specimen boundary strains, which Holtz et al. (2011) states may result in underestimations of soil stiffness.

Only typical confining pressures that were applied to specimens for triaxial and simple shear tests are compared for the following moduli correlations (50 to 200 kPa). The modulus of elasticity values, calculated via Equation 2.14 with shear modulus values from simple shear test responses, range from $E \approx 1$ to 8 MPa (in contrast to those measured from triaxial test responses: $E \approx 20$ to 70 MPa), generally increasing with confining pressure. Similarly, the shear modulus values, predicted using modulus of elasticity values estimated from triaxial test responses, range from $G \approx 7$ to 27 MPa (in contrast to those measured from simple shear test responses: $G \approx 0.5$ to 3 MPa), also increasing with confining pressure. There appears to be a disconnect by an order of magnitude between the approximations when using the relationship proposed in Equation 2.14.

Differences in consolidation methods may also contribute to the difference in soil stiffness estimated from triaxial and simple shear testing. Isotropic consolidation in triaxial testing applies equal pressure to the entire surface area of the testing specimen, while uniaxial consolidation in simple shear tests applies lower lateral stresses (near at-rest conditions, or $\sigma'_h = \sigma'_v \times K_0$) than the vertical effective stress. For this reason, the lateral stresses present within simple shear specimens are likely less than those in triaxial specimens, when similar values of σ'_3 and σ'_v are applied during consolidation. For both triaxial compression and simple shear test results, the stiffness of the tested material depends on the level of confinement. Triaxial tests that employ K_0 conditions during the consolidation phase may more closely match the state of simple shear

specimens.

Following the simple shear tests performed on specimens under typical confining pressures, tests were performed on specimens for a range of lower confining pressures, down the lowest pressure that the system could apply, as detailed in §3.3.2. Researchers have found that accounting for the contribution of system resistance and correcting measured loading responses for these unintended loads is important for tests performed under low confining pressures (e.g., Ponce and Bell, 1971; Fukushima and Tatsuoka, 1984), as discussed in §2.3. To account for the added resistance of components of the simple shear testing apparatus, and to understand the resulting influence on the measured loading responses of the specimens to perturbation, several methods were evaluated. A final correction to the simple shear test results is applied herein in order to present the outcomes of all strength tests as a summary plot. It is noted that more complex corrections may be necessary to fully understand the simple shear test results at extremely low confining pressures. Future work should be performed to further investigate the complexities of the measured responses of specimens sheared under low confining pressures in the simple shear device.

Initially, tests were performed to quantify a friction angle to encompass the resistance that system components contributed to the measured loading responses. Small loads (10 and 15 N) were applied to the surface of the Teflon confining ring stack with no specimen present, and the shearing phase was performed as usual. Figure 4.3 shows the process of this method of system resistance testing. An average stress pair ($\bar{\sigma_v'}$, $\bar{\tau'}$) was determined from each test response. The stress pairs were then used to estimate a friction angle, similar to how the friction angle for specimens tested in

simple shear was determined, via Equation 2.19. With this method, a friction angle of the simple shear system resistance was determined to be approximately 20°. It is evident that a reduction of the friction angles estimated from the simple shear test responses by 20° would be an inappropriate correction, and would not address the specific corrections necessary for results at very low confining pressures. The friction angle estimated from the measured resistance of the system may need to be used in combination with the appropriate normal stresses present at the respective component interfaces in order to improve the accuracy of corrections with this method. The vertical effective stress applied to the top surface of simple shear testing specimens, σ'_v, is transmitted through the specimen and transferred laterally at the membrane interface, in some capacity, to the confining rings during consolidation and shearing phases. Without further instrumentation, it is difficult to quantify the loads experienced by the confining rings and other system components. Following this approach, other methods to determine the contribution of system resistance to the measured loading responses were evaluated.

An alternative approach to determine appropriate corrections for the simple shear results was investigated by directly measuring the frictional resistance of the vacant system. The specimen base plate, confining rings, and a mass equal to that of a soil specimen ($\approx$ 110 g) were placed into position in the simple shear device and the shearing phase was performed as usual. The purpose of the horizontal actuator advancing the apparatus without an applied vertical load was to observe the horizontal loads recorded when the measurements were expected to be zero. This approach accounts for only for the components that do not directly apply load to the top surface

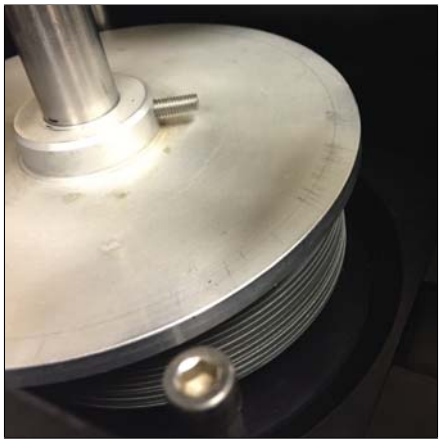

(a) Confining rings in position pre-shear

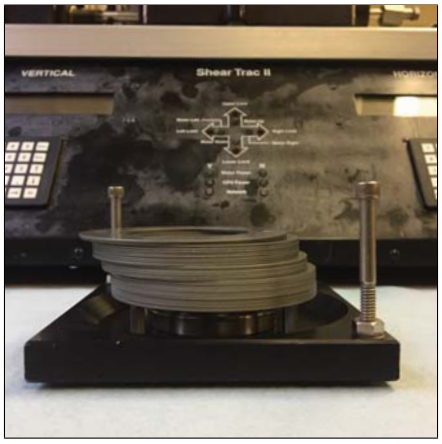

(b) Confining rings post-shear

Figure 4.3: Simple shear system resistance testing by applying loads to the Teflon confining ring stack. The rings are loaded by locking the LVDT plate to the loading rod and placing the plate on the confining ring stack (a), and shearing is applied as usual to measure the shear resistance of the system without a specimen in place (b).

of the testing specimen when in place (i.e., the specimen cap, LVDT plate, loading rod, and any addition vertical load applied by the system). Figure 4.4a shows the process of this system resistance test (E1). Figure 4.5 shows the measured horizontal loads for the E1 test. The measured horizontal loads during horizontal displacement were small (average value of ≈ 2 N). The respective measurements appear to produce reasonable horizontal loads that were contributed to the results from the system resistance of the simple shear device. This correction method does not account for membrane effects, and an alternate method to perform a similar 'empty' test to measure the horizontal load during displacement with a membrane in place was also performed.

Creating an 'empty' system, wherein the testing apparatus is in place as if a soil specimen is present, is difficult. The top specimen cap falls into the void created by the confining rings without a specimen present. To address this issue, an O-ring was

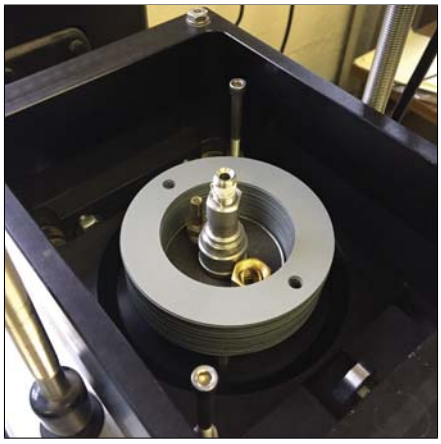

(a) E1

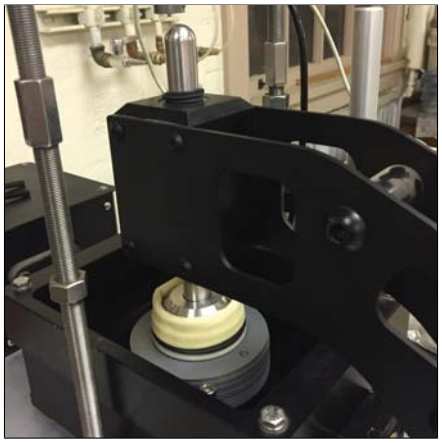

(b) E2

Figure 4.4: Simple shear system resistance tests with no vertical loads applied.

secured around the specimen cap to secure its placement atop the confining rings. The membrane was then positioned as if a soil specimen was present. The empty specimen apparatus was placed in the simple shear device and the loading rod was screwed into the specimen cap to secure the position. The purpose of this test was primarily to observe the added contribution of the specimen membrane to the system resistance, and thus, the additional uncertainty of applying load to the confining rings was undesirable. To ensure that no vertical loads were being transmitted to the confining rings from the specimen cap, the loading rod was raised slightly from the at-rest position and secured in place with an elastic band so that the O-ring around the specimen cap hovered slightly above the surface of the confining rings. The shearing phase was then performed as usual and the horizontal resistance was measured. Figure 4.4b shows the process of this system resistance test (E2). Figure 4.5 shows the horizontal loads measured for the E2 test. The horizontal loads recorded

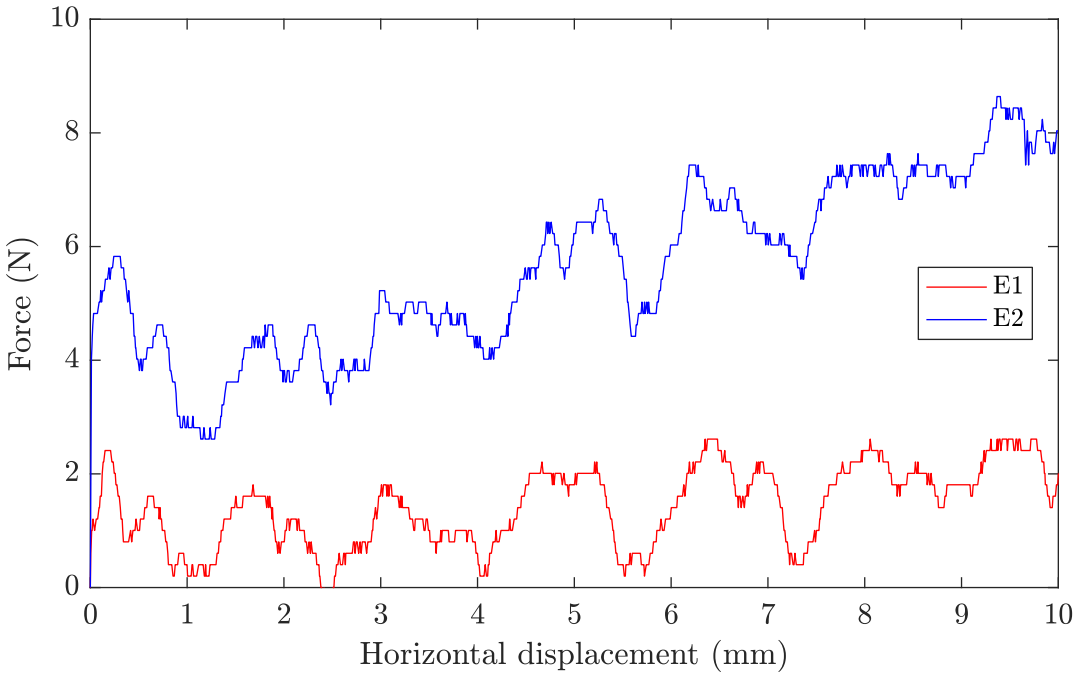

Figure 4.5: System resistance measurements of the simple shear apparatus.

are greater than the response shown for test E1, which is expected due to the added resistance of the membrane. It should be noted that the resistance measured from the membrane is likely different than the true added membrane resistance when a soil specimen is present in the apparatus, because the displacement mechanisms would be altered.

Following the observations of the resistance contributed by the simple shear testing system components, initial corrections are applied to the simple shear test responses. Figure 4.6 shows two examples of the resulting friction angles when corrections are applied to the measured shearing responses. Figures 4.6a and 4.6b show the corrected friction angles for peak and constant volume states when 5 and 10 N are deducted

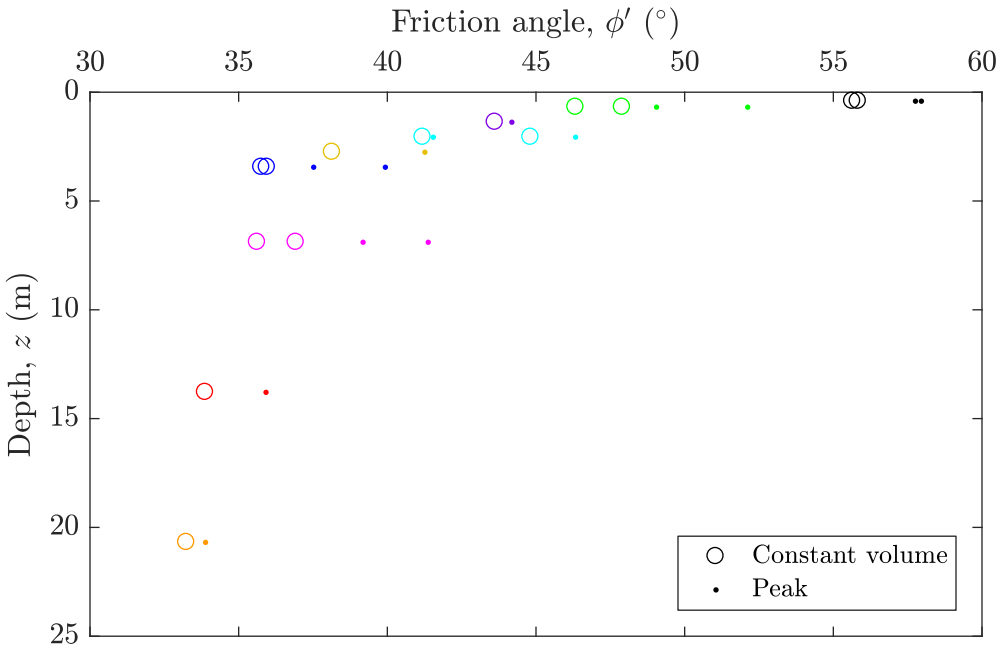

(a) 5 N deducted from simple shear data

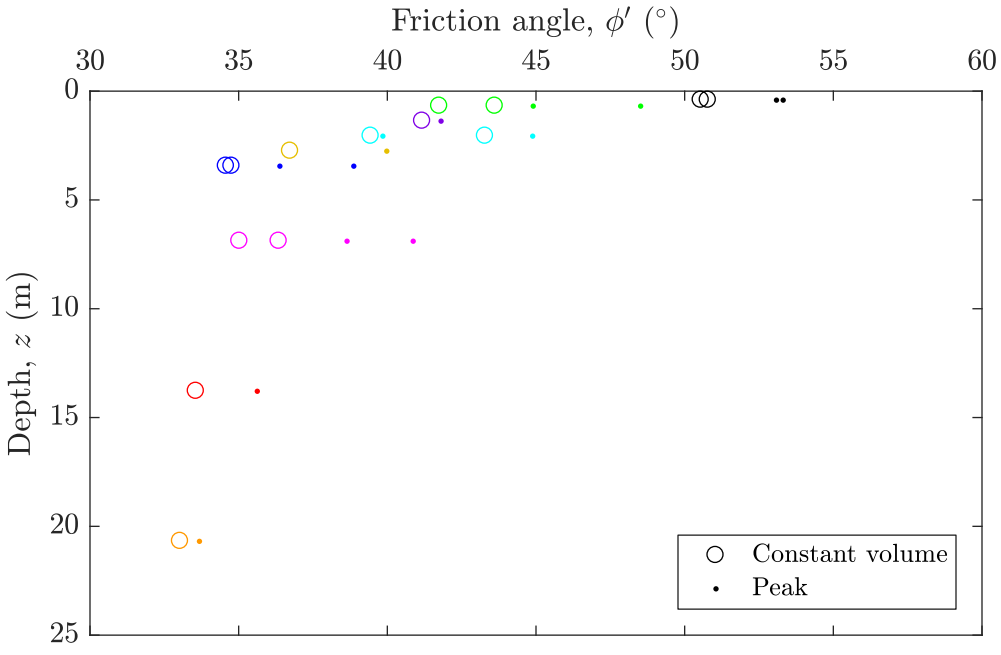

(b) 10 N deducted from simple shear data

Figure 4.6: Examples of corrected simple shear results.

from the measured shearing responses, similar to the methods employed by Kwan and El Mohtar (2014) for cyclic simple shear test corrections. Figure 4.6a shows that the lowest confinement test, simulating the shallowest depth (σ'_v = 6 kPa), is altered when a reduction of 5 N is applied to the measured shearing resistance data, by a decrease in friction angles of approximately 5°. Deducting a constant value from the shearing response data produces greater effects on tests performed under lower confining pressures, because the magnitude of the measured shearing resistance loads are lower. At a certain magnitude of a constant force applied as a correction to the shearing responses, the friction angles appear to shift too greatly. Although the trends are somewhat confused in the uncorrected results, due to the challenges of low confinement testing using the simple shear device, generally, the friction angles increase with decreasing confining pressures (i.e., depth). Notably, in Figure 4.6b, the friction angles of several low confinement tests are shifted to be less than friction angles of higher confinement tests. This effect implies that 10 N deducted from the shearing response data approaches the upper bound of an appropriate correction by this method.

Although the system resistance testing herein did not definitively determine the appropriate corrections that should be applied to low confinement simple shear test results, the various methods performed for the initial evaluation are useful for understanding the resistance of the simple shear system components. At the current stage, it appears most appropriate to apply a correction of a constant force value to the measured shearing responses.

As discussed in §2.3, Bolton (1986) and Chakraborty and Salgado (2010) present

empirical expressions to predict sediment dilation during shearing and the resulting peak friction angle as a function of the specimen relative density and applied confining pressure. The fitting parameters, R and Q, employed in Equations 2.11 and 2.12 by Bolton (1986) and Chakraborty and Salgado (2010), respectively, represent similar aspects of the friction angle predictions, and thus, values of R and Q are interchangeable between the noted expressions. Bolton (1986) concludes that values of $Q = 10$ and $R = 1$ are generally appropriate to estimate the peak friction angles of the respective sands investigated under typical confining pressures. For plane strain conditions, Chakraborty and Salgado (2010) shows that Q approaches 8 (when maintaining a value of $R = 1$ for simplicity), especially for low confinement shearing responses of sand. To evaluate the predictions of peak friction angle for a range of confining pressures, the sensitivity of Equations 2.11 and 2.12 is investigated. Although herein the critical state friction angle is found to increase with a decrease in confining pressure (noticeable at pressures below around $\sigma'_v = 50$ kPa for the simple shear test responses), a constant value of $\phi'_{cs} = 34°$, which was reported for typical confinement conditions as a result of triaxial and simple shear testing, is utilized for the investigation of the sensitivity of Equations 2.11 and 2.12. The constant value of critical state friction angle is employed for simplicity and to provide application conditions consistent with how the noted expressions were derived.

As noted in §2.3, Equation 2.12 by Chakraborty and Salgado (2010) is developed to extend the expression developed by Bolton (1986) to estimate peak friction angles for sand sheared under low confining pressures ($p' < 100$ kPa). Appropriately, in the following evaluation, Equation 2.12 is utilized to estimate the peak friction angle

when $p' \leq 100$ kPa, and Equation 2.11 for $p' > 100$ kPa (for plane strain conditions where $\phi'_p - \phi'_{cs} = \phi'_{cs} + 5I_R$, as discussed in §2.3). Similar to the range of possible Q values from 8 to 10 determined by Chakraborty and Salgado (2010), there is some uncertainty in the relative density of South Beach sand specimens tested in the simple shear device. The influence of the noted uncertainties for the estimations of peak friction angles is shown graphically by plotting the predictions produced by Equations 2.11 and 2.12 with the lower bound of the density range, $D_r = 30\%$, and the fitting coefficient of $Q = 8$, which produces the lower bound peak friction angle estimations, and similarly $D_r = 50\%$ and $Q = 10$ for the upper bound peak friction angle estimations. The expected peak friction angle estimations from the simple shear testing results are determined with the target relative density of the simple shear test specimens, $D_r = 40\%$, and $Q = 8$ for plane strain conditions, which the simple shear apparatus aims to replicate. Figure 4.7 shows the resulting bounding and expected peak friction angle prediction curves from Equations 2.11 and 2.12 in linear and semi-logarithmic space.

Figure 4.7 shows the range of expected peak friction angles resulting from the typical to low confinement simple shear testing, if the South Beach sand investigated with the simple shear device conforms to the trends that Equations 2.11 and 2.12 predict. It is important to note that Equation 2.12 was developed exclusively from the database of low confinement test responses of Toyoura sand reported in Fukushima and Tatsuoka (1984) and Tatsuoka et al. (1986). The limitation of the applicability of Equation 2.12 to predict the response of other sands is evident, because the responses from different low confinement tests on sands show varying trends (e.g.,

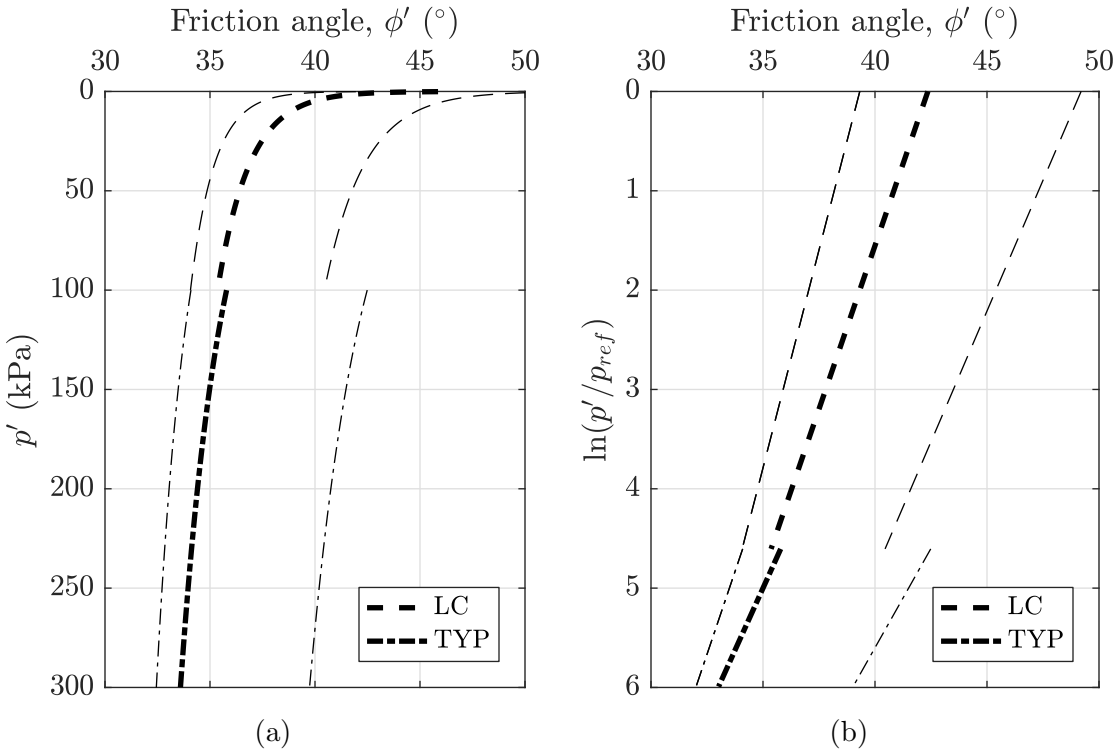

Figure 4.7: Range of predicted peak friction angles. 'LC' curves correspond to the low confinement estimation by Chakraborty and Salgado (2010) and 'TYP' curves correspond to typical confinement estimation by Bolton (1986). The lower bounding thin lines employ fitting parameters, $R = 1$, $Q = 8$, $D_r = 30\%$ and for the upper bounding thin lines, $R = 1$, $Q = 10$, $D_r = 50\%$. The thin bounding lines show the expected reasonable range of the predicted friction angle from Equations §2.11 and §2.12. The thick lines show the expected prediction of peak friction angle which employs fitting parameters $R = 1$, $Q = 8$, $D_r = 40\%$.

Ponce and Bell, 1971; Stroud, 1971; Fukushima and Tatsuoka, 1984). Neither of the relationships defined in Equations 2.11 and 2.12 consider specific sediment particle properties. As discussed in §2.2, index properties such as particle size, gradation, and shape influence the sediment loading response, in addition to the relative density and level of confinement. Results from Equations 2.11 and 2.12 are used herein as an example of the predicted response to perturbation of sand, in typical to low confinement conditions, from previously developed relationships. The range of mean effective stresses for which Equation 2.12 is developed is extrapolated in Figure 4.7, down to $p' = 0.1$ kPa, below the lowest confining pressures applied to the Toyoura sand in the respective database (≈ 2 kPa). The semi-logarithmic plot in Figure 4.7b shows the peak friction angle predictions for pressures down to $p' = 1$ kPa. Lower values of p' produce negative values on the y-axis, but if extrapolated, the trend produces a continuous estimate for smaller positive mean effective stress values.

To obtain the Chakraborty and Salgado (2010) and Bolton (1986) peak friction angle estimates as a function of depth, which allows comparisons to the simple shear test results provided herein, a simplified approach is presented. Plane strain conditions are assumed for the predicted peak friction angles, and for plane strain conditions, the peak principal stress relationship is estimated as (Chakraborty and Salgado, 2010),

$$b = \frac{\sigma'_2 - \sigma'_3}{\sigma'_1 - \sigma'_3}, \tag{4.1}$$

where $b \approx 0.25$ (Mitchell and Soga, 2005). The relationship provided by Equation 4.1, along with the assumption of at-rest conditions (i.e., $\sigma'_3 = \sigma'_1 \times K_0$, where

$K_0 = 1 - \sin\phi'_{cs}$ (Holtz et al., 2011) and $\phi'_{cs} = 34°$), allows for the estimation of the equivalent vertical effective stress (σ'_v). Note that the equivalent vertical effective stress is assumed to be equivalent to the major principal stress (σ'_1) for the preceding estimation, which is reasonable for the consolidation mechanism in plane strain tests. These simplifying assumptions produce σ'_v estimates, which simulate the overburden pressure of a soil specimen at a given depth below the surface of a sediment bed. The estimates of σ'_v are then related to corresponding sediment embedment depths, with the same method employed for simple shear test results in §3.3.2, by assuming an average dry unit weight of γ_d =14.5 kN/m^3. Although there are many complexities simplified in the preceding assumptions (e.g., rotation of principal stresses for sediment loading responses in plane strain conditions, deviation from at-rest conditions at peak state, range of critical state friction angles as conditions deviate from typical geotechnical confining pressures), the resulting peak friction angle estimations with depth from Equations 2.11 and 2.12 allow generalized comparisons to the simple shear test responses of the South Beach sand specimens. The respective comparisons provide further justification that the simple shear test responses provide reasonable low confinement trends.

To provide a summary of the interpretation of sediment strength parameters (i.e., friction angles) with depth, Figure 4.8 shows the reduced test results from the various loading responses of South Beach sand. For the final presentation of the summary of friction angles, simple shear test responses are corrected by deducting 8 N from the measured loading responses. The constant correction value was selected based on the results of the correction trials shown in Figure 4.6, and the upper bound of

the observed measurements of the system resistance tests shown in Figure 4.4, which provided reasonable adjustments to the responses. Figure 4.8 also shows schematically the proposed relationships between the various characteristic friction angles determined herein. It should be noted that the imposed trend lines in Figure 4.8 serve only as predictions of how the friction angles may change with depth below the surface of a simplified sediment bed, based on the interpretation of the laboratory results and informed by the literature. Further analytical efforts and experimental data would improve the accuracy of the proposed trends. The predicted peak friction angles with depth (dashed lines) are projected on Figure 4.8 from the Chakraborty and Salgado (2010) and Bolton (1986) estimations described (via Equations 2.11 and 2.12), with the prediction curves utilizing the expected appropriate inputs for the simple shear testing performed herein: $D_r = 40\%$, $Q = 8$, and $R = 1$. The predicted critical state friction angle with depth (solid line) has been projected on Figure 4.8 with a simplified trend presented. The increase of the critical state friction angle for sediment under low confinement is informed only by the interpretation of the simple shear test responses, and by the prediction noted in Sadrekarimi and Olson (2011) that the critical state friction angle approaches the angle of repose for sediment under low confining pressures; therefore, more sophisticated trends to define the change in critical state friction angle cannot be predicted at the current stage. Figure 4.8 also shows the angle of repose and the pocket-friction angle determined in §3.3.3 and §3.3.4, respectively, as ϕ'_{Rep} and ϕ'_{IP}, simulated as properties at the surface of the sediment bed.

The constant volume friction angles determined from the simple shear test results,

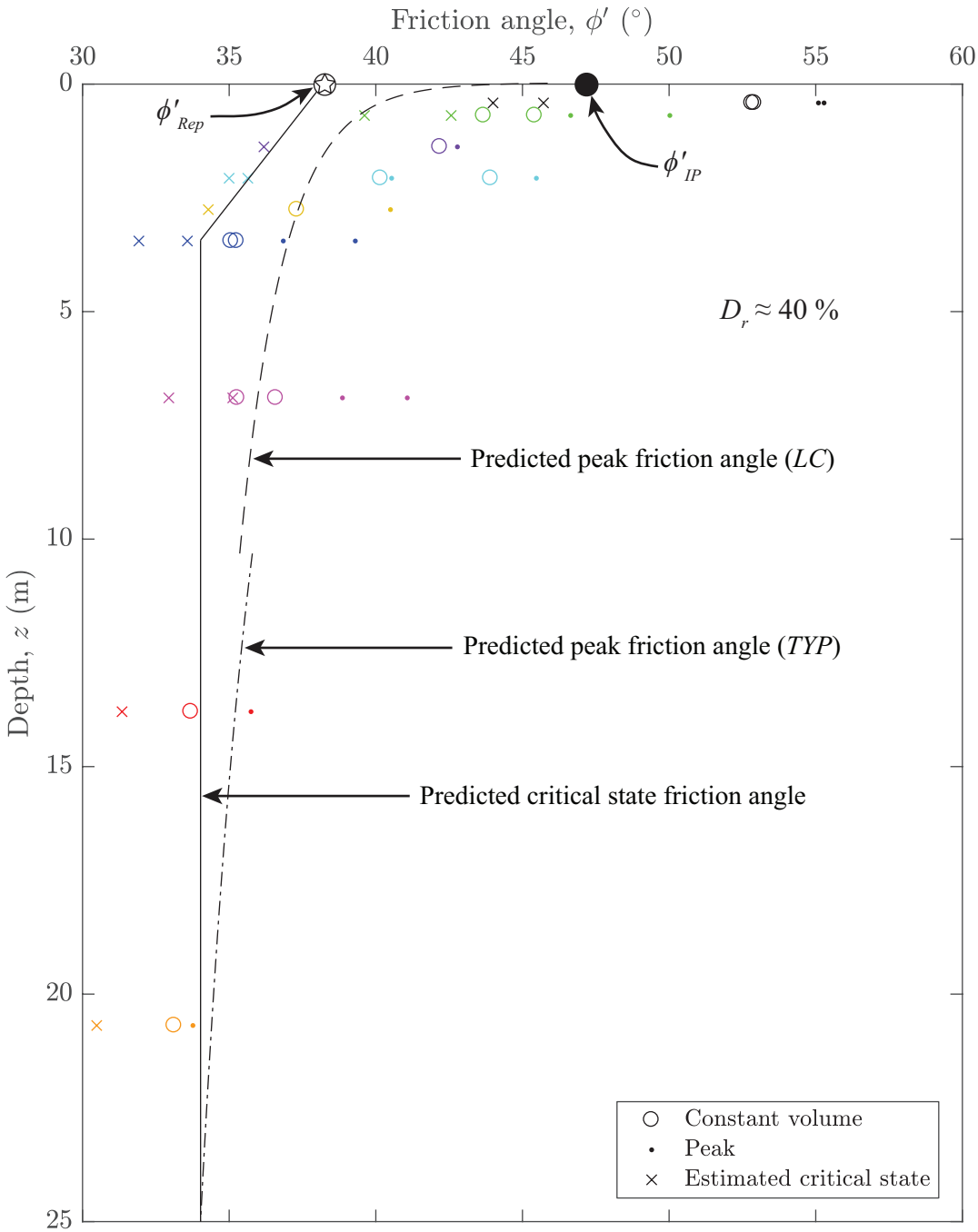

Figure 4.8: Summary of South Beach sand characteristic friction angles. The solid line shows the simplified trend for the increase in critical state friction angle with decreasing depth. The dashed lines, produced by Equations §2.11 and §2.12, show the predicted peak friction angles. Constant volume, peak, and estimated critical state points are produced from the reduced simple shear test responses.

as discussed in §3.3.2, are based off of the friction angles estimated when the loading responses produced negligible volumetric changes. As shown in §3.3.2, accounting for the dilation angle, estimated from the maximum slope of the volumetric response, produces a different estimation of the critical state friction angle. The critical state friction angles estimated from the noted dilation angles appear to approach the angle of repose under very low confinement (i.e., near the surface), as postulated by Sadrekarimi and Olson (2011).

It is observed from the corrected simple shear results summarized in Figure 4.8, that the increase of the estimated critical state friction angle is noticeable at depths less than about 3 m from the surface of the simplified medium density, dry sediment bed (i.e., simple shear tests responses with $\sigma'_v = 50$ kPa show the initiation of the observed increase from $\phi'_{cs} = 34°$), and appears to approach a value near the angle of repose. The very low confinement tests performed herein (i.e., $\sigma'_v = 6$ and 10 kPa) deviate from this trend, possibly as a result of the inability of the simple shear testing equipment to reliably measure the loading response at the extremely low confining pressures, or the responses may not be sufficiently corrected for system resistance effects. The very low confinement test results are most susceptible to the effects of unintended forces during testing, because small contributions of measured loads constitute a larger proportion of the small shearing response loads measured.

The critical state friction angles estimated by deducing dilation angles, determined from the maximum slopes of the volumetric responses, from the peak friction angles appear to underestimate the expected critical state friction angle (i.e., $\phi'_{cs} = 34°$) for simple shear test responses at typical confining pressures. At typical confining

pressures (i.e., $\sigma'_v = 100$ to 300 kPa), the expected critical state friction angle appears to be better estimated by the friction angle determined at the constant volume state of the simple shear test responses. The observation that the constant volume friction angles are noticeably greater than the estimated critical state friction angles may be a due to limitations of the simple shear testing apparatus at low confining pressures. The simple shear system apparently fails to capture the post-peak response after full dilation of the medium density South Beach sand specimens. The dilatant behavior is captured in the volumetric response of the simple shear tests, and by definition, dilation should differentiate the peak and critical state friction angles (Bolton, 1986).

The corrected simple shear responses show that the estimated peak friction angles near the surface of the sediment bed also increase. Figure 4.8 shows that the estimated peak friction angles may approach values similar to the magnitude of the the pocket-friction angle near the surface of the sediment bed. This observation coincides with the findings of Booth et al. (2014), that the transition of the response of a sediment continuum to individual particles produces friction angles that increase exponentially.

An obstacle in relating the estimated peak friction angles from the simple shear test responses to the pocket-friction angle determined with inclined plane testing, is the effect of the density state of the sediment. It is not reasonable to assume that, because the estimated peak friction angles determined from the corrected low confinement simple shear responses of the medium dense specimens appear to approach a similar magnitude to the reported pocket-friction angle, that the two measures correspond. From the background knowledge provided in §2.3, it is evident that denser arrangements of soil exhibit greater dilation than loose arrangements of soil. If this re-

lationship is extended to low confinement responses, as postulated by Ponce and Bell (1971) and shown in Figure 2.6, then it is assumed that the response of loose South Beach sand specimens would produce lower peak friction angles than the medium density specimens utilized in simple shear testing herein. A more reasonable hypothesis for the relationship between the two characteristic friction angles may be that the peak friction angles of loose specimens sheared under very low confining pressures approach the pocket-friction angle of the least stable free particles on a rough fixed sediment bed. Similarly, the peak friction angles of dense specimens tested under very low confining pressures may approach the pocket-friction angle of the most stable free particles on a rough fixed sediment bed.

To further investigate the effect of specimen density state on the peak friction angle at low confinement, simple shear tests (or other geotechnical shearing tests capable of low confinement testing) could be performed on specimens for an array of relative densities, from very loose to very dense. As discussed in §3.3.4, the average pocket-friction angle reported herein is the angle defining the incipient motion of the least free stable particles on the rough sediment bed of fixed particles on the inclined plane board. Free particles were observed to experience incipient motion at higher angles than the reported average pocket-friction angle of the least stable particles with continued inclination of the fixed sediment rough board, indicating that those particles were in a more stable position. Improved imaging techniques and analyses of inclined plane tests could reveal the distribution of the pocket-friction angles for free particles with a range of stability conditions on the rough bed of fixed sediment.

The curves in Figure 4.8 which show the peak friction angles predicted by Equa-

tions 2.11 and 2.12 appear to produce somewhat similar trends to the estimated peak friction angles from corrected simple shear test responses. The predictions from Equation 2.12 for low confinement peak friction angles given by Chakraborty and Salgado (2010) show an increase in peak friction angle at simulated shallow depths. However, the increase is more gradual until depths between 1 m and the surface of the simplified sediment bed, where a sharp increase is observed. The predicted peak friction angles from Equation 2.12 appear to underestimate the peak friction angles estimated from the corrected simple shear responses. There are challenges involved with enforcing consistent specimen preparation of known density states in the simple shear testing device, as discussed in §3.3.2, which limits confidence in the accuracy of the peak friction angles estimated from the loading responses. As discussed in §2.3, the peak friction angle is a function of specimen dilation, which depends on the specimen's density state and confining pressure applied. Insufficient corrections for system resistance effects of the simple shear testing device could also contribute to the deviation of the predicted peak friction angles to those estimated from the corrected simple shear responses, but it is also likely that Equation 2.12 does not accurately estimate the response of South Beach sand at low confinement, because the relationship developed in Chakraborty and Salgado (2010) was calibrated exclusively for the low confinement response of Toyoura sand. As noted by Fukushima and Tatsuoka (1984), low confinement strength testing should be performed for the sediment of interest, because the change is friction angle at very low confining pressures vary greatly, even for similar soils.

Informed by the findings and proposed relationships herein, Figure 2.7 produced

by (Ponce and Bell, 1971) is modified to summarize the predicted response of very loose South Beach sand. Figure 4.9 shows the schematic representation of the predicted resistance mechanisms contributing to the mobilized characteristic friction angles of South Beach sand. As discussed in §2.3, very loose sand sheared under extremely low confining pressures is expected to exhibit dilation, similar to the dilation expected of a dense sand sheared under typical confining pressures (Ponce and Bell, 1971). From the conclusions outlined in the preceding discussions, it is predicted that the peak friction angles of the loose South Beach sand at low confinement approach the lower bound of the pocket-friction angle (i.e., the average pocket-friction angles for the least stable free particles on a rough bed of fixed particles). The corrected simple shear responses, in addition to the findings in Sadrekarimi and Olson (2011), also inform the predicted increase of the critical state friction angle at low confinement, perhaps approaching the angle of repose.

Figure 4.9 shows that the difference between the sliding friction angle and the critical state friction angle for more typical confining pressures is due to particle rearranging, as stated by Rowe (1962) and Ponce and Bell (1971). For decreasing confining pressures, the difference between the sliding friction angle and the critical state friction angle is shown as an alternate friction angle, ϕ'_{alt}. The mechanisms contributing to ϕ'_{alt} being larger than ϕ'_r to account for the increase in critical state friction angle at low confinement shown in Figure 4.9 are not straighforward. It is assumed that the sliding friction angle remains constant at low confinement, for which the literature relating to low confinement response of sands investigated herein has not shown otherwise. Mitchell and Soga (2005) also discussed the uncertainties of

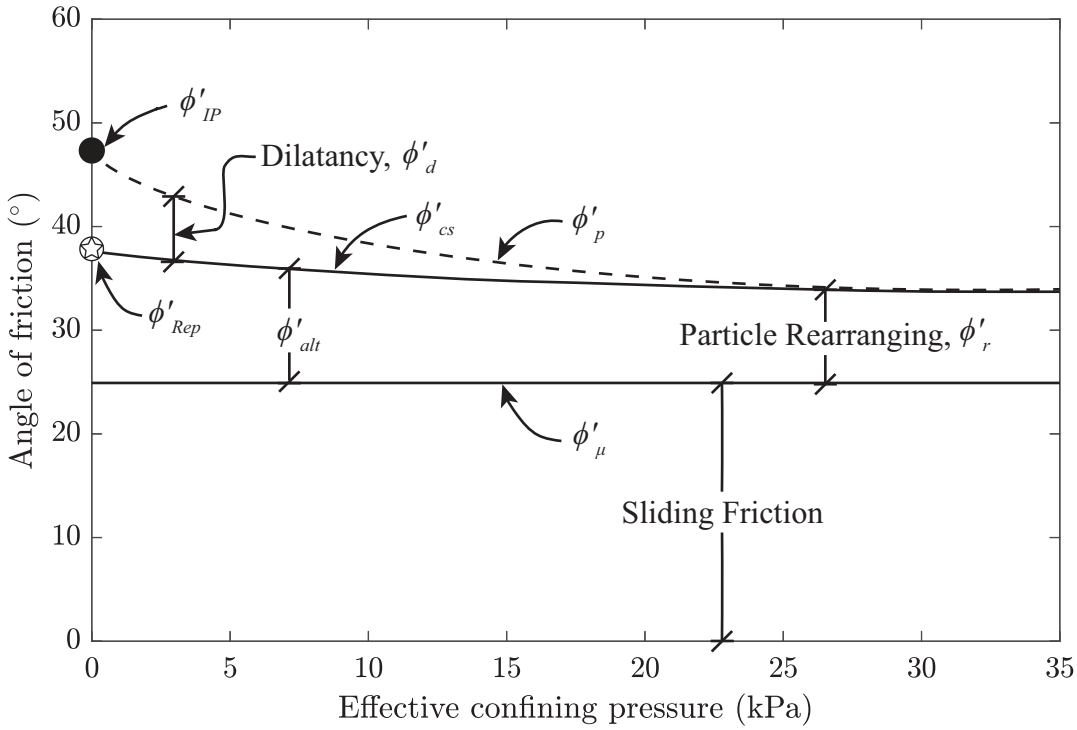

Figure 4.9: Modified components of strength with decreasing confinement. The schematic representation shows the modified components of mobilized friction angles for loose South Beach sand (modified after Ponce and Bell, 1971).

the contributing resistance mechanisms to mobilized sediment shear strength, due to inhomogeneous loading conditions. Sadrekarimi and Olson (2011) postulates that the increase in the critical state friction angle under low confining pressures is due to increased particle interlocking. An increase in particle rearranging could also possibly contribute to the increase in critical state friction angle, or perhaps some combination of contributing mechanisms. The definition of critical state friction angle informs the conclusion that no dilative effects should be present. Detailed studies should be performed to further reveal the contributing mechanisms leading to the increases of the critical state friction angle of South Beach sand at low confinement.

4.3 Outcomes and Results of South Beach Sediment Investigation

The work herein determined geotechnical testing and analysis techniques that provided reasonable results, based on the respective laboratory testing program investigating South Beach sand. The detailed evaluation of methods also exposed flaws and deficiencies in the reliability of results from some procedures. These details have been discussed throughout the preceding sections of this Chapter. The methods performed in the evaluation of South Beach sediment to determine index properties and the loading response under various confinement conditions shows that (parenthetical section specifiers provided to locate the detailed topic discussions):

- Sieve analyses of the fine sand is susceptible to the phenomena of sieve overloading, consequently overestimating the size of the gradation of particles within the collection of soil (§4.1.1)

- Visual methods of classifying sediment are preferred to those that employ fitted circles to particle image projection outlines (§4.1.2)

- Fitted ellipses to particle image projection outlines provide a useful and simplistic model of sediment particles, and can also provide a measure of particle sphericity based on the ellipse aspect ratio (§4.1.2)

- Fitted ellipse models can provide an approximation of the grain-size distribution curve, assuming oblate spheroids and the equivalent sieve size as the particle size, within a difference of d_{50} of 0.04 mm of that produced by sieve analysis (§4.1.3)

- The average value of the particle roundness shape parameter used to estimate the limiting void ratios by existing correlations provides a good comparison of results and improves the confidence of reported limiting void ratios, because there are limitations with the applicability of standardized laboratory procedures and uncertainty in the results (§4.1.4)

- The simple shear testing apparatus utilized herein appears to provide meaningful observations of the low confinement response of South Beach sand, down to a limiting confining pressure ($\sigma'_v \approx 10$ kPa) (§4.2)

- Results from surficial particle strength tests (angle of repose and inclined plane testing) were informative to compare to low confinement simple shear test responses (§4.2)

- ASTM C1444-00 (2000) provided more consistent measures of the angle of repose than the methods suggested by Santamarina and Cho (2001) (§3.3.3)

The listed outcomes of the evaluation of testing methods and analysis techniques are determined specifically for the South Beach sand investigated for the specific applications outlined. The focus herein was to better understand the sediment properties and loading response of South Beach sand for the near-surface environment. It will be a product of future work and subsequent researchers to continue to determine what properties of the respective sediment are appropriate to include for the sediment instability and transport applications of interest.

Table 4.2 shows the developed database of index properties and strength parameters that govern the response of South Beach sand. Table 4.2 shows parameters

determined specifically for the DTL sediment samples obtained during the S10 sampling effort, for consistency.

South Beach sediment classification: (SP) Clean, poorly-graded, subrounded, fine sand (Powers, 1953; ASTM D2487-11, 2011)

Table 4.2: South Beach sand property database.

d_{10} (mm)	d_{30} (mm)	d_{50} (mm)	d_{60} (mm)	C_u	C_c	G_s
0.17	0.19	0.21	0.22	1.35	1.01	2.69
r	s	e_{min}	e_{max}	ϕ'_{cs}	ϕ'_{Rep}	ϕ'_{IP}
0.36	0.74	0.67	0.9	34°	38°	47°

4.4 Implications for Sediment Instability

Herein, sediment properties and response characteristics that are relevant to sediment instability and transport model applications are the focus; however, as discussed in Chapter 1 and noted by other researchers (e.g., Ponce and Bell, 1971; Stroud, 1971; Fukushima and Tatsuoka, 1984; Chakraborty and Salgado, 2010), many other engineering applications may benefit from defined near-surface sediment properties and loading responses. The characterization of the near-surface sediment region will inform analysis techniques that consider more geotechnical properties, leading to improved infrastructure design. Due to the general homogeneity determined for the cross section investigated at South Beach, Newport, Oregon, the beach characteris-

tics and sediment properties defined herein are likely representative of the specific cross section for the foreseeable future, notwithstanding significant morphological changes from impending natural disasters or human-induced changes, as discussed in §2.1. Although slightly different particle size, gradation, and shape parameters were observed for samples from different locations of the beach cross section and different sampling dates, the differences are considered to be of minimal influence, especially because the slight differences observed may be due to limitations of laboratory testing methods (e.g., sieve overloading potential may limit the meaningful observation of slight gradation discrepancies between the investigated specimens). However, the slight differences in sediment properties, if verified, could be important for specific sediment transport applications.

The apparently stable environment of the South Beach cross section investigated allows for the sediment parameters defined herein (summarized in Table 4.2) to be utilized as inputs to a more inclusive sediment transport model for South Beach in combination with specific overflow characteristics of interest (e.g., an estimated tsunami wave following a Cascadia Subduction Zone earthquake). The detailed sediment transport model could be developed to include specific sediment characteristics, not typically defined in classic sediment transport models (e.g., Shields, 1936; Soulsby, 1997; Sleath, 1999).

As discussed in Chapter 1, the specific sediment properties and loading response characteristics investigated herein are influential for near-surface sediment instability applications. Particle size, typically the mean grain-size diameter, d_{50}, is utilized in classic sediment transport models (e.g., Shields, 1936). Other index properties

determined from a particle size analysis (e.g., C_u, C_c, other characteristic particle diameters) are also influential to the response of sediment to perturbation (Bardet, 1997; Santamarina et al., 2001). Particle shape parameters, specifically average particle roundness, have been directly correlated to limiting packing densities (i.e., limiting void ratios) and shear strength (i.e., critical state friction angle) of a collection of soil particles (Santamarina and Cho, 2004). Particle shape analysis which generates fitted ellipses to particle image projection outlines (e.g., Simpson, 2014) can be used to approximate three-dimensional particle shape parameters, such as CSF or $A^{\star}_{mmm}$, from the assumption of prolate or oblate spheroid models. As discussed in §2.4, CSF and $A^{\star}_{mmm}$ are influential particle shape parameters used to estimate drag effects in flow analyses (Loth, 2008). The state of sediment fabric (i.e., packing density or in situ void ratio or porosity), in combination with applied confining pressures, determines the dilatant response of a collection of soil particles subjected to shearing (Bolton, 1986; Chakraborty and Salgado, 2010). The determination of limiting void ratios of a collection of soil allows the meaningful definition of relative density state for in situ sediments or laboratory specimens, which allows a more detailed evaluation of shear strength (i.e., determination of peak friction angles for specific density states and levels of confinement).

The characteristic friction angles of South Beach sand determined for different loading and confinement conditions (i.e., spectrum of critical state and peak friction angles for different sediment states, angle of repose, pocket-friction angle) will be informative for estimating the resistance of the sediment to imposed shear stresses in near-surface environments. Defining appropriate strength properties for sediment

instability applications will provide more accurate sediment response predictions for near-surface deposits subjected to bed-shear stresses. As discussed in §2.4, common analyses in sediment transport models correlate sediment shear strength to observed sediment instability databases, in the form of empirical relationships. The correlations are often based on soil index properties such as the mean grain-size diameter, specific gravity, and packing density, and do not consider other important index properties, such as particle shape, or the loading response of the sediment under various levels of confinement (e.g., Shields, 1936; Soulsby, 1997; Sleath, 1999; Yeh and Mason, 2014).

When considering sediment response due to imposed overflows on the surface of a sediment bed, pore-water pressure changes within the sediment deposit will also govern the response. Pore-water pressure changes alter the effective stresses within the sediment deposit. Sediment shear strength, which governs the response to perturbation, is dependent on the effective stresses within the sediment deposit (i.e., confining stress), as discussed in §2.3 and shown in Equation 2.8. Pore-water pressure changes are governed by the hydraulic conductivity, or permeability, of a sediment deposit. Characteristics of overflowing waves, such as tsunamis, will govern the water pressure imposed at the surface of a sediment bed. Wave height, length, and velocity will all affect the induced pressures and affect how seepage and resulting pore-water pressures will change within the sediment bed. As discussed, specific sediment properties will also govern the pore-water pressure changes.

The coefficient of consolidation, c_v, a factor that governs the permeability of a collection of soil, has a large expected range for South Beach sand, based on the sediment properties defined herein (Holtz et al., 2011). The coefficient of consolidation

can be estimated via Equation 2.25. Typical values for hydraulic conductivity of fine sands are provided by Duffield (2016) as $k = 2 \times 10^{-4}$ mm/s to 2×10^{-1} mm/s. The constrained modulus can be estimated from the range of modulus of elasticity values estimated from the triaxial and simple shear test responses, and the average value of Poisson's ratio determined from triaxial testing, $\nu = 0.3$. Due to the variation of hydraulic conductivity for fine sand and the estimated stiffness under different confining conditions, the estimates of coefficient of consolidation have a large range. The coefficient of consolidation estimated from parameters determined in the current study, and from published ranges of hydraulic conductivity, yield $c_v = 14$ mm^2/s to 2×10^6 mm^2/s. These values lie outside the range of expected c_v values for sands, summarized by Yeh et al. (2001) as $c_v \approx 1 \times 10^3$ mm^2/s to 1×10^6 mm^2/s. Test results specific to South Beach sand could provide improved measures of estimated c_v values.

Clearly, the defined characteristics of the near-surface region of a sediment deposit will lead to improved predictions of sediment response for various applications. The results of the current study will inform more inclusive and detailed sediment transport and instability analyses methods that consider specific properties and response trends of near-surface deposits.

Chapter 5: Conclusion

A primary goal of the work herein was to create a database of relevant sediment properties for beach sands sampled at South Beach, Newport, Oregon. To create the database, surficial sediment samples were obtained from the selected beach cross-section at South Beach, Newport, Oregon. Samples were taken at various tidal marks throughout the course of the study to observe the spatial and temporal variability of the South Beach site. In particular, the relevant sediment properties were selected to be applicable as input parameters for sediment instability and transport models. In addition to defining the sediment index properties (e.g., mean grain-size diameter, particle shape, limiting void ratios), the response of the sediment to different forms of perturbation was investigated to observe the sediment strength properties. More specifically, various definitions of the friction angle were determined for the South Beach sand with different displacement mechanisms and confining conditions applied to the sediment (i.e., simulating soils at different in situ depths). The characterization of a natural beach sand also provided opportunities to investigate existing correlations, such as estimating limiting void ratios and friction angles from particle shape parameters.

The characterization of the sampled South Beach sediment required a laboratory program. The sediment samples were subjected to sieve analyses, particle shape analyses, specific gravity testing, minimum and maximum packing density testing,

consolidated-drained triaxial compression testing, constant vertical stress simple shear compression testing, angle of repose testing, and inclined plane testing. The laboratory based characterization of the sediments also allowed for a unique set of research questions, which were given in §1.2, to be answered. In particular, the laboratory program was unique, because few researchers have related low confinement test results, used to simulate the near-surface sediment response, to particle behavior under little to no confinement at the surface of the sediment bed, especially for fine beach sands.

5.1 Research Question Responses

The first research question is, "What are the morphological characteristics of the South Beach, Newport, Oregon site and how do they change during the course of this study?" The investigated beach cross section of South Beach, Newport, Oregon was determined to be fairly stable and homogeneous. Although slight temporal and spatial differences were observed from the particle size and shape analyses, the differences were not large enough to change the general classification of the sediment, defined as a subrounded, poorly-graded, fine sand. The slight differences in grain size may be important for applications such as sediment transport predictions, depending on the type of loading. It should also be noted that historical beach elevation profiles from 1994 onward were examined, and that the beach slope and general beach morphology has not changed considerably during that duration.

The second research question is, "How well do existing correlations relating soil

index properties and the response of granular materials apply to the South Beach sand studied herein?" Correlations utilizing particle shape characteristics, specifically roundness, predict a reasonable range of limiting void ratios, and provide a rough estimate of the critical state friction angle. The resulting estimates of limiting void ratios provided a slightly larger range than determined in the laboratory, but are concluded to be reasonable considering the deviations from standardized laboratory procedures and inherent uncertainties of the laboratory methods used herein. The resulting critical state friction angle estimate was between that derived by triaxial testing and the angle of repose.

The third research question is, "How does the friction angle and the mechanism of mobilized shear strength change in the near-surface region of the sediment bed for South Beach sand?" The friction angles of the sediment under low confining pressure are observed to increase with respect to friction angles measured at deeper depths. The critical state friction angle appears to be well estimated by the angle of repose near the surface, and the peak friction angle for medium density sediment appears to be of similar magnitude to the pocket-friction angle near the surface. The mechanism contributing to the increase in peak friction angle near the surface is due to enhanced dilatant effects. The mechanism contributing to the increase in the critical state friction angle is less apparent. By definition, the critical state friction angle should not possess any contributions from dilation; therefore, the mechanisms contributing to the increase in observed critical state friction angle should be attributed to a combination of sliding friction and particle rearranging. However, clarification of this conclusion is needed, because there are uncertainties in attributing specific resistance

mechanisms to mobilized friction angles.

The fourth research question is, "How are dilatant behavior and stiffness of the sediment affected by shearing at low confining pressures in the utilized simple shear device?" Dilatant behavior of the tested specimens, observed through the volumetric response during simple shear testing, and through the estimated dilation angles, increases with decreasing specimen confining pressures. Specimens that do not typically exhibit notable dilatant behavior (i.e., medium density states) produced dilation angles up to approximately 10° under very low confinement. The stiffness of the tested specimens, measured by the shear modulus estimated from simple shear responses, showed a substantial decrease with decreasing specimen confining pressures.

The fifth research question is, "Is simple shear testing a sufficient method to investigate low confinement behavior?" The simple shear device is observed to capture the effect of increasing friction angles with decreasing confinement, down to the lowest confining pressure that the system could apply ($\sigma'_v = 6$ kPa). The simple shear device fails to capture the detailed loading response after the maximum shear stress is reached, so dilation must be determined through the volumetric response to estimate the critical state friction angle. Additionally, the true influence of the system resistance on the measured responses is difficult to determine for the simple shear apparatus. The simple shear test appears to produce more meaningful results above a threshold confining pressure ($\sigma'_v \approx 10$ kPa).

The sixth research question is, "What effect would the implementation of the specific near-surface sediment properties and response have on sediment instability and transport models?" The friction angle is a major contributor to the determination of

incipient motion. Clearly, it is important to employ the appropriate friction angle for the application of interest. With the range of characteristic friction angles determined herein for various in-situ conditions, it is evident that a single value of friction angle for a given sediment (e.g., the critical state friction angle for typical geotechnical confining pressures) is not sufficient to predict the response in near-surface environments. Considering particle size, gradation, shape, particle and packing densities, and the spectrum of friction angles for a given sediment deposit would result in improved analyses predicting the response of near-surface sediment deposits to different types of perturbation.

As discussed, the friction angle is evidently an important parameter for sediment stability problems. The friction angle defines the strength of granular material and governs the incipient motion of the particles at the surface, as well as the response of the underlying sediment deposit. The unique critical state friction angle defined for the assumed medium density deposit at depths larger than approximately 3 m is $\phi'_{cs} = 34°$. The increase in critical state and peak friction angles ($\phi'_{cs} \approx 34$ to $38°$ and $\phi'_p \approx 40$ to $50°$) is apparent in the simulated transitional region between a depth of approximately 3 m and the surface of the simulated dry, medium dense sediment bed. The assumption that the entire soil deposit possesses a uniform friction angle (which would likely be assumed as $\phi' = 34°$) would be overly simplistic and greatly affect the results of sediment instability and transport models, by not accounting for the strength changes near the surface. Specifically, the assumption of a uniform critical state friction angle for a deposit would lead to larger predictions of sediment transport than would likely be observed. Notably, the answer to the sixth research

question is overly simplified, and is recommended for future work.

In closing, the current study aims to help bridge the gap between geotechnical and coastal engineering communities when modeling sediment instability and transport problems, which will ultimately lead to improved coastal engineering practices and infrastructure design. Although a coastal focus is adopted herein, understanding sediment response near the surface is important for various engineering applications involving low-stress environments. The outcomes of this study revealed numerous areas of future work to be performed to further reveal the complexities of sediment near the ground surface. A natural expansion of the work herein would be to utilize the defined beach properties of the respective South Beach, Newport, Oregon cross section, the sand index properties, and the near-surface sediment loading response trends (i.e., characteristic friction angles), as inputs to to a sediment transport model. The inclusive model could be used to predict the near-surface response of the specific beach cross section to tsunami-induced bed-shear stresses.

Bibliography

Airey, D. W., Budhu, M., and Wood, D. M., 1985. *Developments in soil mechanics and foundation engineering*, vol. 2. Elsevier Applied Science Publishers, London.

ASTM C136/C136M-14, 2014. Standard test methods for sieve analysis of fine and coarse aggregates. *ASTM International, West Conshohocken, PA,* pp. 1–5.

ASTM C1444-00, 2000. Standard test methods for measuring the angle of repose of free-slowing mold powders. *ASTM International, West Conshohocken, PA,* pp. 1–2.

ASTM D2487-11, 2011. Standard practice for classification for soils for engineering purposes (Unified Soil Classification System). *ASTM International, West Conshohocken, PA,* pp. 1–12.

ASTM D422-63, 2007. Standard test methods for particle-size analysis of soils. *ASTM International, West Conshohocken, PA,* pp. 1–8.

ASTM D4253-16, 2016. Standard test methods for maximum index density and unit weight of soils using a vibratory table. *ASTM International, West Conshohocken, PA,* pp. 1–14.

ASTM D4254-16, 2016. Standard test methods for minimum index density and unit weight of soils and calculation of relative density. *ASTM International, West Conshohocken, PA,* pp. 1–9.

ASTM D6913-04, 2009. Standard test methods for particle-size distribution (gradation) of soils using sieve analysis. *ASTM International, West Conshohocken, PA,* pp. 1–34.

ASTM D7181-11, 2011. Standard test methods for consolidated drained triaxial compression test for soils. *ASTM International, West Conshohocken, PA,* pp. 1–11.

ASTM D854-10, 2010. Standard test methods for specific gravity of soil solids by water pycnometer. *ASTM International, West Conshohocken, PA,* pp. 1–8.

Atkins, J. E. and McBride, E. F., 1992. Porosity and packing of Holocene river, dune, and beach Sands. *The American Association of Petroleum Geologists Bulletin,* **76(3)**, 339–355.

Atkinson, J. H., Lau, W. H. W., and Powell, J. J. M., 1991. Measurement of soil strength in simple shear tests. *Canadian Geotechnical Journal,* **28**, 255–262.

Atwater, B. F., Nelson, A. R., Clague, J. J., Carver, G. A., Yamaguchi, D. K., Bobrowsky, P. T., Bourgeois, J., Darienzo, M. E., Grant, W. C., Hemphill-Haley, E. et al., 1995. Summary of coastal geologic evidence for past great earthquakes at the Cascadia subduction zone. *Earthquake Spectra,* **11(1)**, 1–18.

Bardet, J.-P., 1997. *Experimental soil mechanics.* Prentice-Hall, Inc., Upper Saddle River, NJ.

Bishop, A. W. and Henkel, D. J., 1962. *The measurement of soil properties in the triaxial test.* 2 edn. Edward Arnold LTD, London.

Black, D. K. and Lee, K. L., 1973. Saturating laboratory samples by back pressure. *Journal of the Soil Mechanics and Foundations Division,* **99(1)**, 75–93.

Bolton, M. D., 1986. The strength and dilatancy of sands. *Géotechnique,* **36(1)**, 65–78.

Booth, A. M., Hurley, R., Lamb, M. P., and Andrade, J. E., 2014. Force chains as the link between particle and bulk friction angles in granular material. *Geophysical Research Letters,* **41(24)**, 8862–8869.

Chakraborty, T. and Salgado, R., 2010. Dilatancy and shear strength of sand at low confining pressures. *Journal of Geotechnical and Geoenvironmental Engineering,* **136(3)**, 527–532.

Cho, G.-C., Dodds, J., and Santamarina, J. C., 2006. Particle shape effects on packing density, stiffness, and strength: Natural and crushed sands. *Journal of Geotechnical and Geoenvironmental Engineering,* **132(5)**, 591–602.

Cluff, L., 2007. Effects of the 2004 Sumatra-Andaman earthquake and Indian Ocean tsunami in Aceh province. *The Bridge,* **37(1)**, 12–16.

Coduto, D. P., 2001. *Foundation design: Principles and practices.* 2 edn. Prentice-Hall, Inc., Upper Saddle River, NJ.

Dick, J. E. and Sleath, J. F. A., 1992. Sediment transport in oscillatory sheet flow. *Journal of Geophysical Research,* **97(C4)**, 5745–5758.

DOGAMI, 2011. Oregon Department of Geology and Mineral Industries (DOGAMI) - Oregon beach and shoreline mapping and analysis program (OBSMAP): Pacific Northwest estuaries and shores. Accessed: Apr. 8, 2017 <http://www.oregongeology.org/sub/Nanoos1/index.htm>.

Duffield, G. M., 2016. AQTESOLV - Representative values of hydraulic properties. Accessed: Jun. 6, 2017 <http://www.aqtesolv.com/aquifer-tests/aquifer_properties.htm>.

EERI, 2011. The Japan Tohoku Tsunami of March 11, 2011. *Earthquake Engineering Research Institute (EERI), Special Earthquake Report - November 2011, Learning from Earthquakes,* pp. 1–15.

Flores, N. Z. and Sleath, J. F., 1998. Mobile layer in oscillatory sheet flow. *Journal of Geophysical Research,* **103(C6)**, 12783–12793.

Fredlund, M. D., Fredlund, D. G., and Wilson, G. W., 2000. An equation to represent grain-size distribution. *Canadian Geotechnical Journal,* **37**, 817–827.

Fukushima, S. and Tatsuoka, F., 1984. Strength and deformation characteristics of saturated sand at extremely low pressures. *Soils and Foundations,* **24(4)**, 30–48.

Head, K., 1998. *Manual of soil laboratory testing - Effective stress tests*, vol. 3. 2 edn. John Wiley & Sons, USA.

Holtz, R. D., Kovacs, W. D., and Sheahan, T. C., 2011. *An introduction to geotechnical engineering.* 2 edn. Pearson Education, Inc., Upper Saddle River, NJ.

Holubec, I. and D'Appolonia, E., 1973. Effect of particle shape on the engineering properties of granular soils. *American Society for Testing and Materials,* **STP 523**, 304–318.

Houlsby, G. T., 1991. How the dilatancy of soils affects their behaviour. In *Tenth European conference on soil mechanics and foundation engineering*, OUEL 1888/91. University of Oxford, Department of Engineering Science, U.K.

Hryciw, R. D., Zheng, J., Ohm, H.-S., and Li, J., 2014. Innovations in optical geocharacterization. *Geo-Congress 2014 Keynote Lectures,* **GSP 235**, 97–116.

Kraupa, T. J., 2013. Static and cyclic response of ecoroof soil. Master's thesis, Oregon State University: Civil Engineering.

Krumbein, W. C. and Sloss, L. L., 1963. *Stratigraphy and sedimentation*. 2nd edn. Freeman and Company, San Francisco, CA.

Kwan, W. S. and El Mohtar, C., 2014. Comparison between shear strength of dry sand measured in CSS device using wire-reinforced membranes and stacked rings. In *Geo-Congress 2014: Geo-characterization and Modeling for Sustainability*, pp. 1111–1119.

Lambe, T. W. and Whitman, R. V., 1969. *Soil Mechanics*. John Wiley & Sons, USA.

Lee, K. L. and Seed, H. B., 1967. Drained strength characteristics of sands. *Journal of Soil Mechanics and Foundations Division,* **93(6)**, 117–141.

Loth, E., 2008. Drag of non-spherical solid particles of regular and irregular shape. *Powder Technology,* **182**, 342–353.

Miller, R. L. and Byrne, R. J., 1966. The angle of repose for a single grain on a fixed rough bed. *Sedimentology,* **6**, 303–314.

Mitchell, J. K. and Soga, K., 2005. *Fundamentals of soil behavior*. 3rd edn. John Wiley & Sons, Inc., Hoboken, NJ.

NOAA, 2013. National Oceanic and Atmospheric Administration (NOAA) - Tides and currents. Accessed: Apr. 5, 2017 <https://tidesandcurrents.noaa.gov/stationhome.html?id=9435380>.

Ponce, V. M. and Bell, J. M., 1971. Shear strength of sand at extremely low pressures. *Journal of the Soil Mechanics and Foundations Division,* **97(4)**, 625–638.

Powers, M. C., 1953. A new roundness scale for sedimentary particles. *Journal of Sedimentary Petrology,* **23(2)**, 117–119.

Priest, G. R., Myers, E., Baptista, A. M., Fleuck, P., Wang, K., Kamphaus, R. A., and Peterson, C. D., 1997. *Cascadia subduction zone tsunamis: Hazard mapping at Yaquina Bay, Oregon. Tech. rep.*, Final technical report to the National Earthquake Hazard Reduction Program: Oregon Department of Geology and Mineral Industries Open-File Report O-97-34.

Rossato, G. and Simonini, P., 1991. Stress-strain behavior of sands in triaxial and direct simple shear tests. *Canadian Geotechnical Journal,* **28**, 276–281.

Rousé, P. C., 2014. Comparison of methods for the measurement of the angle of repose of granular materials. *Geotechnical Testing Journal,* **37(1)**, 164–168.

Rowe, P. W., 1962. The stress dilatancy relations for static equilibrium of an assembly of particles in contact. In *Royal Society*, vol. 269 of *A*, pp. 500–527. London.

Sadrekarimi, A. and Olson, S. M., 2011. Critical state friction angle of sands. *Géotechnique,* **61(9)**, 771–783.

Santamarina, J. C. and Cho, G. C., 2001. Determination of critical state parameters in sandy soils-simple procedure. *Geotechnical Testing Journal,* **24(2)**, 185–192.

Santamarina, J. C. and Cho, G. C., 2004. Soil behaviour: The role of particle shape. In *Advances in Geotechnical Engineering: The Skempton Conference*, pp. 604–617. Thomas Telford, London.

Santamarina, J. C., Klein, K. A., and Fam, M. A., 2001. *Soils and waves: Particulate materials behavior, characterization and process monitoring.* Wiley, New York.

Schulz, K., 2015. The really big one. *The New Yorker,* **20(7)**.

Schwarcz, H. P. and Shane, K. C., 1969. Measurement of particle shape by Fourier analysis. *Sedimentology,* **13**, 213–231.

Shields, A., 1936. *Application of similarity principles and turbulence research to bed-load movement. Tech. rep.*, Soil Conservation Service, California Institute of Technology, Pasadena (Translated from German by W. P. Ott and J. C. van Uchelen).

Shih, S.-M. and Komar, P. D., 1994. Sediments, beach morphology and sea cliff erosion within an Oregon coast littoral cell. *Journal of Coastal Research,* **10(1)**, 144–157.

Simpson, D. C., 2014. Behavioral threshold in mixtures of sand and clay. Master's thesis, Oregon State University: Civil Engineering.

Simpson, D. C. and Evans, T. M., 2015. Behavioral thresholds in mixtures of sand and kaolinite clay. *Journal of Geotechnical and Geoenvironmental Engineering,* **142(2)**, 1–10.

Skempton, A. W., 1954. The pore-water coefficients A and B. *Géotechnique,* **4(4)**, 143–147.

Skinner, A. E., 1969. A note on the influence of interparticle friction on the shearing strength of a random assembly of spherical particles. *Géotechnique,* **19(1)**, 150–157.

Sleath, J. F. A., 1999. Conditions for plug formation in oscillatory flow. *Continental Shelf Research,* **19(13)**, 1643–1664.

Soulsby, R. L., 1997. *Dynamics of marine sands.* Thomas Telford Publications, London.

Stark, N., Hay, A. E., Cheel, R., and Lake, C. B., 2014. The impact of particle shape on the angle of internal friction and the implications for sediment dynamics at a steep, mixed sand-gravel beach. *Earth Surface Dynamics,* **2(2)**, 469–480.

Stroud, M. A., 1971. The behavior of sand at low stress levels in the simple-shear apparatus. Ph.D. thesis, Cambridge University.

Sture, S., Costes, N. C., Batiste, S. N., Lankton, M. R., AlShibli, K. A., Jeremic, B., Swanson, R. A., and Frank, M., 1998. Mechanics of granular materials at low effective stresses. *Journal of Aerospace Engineering,* **11(3)**, 67–72.

Sumer, B. M. and Fredsøe, J., 2002. The mechanics of scour in the marine environment. vol. 17 of *Advanced Series on Ocean Engineering.* World Scientific, Singapore.

Tam, G., 2004. The Physics Factbook - The coefficients of friction for Teflon. Accessed: Apr. 18, 2017 <http://hypertextbook.com/facts/2004/GarvinTam.shtml>.

Tatsuoka, F., Sakamoto, M., Kawamura, T., and Fukushima, S., 1986. Strenth and deformation characteristics of sand in plane strain compression at extremely low pressures. *Soils and Foundations,* **26(1)**, 65–84.

Terzaghi, Peck, and Mesri, 1996. *Soil Mechanics in engineering practice.* 3 edn. John Wiley & Sons, USA.

Tonkin, S., Yeh, H., Kato, F., and Sato, S., 2003. Tsunami scour around a cylinder. *Journal of Fluid Mechanics,* **496**, 165–192.

Train, D., 1958. Some aspects of the property of angle of repose of powders. *Journal of Pharmacy and Pharmacology,* **10(S1)**, 127T–135T.

Vucetic, M., 1994. Cyclic threshold shear strains in soils. *Journal of Geotechnical Engineering* **120(12)**, 2208–2228.

Wijewickreme, D., Dabeet, A., and Byrne, P., 2013. Observations on the state of stress in the direct simple shear test using 3D discrete element analysis. *Geotechnical Testing Journal,* **36(2)**, 1–8.

Yang, F.-G., Liu, X.-N., Yang, K.-J., and Cao, S.-Y., 2009. Study on the angle of repose of nonuniform sediment. *Journal of Hydrodynamics,* **21(5)**, 685 – 691.

Yeh, H. and Mason, H. B., 2014. Sediment response to tsunami loading: Mechanisms and estimates. *Géotechnique,* **64(2)**, 131–143.

Yeh, H., Tonkin, S., Heller, E., Arduino, P., Kato, F., and Sato, S., 2001. Mechanisms of Scour Induced by Tsunami Runup. In *Proceedings of the 2nd International Conference on Scour and Erosion*, pp. 464–471. Singapore.

Youd, T. L., 1973. Factors controlling maximum and minimum densities of sands. *American Society for Testing and Materials,* **STP 523**, 98–112.

APPENDICES

Appendix A: Simple Shear Testing Results

Each plot shows the estimated point of the initial shear modulus, G_i, at 20% of the maximum shear stress, the secant shear modulus, G_{sec}, at 50% of the maximum shear stress, and the approximation of the point of no volume change or constant volume state (CV estimate).

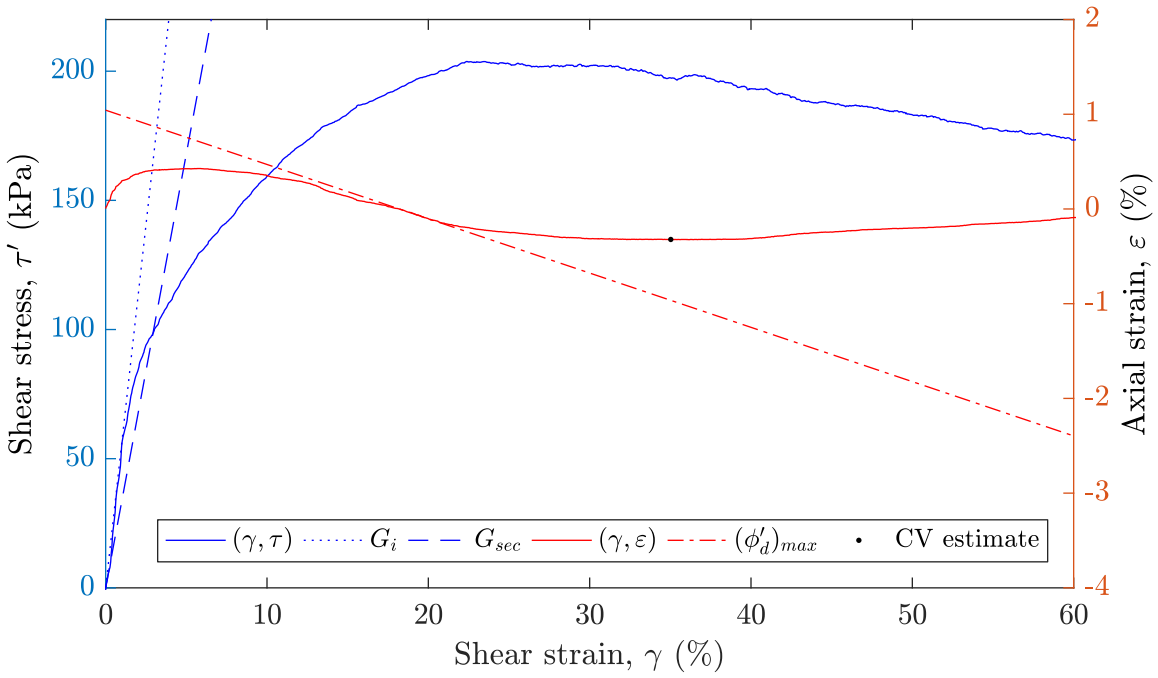

Figure A.1: SS1 $\sigma'_v = 300$ kPa simple shear test results.

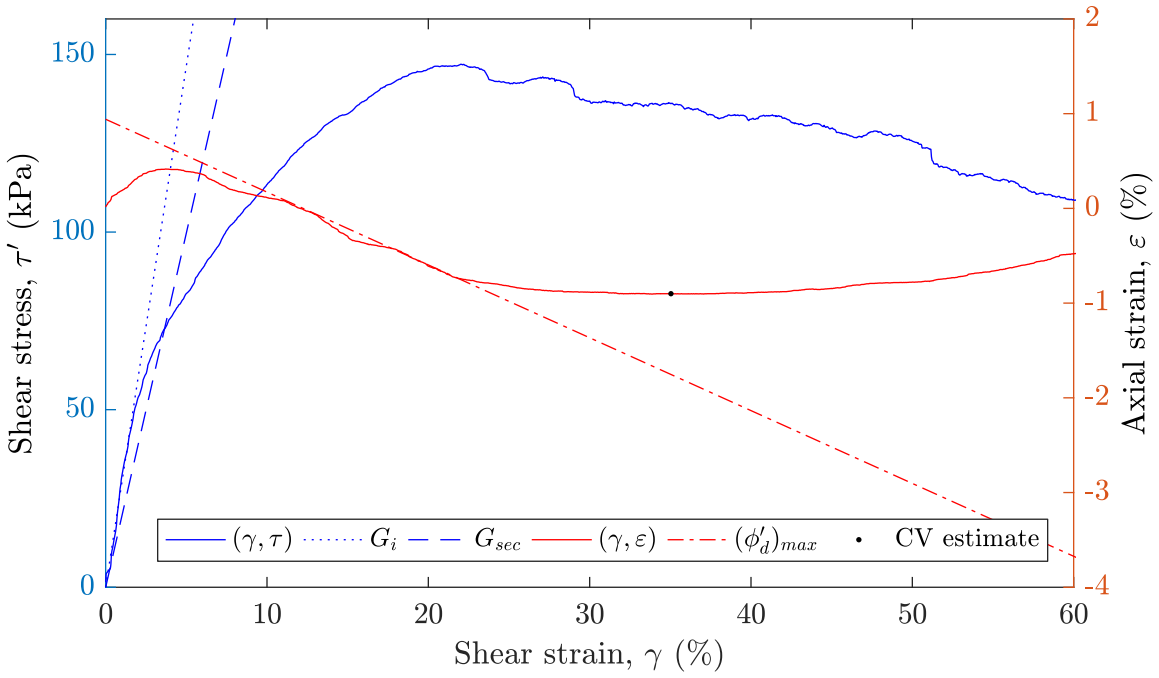

Figure A.2: SS2 $\sigma'_v = 200$ kPa simple shear test results.

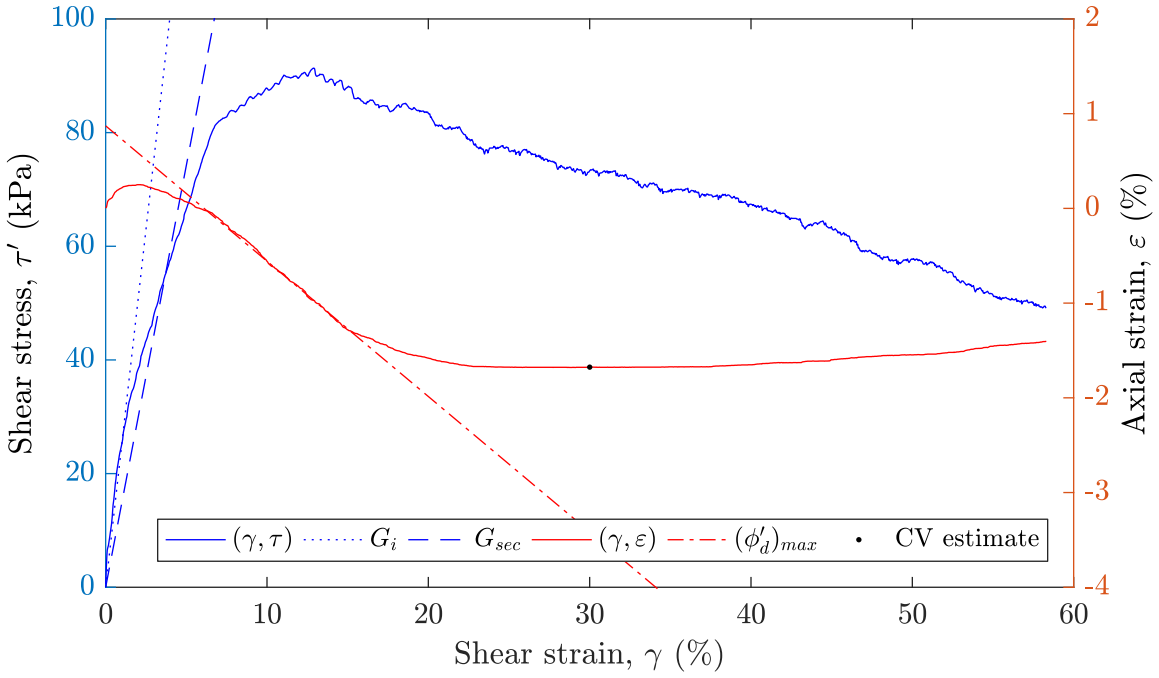

Figure A.3: SS3 $\sigma'_v = 100$ kPa simple shear test results.

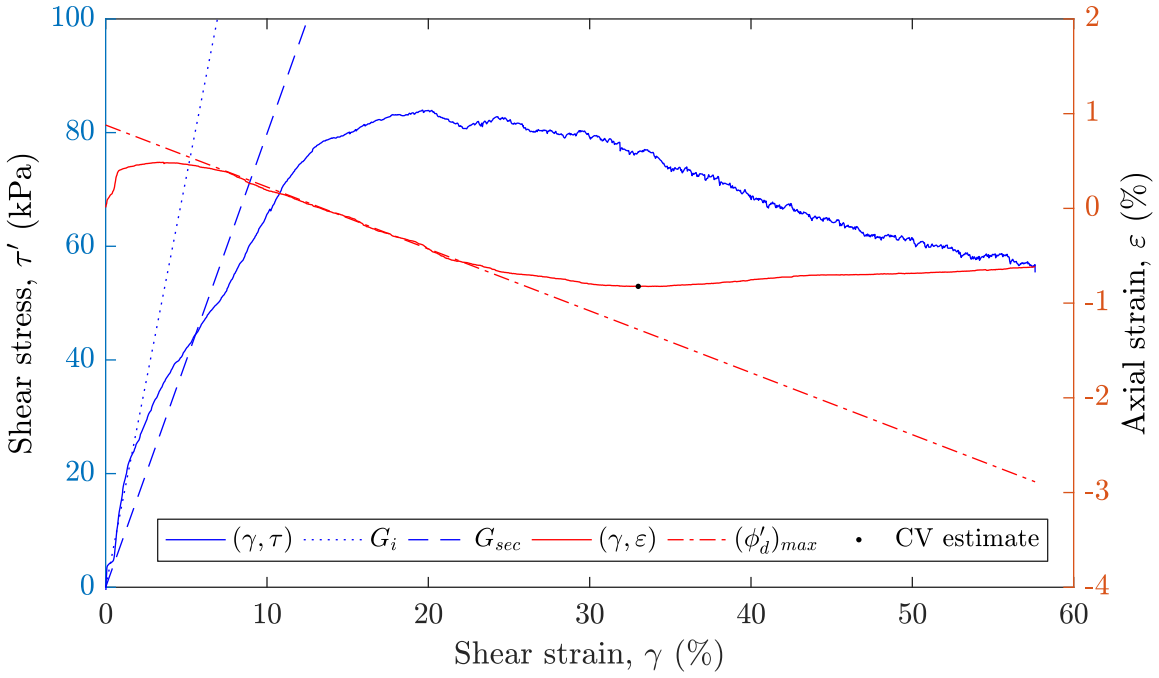

Figure A.4: SS4 $\sigma'_v = 100$ kPa simple shear test results.

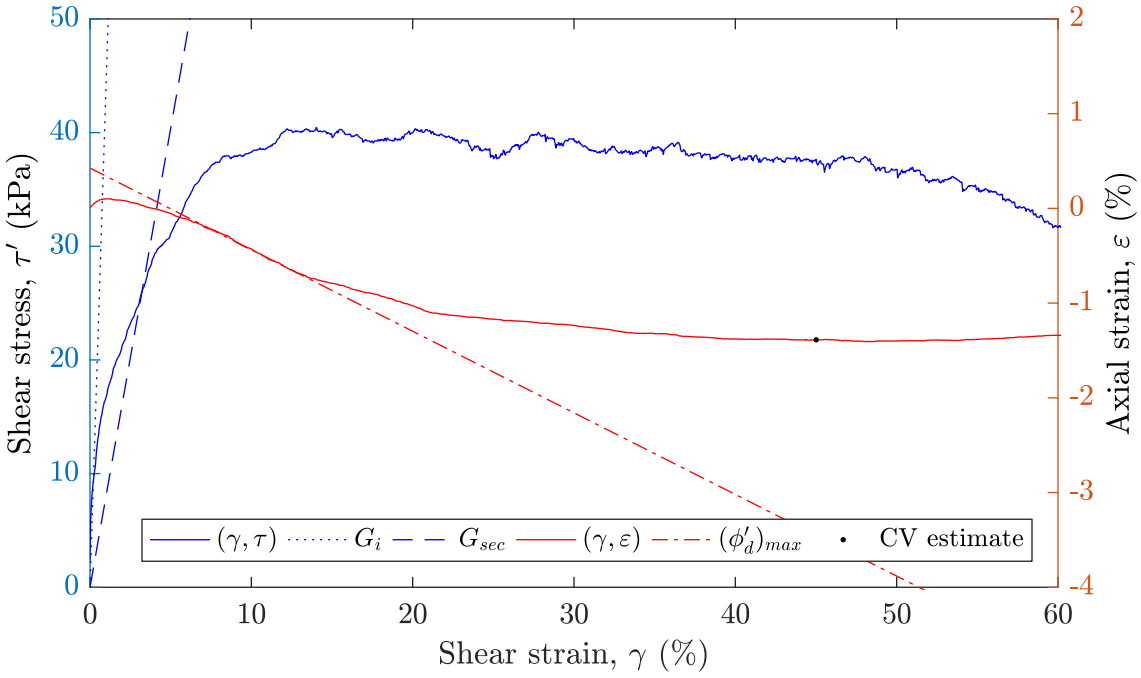

Figure A.5: SS5 $\sigma'_v = 50$ kPa simple shear test results.

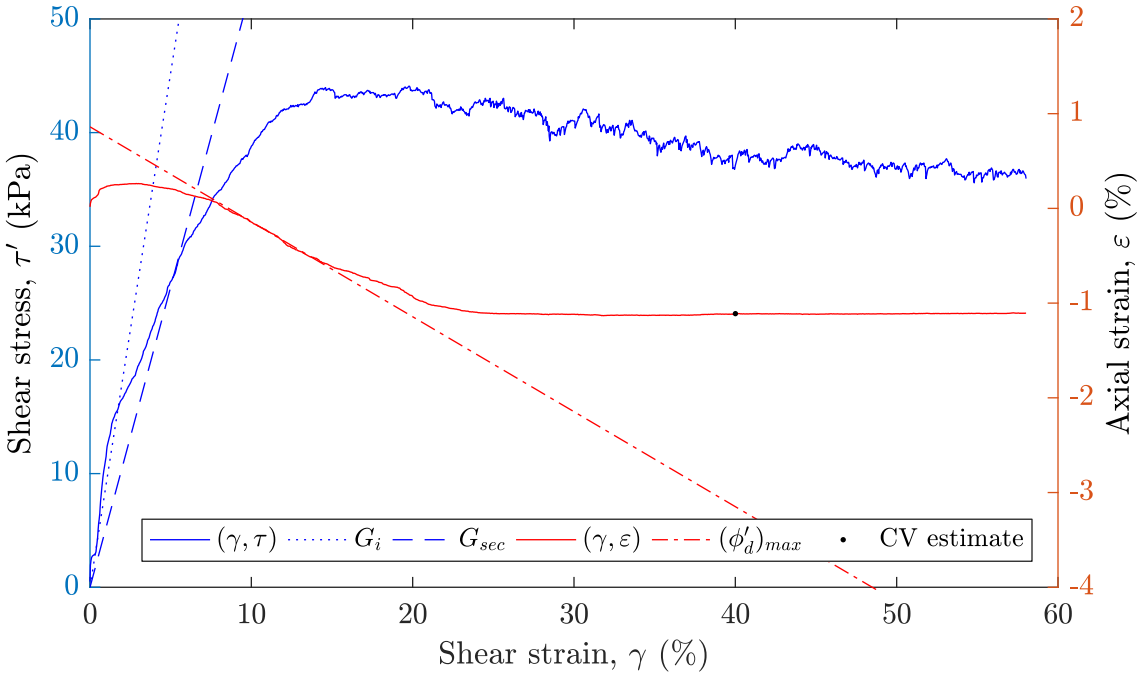

Figure A.6: SS6 $\sigma'_v = 50$ kPa simple shear test results.

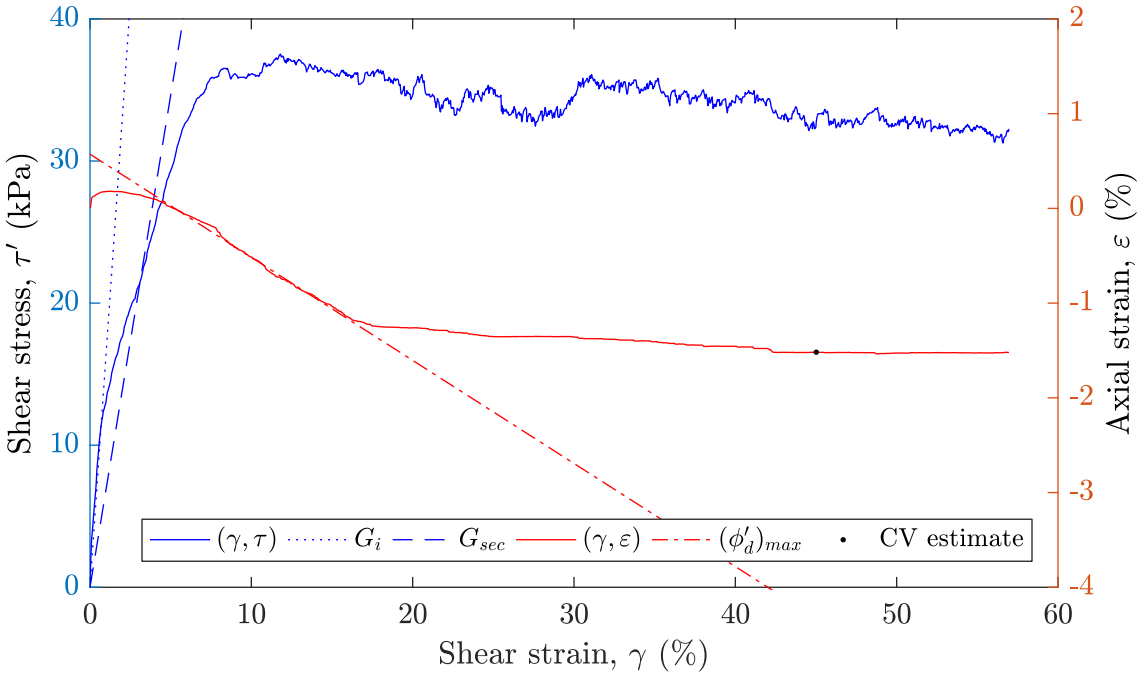

Figure A.7: SS13 $\sigma'_v = 40$ kPa simple shear test results.

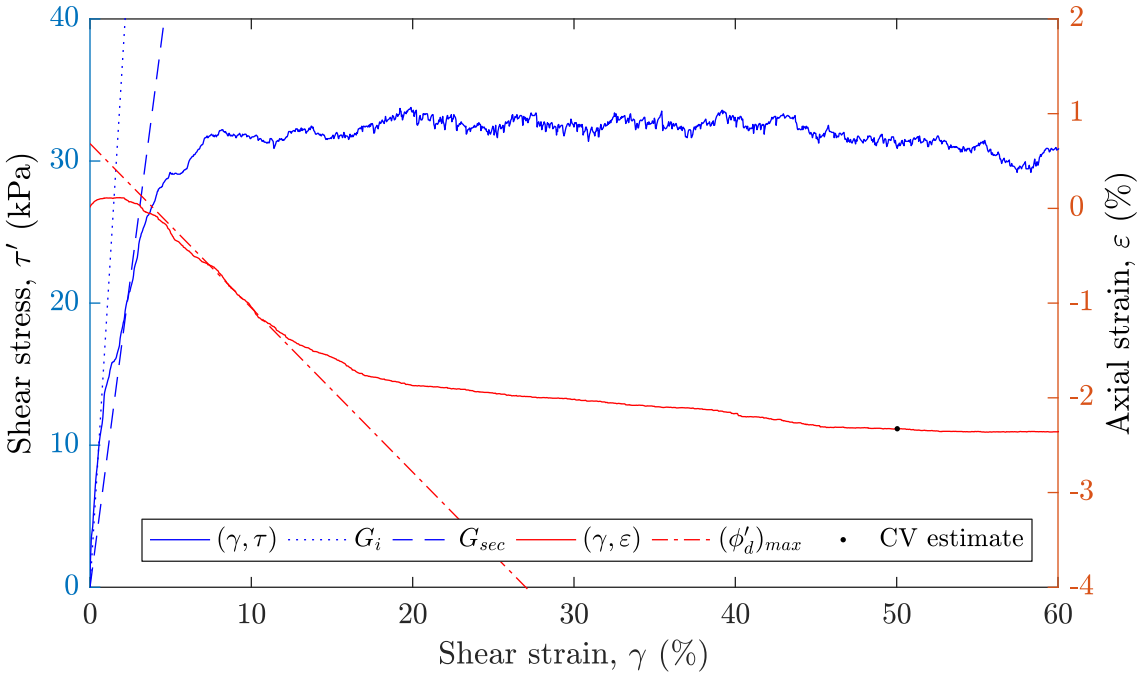

Figure A.8: SS7 $\sigma'_v = 30$ kPa simple shear test results.

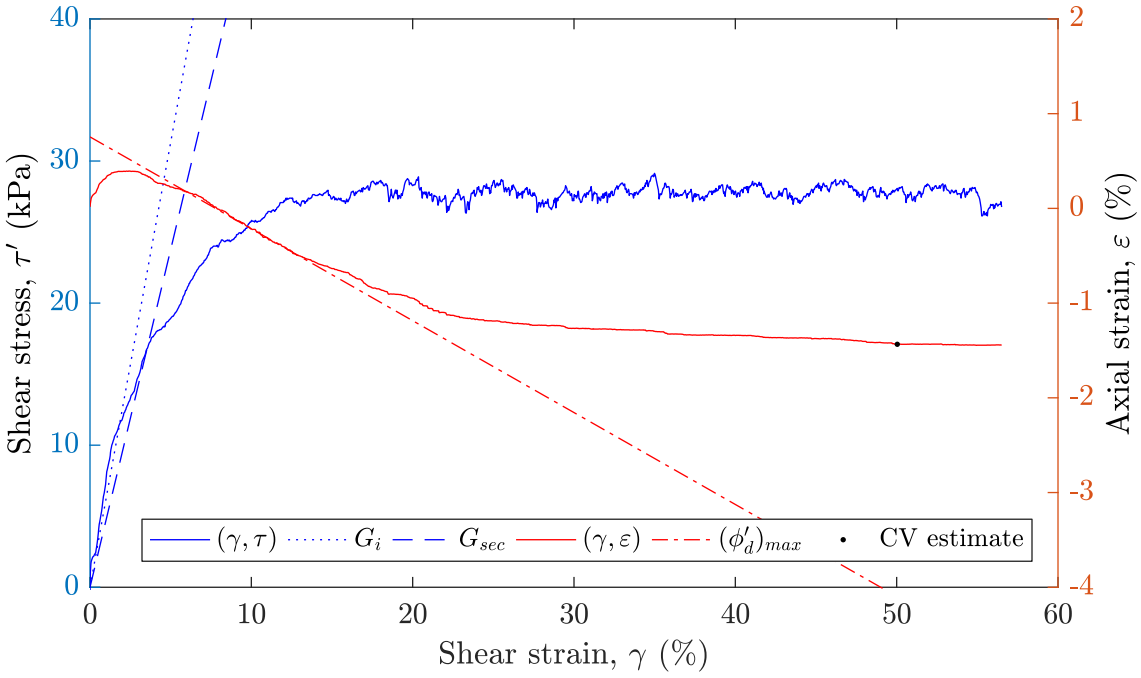

Figure A.9: SS8 $\sigma'_v = 30$ kPa simple shear test results.

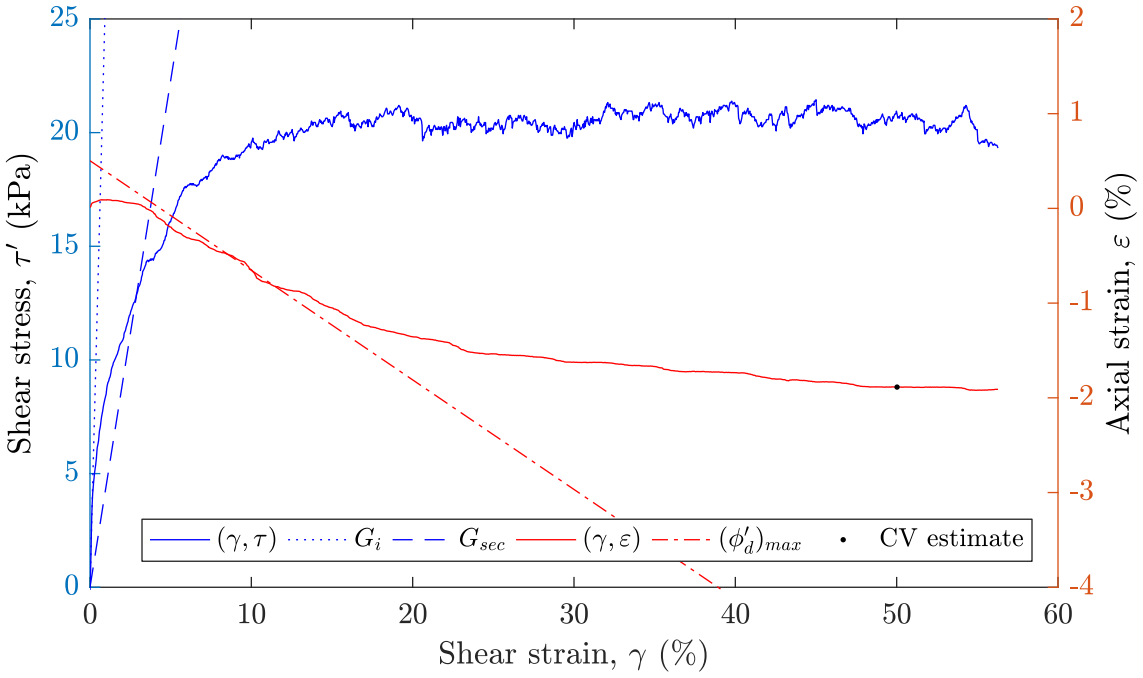

Figure A.10: SS14 $\sigma'_v = 20$ kPa simple shear test results.

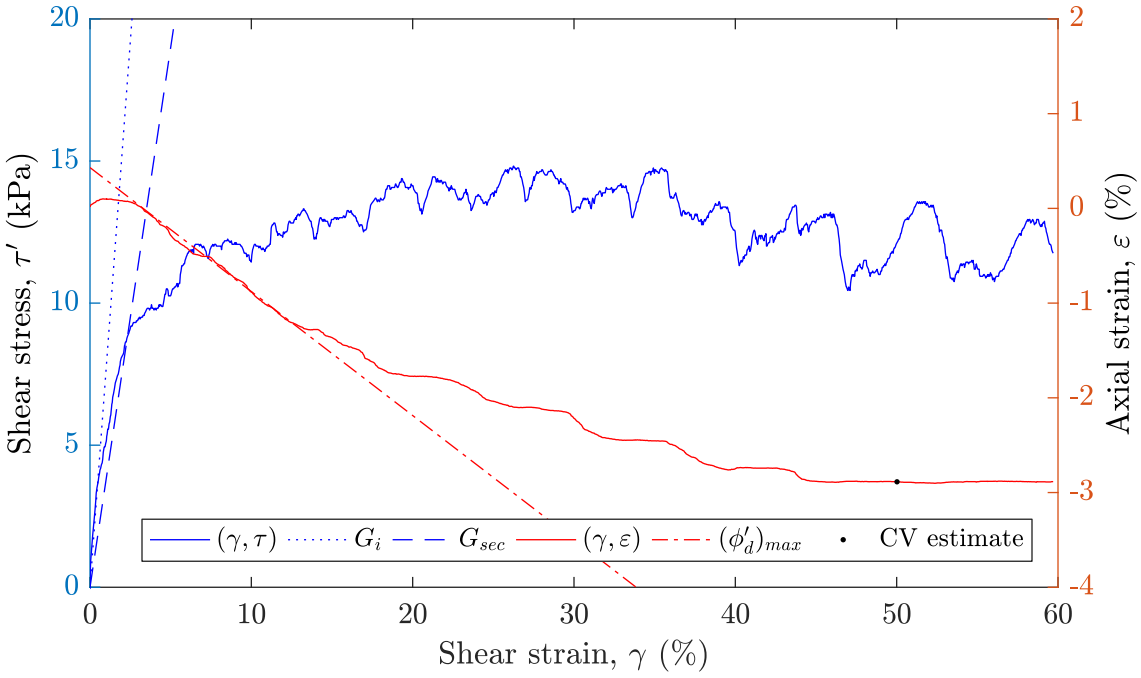

Figure A.11: SS9 $\sigma'_v = 10$ kPa simple shear test results.

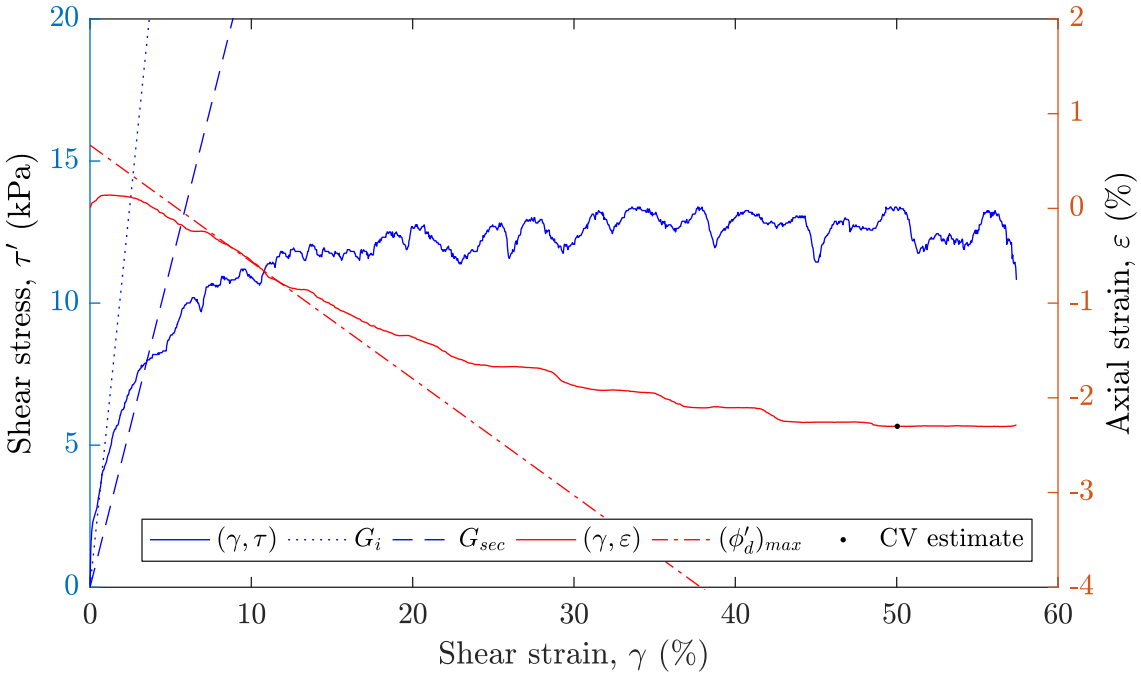

Figure A.12: SS10 $\sigma'_v = 10$ kPa simple shear test results.

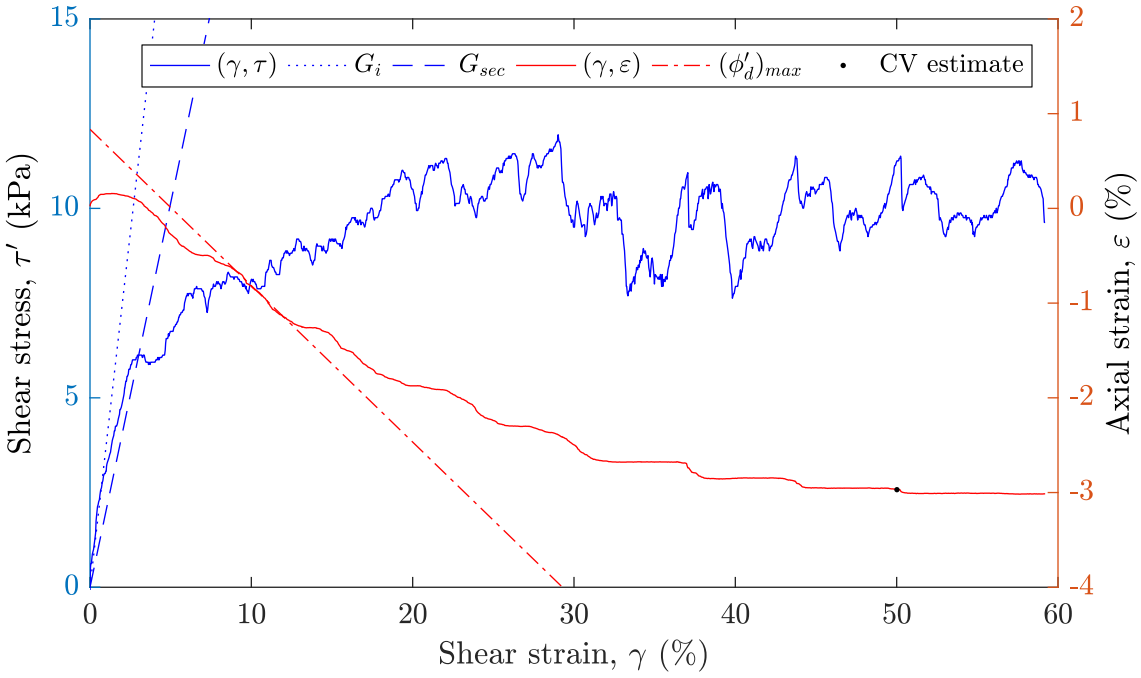

Figure A.13: SS11 $\sigma'_v = 6$ kPa simple shear test results.

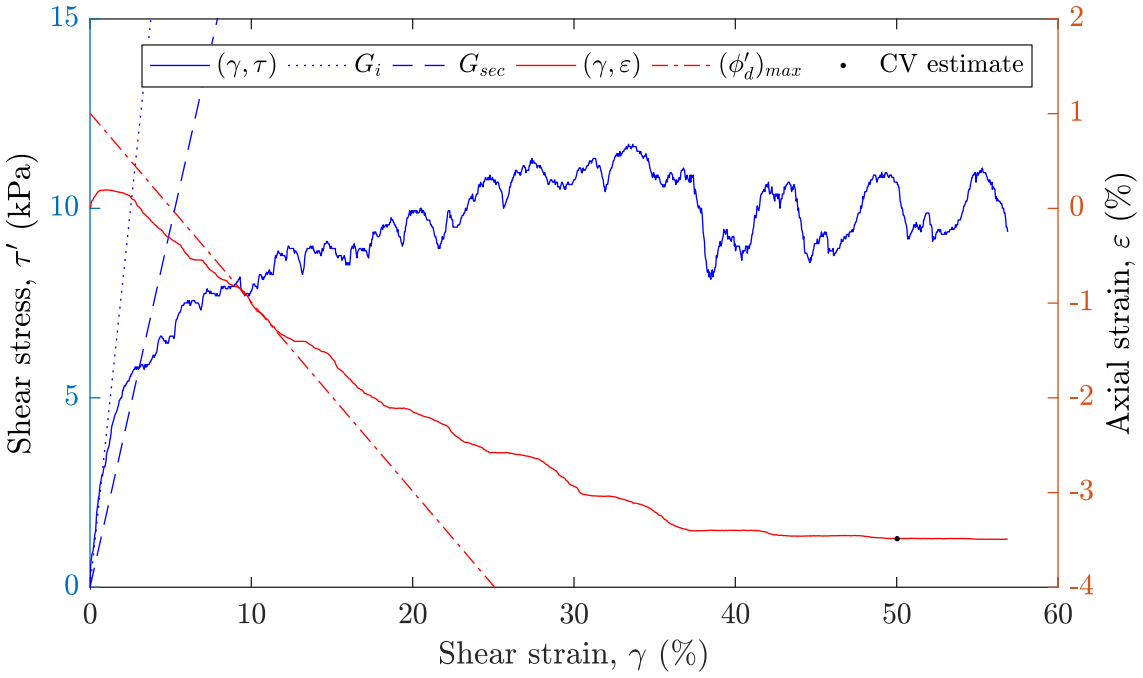

Figure A.14: SS12 $\sigma'_v = 6$ kPa simple shear test results.

Appendix B: Simple Shear Testing Procedures

LIST OF APPENDIX B FIGURES

This procedure, modified from Kraupa (2013), utilizes no water or vacuum grease and is specifically written for granular material testing. Subsequent researchers should examine the following procedures, in addition to available documentation for the Shear Trac II device, and simple shear testing literature to determine the appropriate methodology to perform the respective testing. The procedures were developed when testing oven-dried, fine, poorly graded sand. The testing apparatus and equipment shown in Figure 1 is prepared for simple shear testing. Figure 2 shows further details of the testing apparatus and the orientation convention.

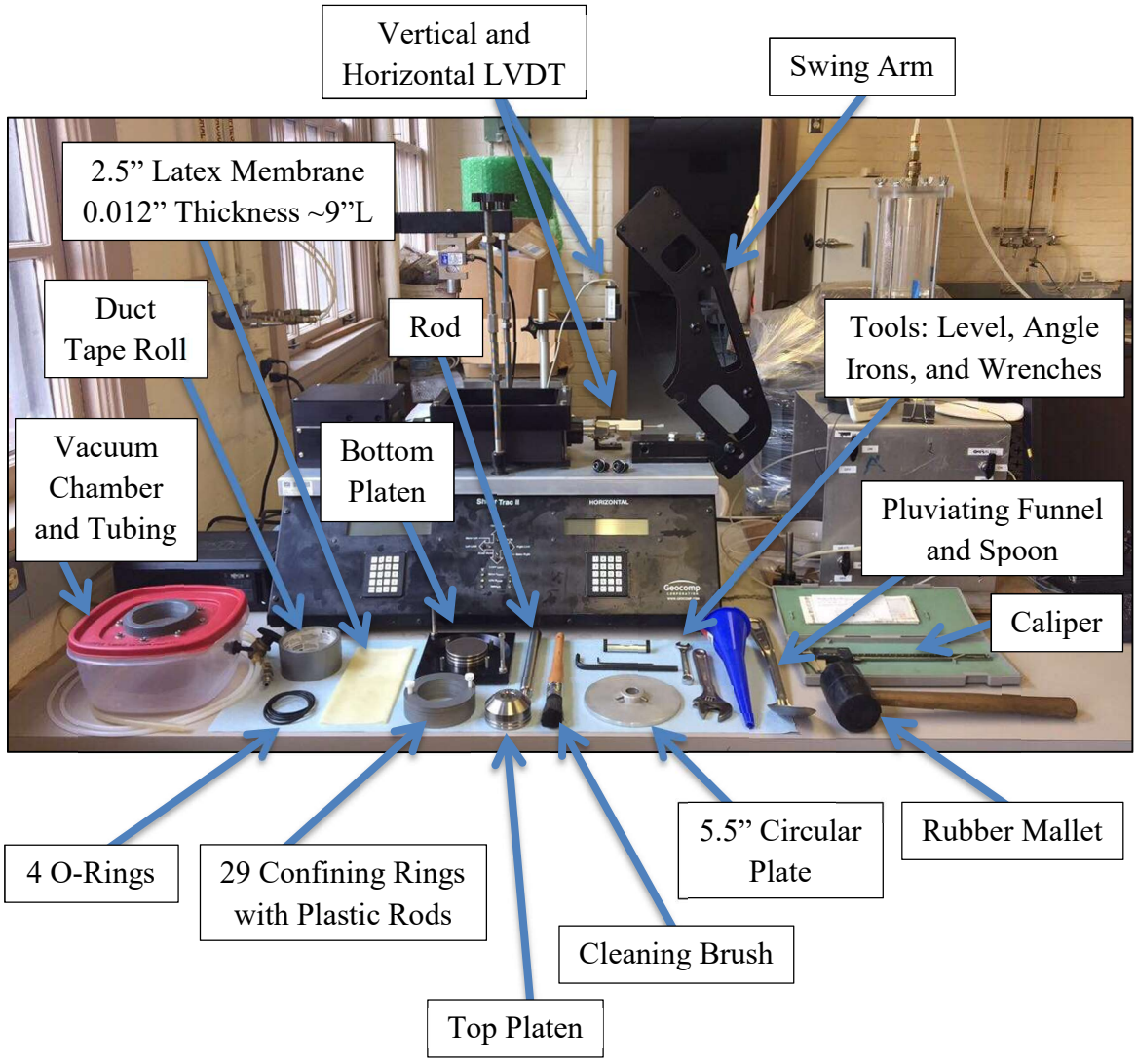

Figure 1: Testing apparatus and materials necessary to perform simple shear testing.

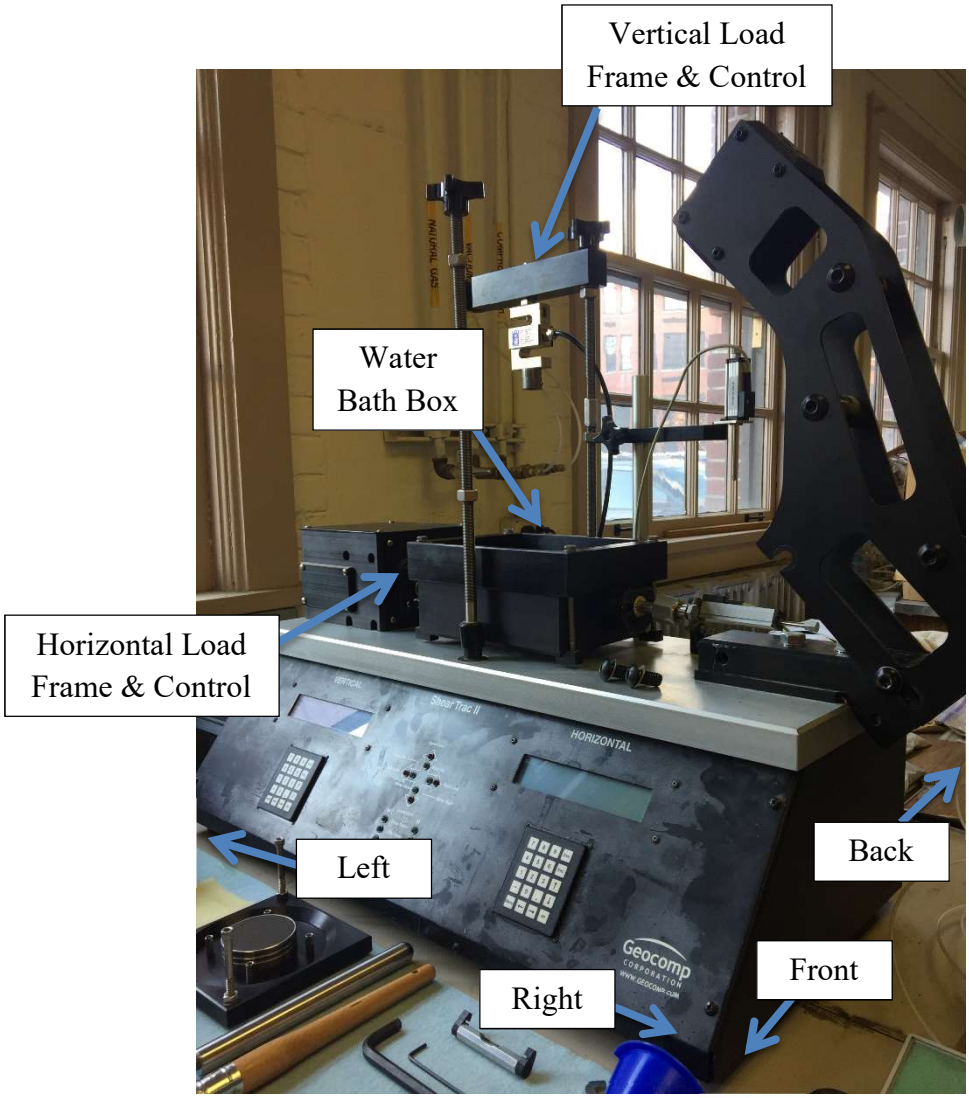

Figure 2: Details and orientation convention of testing apparatus.

The following initial steps should be performed the first time the device is used to complete measurements and calibrations:

1. Ensure clean sample apparatus, free of old sample particulate, dust, etc. Slide latex membrane over bottom platen and stretch 2 O-rings around the platen making sure that the membrane stays flush to the bottom of the platen and air does not become trapped between the membrane and platen (Figure 3). A duct tape roll or any cylindrical item slightly larger than the base can be used to assist stretching the O-rings over the membrane and base.

Figure 3: Assembly of specimen membrane, O-rings, and bottom platen.

2. Inspect and clean the 29 specimen confining rings and slide rings one at a time onto the plastic rods.

3. Carefully place stacked rings with plastic rods centered on the bottom platen, making sure that the membrane does not become pinched (Figure 4).

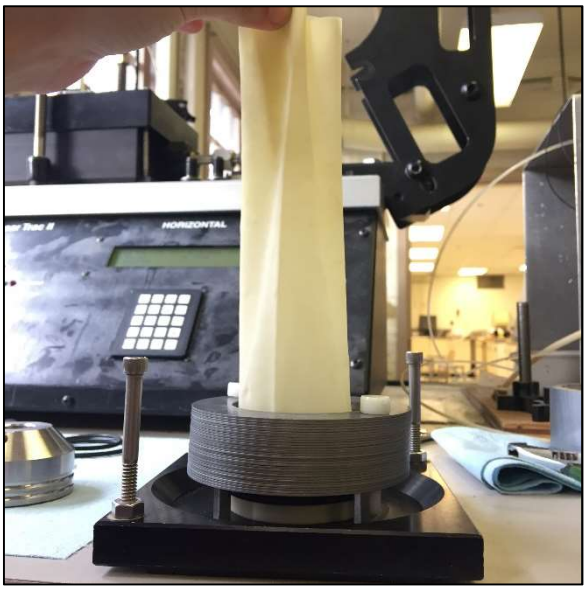

Figure 4: Confining rings stacked onto plastic rods centered on bottom platen.

4. *When the vacuum chamber is used to prepare the soil specimen, it is not possible to take some inner dimensions of the empty system. The first time you the apparatus is used, the inner dimensions must be determined.* Carefully take the plastic rods out of the rings and pull the membrane around the rings. With a caliper, taking care not to poke the membrane, measure the inner diameter with a minimum of three separate measurements around the inside of the membrane enclosed rings. Then, take a minimum of three measurements from the top of the membrane enclosed rings to the porous stone to determine the height of the empty space (Figure 5). Calculate the average of these dimensions and save values for subsequent testing.

Figure 5: Membrane pulled around stacked rings with caliper to obtain inner dimensions.

5. Determine the mass of the top cap, rod, and circular plate that will be applied to the specimen. These values are important when calculating the load to apply from the system in order to obtain the desired loading.

6. Fill the membrane enclosed rings with an arbitrary sand sample that will be used in a process to ensure alignment of the system. Place the top cap over the sand and pull the membrane up and around the cap. Place an O-ring around the membrane enclosed cap, allowing the membrane to sit in the top groove of the cap. Place plastic rods back into the stack of rings to keep the system rigid. Roll the membrane down to the top cap O-ring (Figure 6).

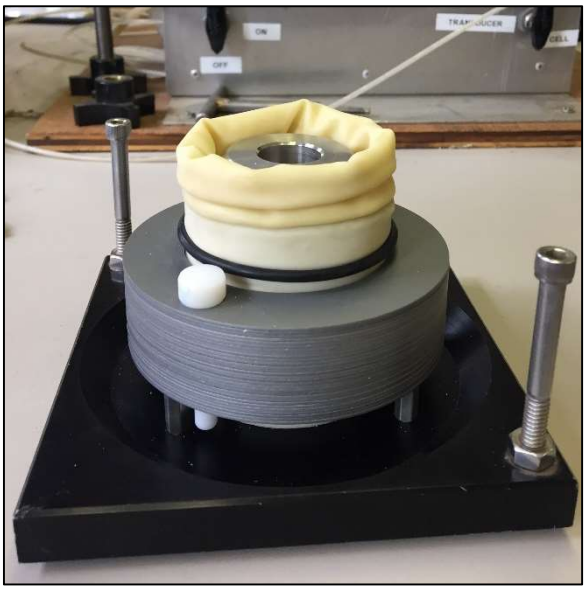

Figure 6: Membrane enclosed top cap placed on sand specimen with O-ring resting in the upper groove of the top cap and extra membrane rolled down to surface of top cap.

7. Ensure that the Shear Trac II equipment is set up as pictured in Figure 7. The swing arm should be bolted in position by the top bolts of the base, and two front side bolts should be removed, and right side bolts should be loosened to allow rotation. Raise the swing arm and lock into place with the front right side bolt.

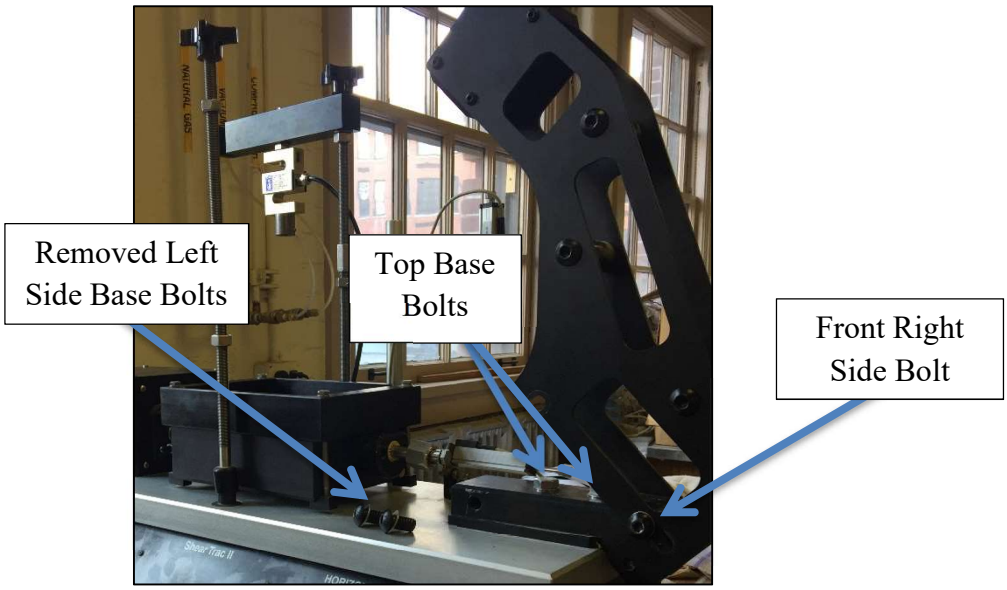

Figure 7: Swing arm initial position.

8. Insert the prepared specimen into the water bath with the bottom drain line pointing left. There are grooves in the bottom of the water bath that guide the specimen base. Center the base between the guides. Lock the sample base in position with the set screws on the water bath box (Figure 8).

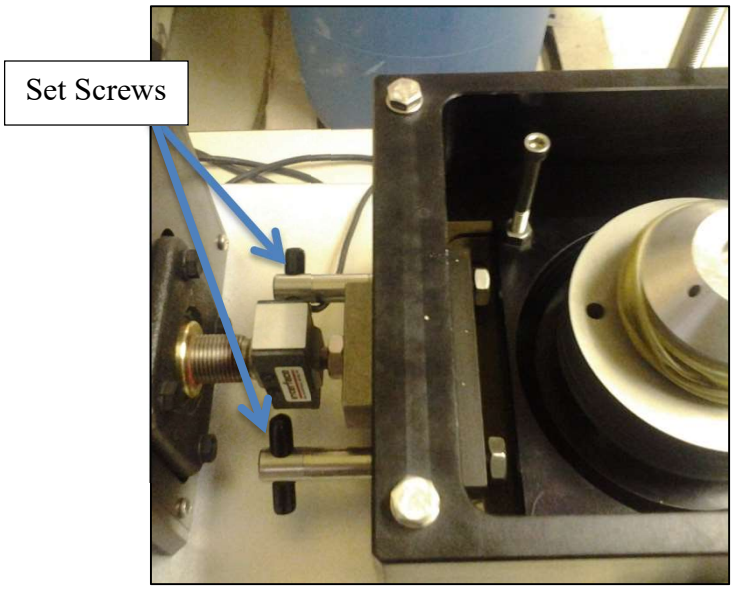

Figure 8: Specimen secured in water bath box.

9. Turn on the Shear Trac II device. Initialize the horizontal position by pressing 2 → 3 → enter on the right (horizontal) front panel. This moves the entire water bath and sample apparatus to correct position.

10. Insert the rod into the shaft of the swing arm, feed the rod into the shaft with the rounded end fed through the lower end of the shaft, otherwise the rod will not fit. While holding the swing arm and rod in place, loosen the front right side bolt to allow swing arm rotation.

11. Lower the swing arm and rod down to the sample, moving the arm as far left as possible, which allows the left side bolts to be secured. Attempt to thread the rod into the specimen cap. If the system allows this threading without disturbing the location of the top cap, then alignment is complete. If the rod falls to the left, right, front, or back of the specimen top cap threads, the top bolts on the swing arm base should be loosened and the swing arm base should be adjusted to align the swing arm. When the position of swing arm allows the rod to thread into the top cap, secure top bolts on swing arm base. Reset apparatus and clean equipment to move on to testing procedures (Figure 9).

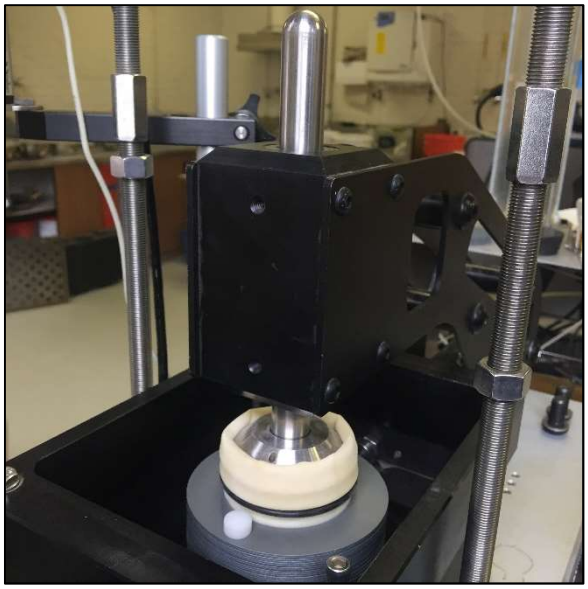

Figure 9: Properly aligned system.

The following procedures should be followed for every subsequent simple shear test:

1. Slide latex membrane over bottom platen and stretch 2 O-rings around the platen making sure that the membrane stays flush to the bottom of the platen and air does not become trapped between the membrane and platen. A duct tape roll or any cylindrical item slightly larger than the base can be used in assisting stretching the O-rings over the membrane and base (refer to Figure 3).

2. Inspect and ensure that the 29 specimen confining rings are clean and slide rings one at a time onto the plastic rods.

3. Carefully place stacked rings centered on the bottom platen making sure that the membrane does not become pinched. Leave the plastic rods in place (refer to Figure 4).

4. Place the bottom platen with membrane and confining rings into the vacuum chamber so that it is centered (use markings on the bottom of chamber as guide) with the drain line pointing left and the vacuum connector pointing right (Figure 10). Close the lid, being careful not to disturb the confining rings.

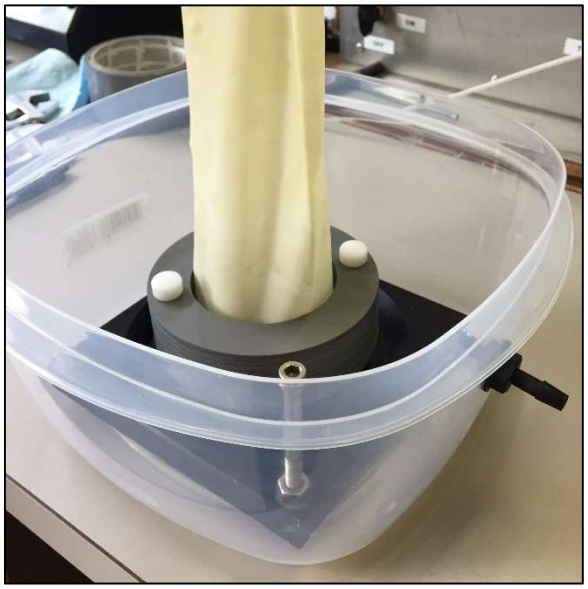

Figure 10: Specimen apparatus placed in vacuum chamber.

5. Gently pull the top of the membrane up through the vacuum chamber lid and roll the membrane around the fitting ring to keep in place to create a sealed system. There should be some slack left in the membrane as to not introduce tension or torsional forces to the specimen when removed from vacuum chamber (Figure 11 - left).

6. Apply a low level of vacuum to the chamber (Figure 11 - right). If a regulator is available, determine what pressure is sufficient to eliminate space between the membrane and the confining rings. If no regulator is available, a valve can be opened slightly to apply a low vacuum sufficient to eliminate space between the membrane and the confining rings. Care should be taken at this step not to apply too high of vacuum pressure to the chamber or the membrane will become overly stretched or break. As vacuum is applied, smooth the membrane to the sides of the confining rings, ensuring good contact with no creases formed.

Figure 11: Membrane stretched around vacuum chamber lid fitting (left), with slight vacuum applied to chamber (right).

7. Record the initial mass of dry material to be tested in a bowl.

8. Carefully spoon material from bowl into funnel placed within the membrane terminating at the bottom porous stone and air pluviate the sample (Figure 12). Fill the space within the membrane until soil is near the surface of the confining rings.

Figure 12: Air pluviation process.

9. Return excess material from spoon and funnel to the bowl and record the final mass reading of the remaining material in the bowl.

10. Gently smooth the surface of the specimen and tap top area of vacuum chamber slightly with rubber mallet to aid in leveling the sample, do not over-densify the sample in this step to allow for increasing density in subsequent steps. Add filter paper of correct size to sample surface and insert top cap with rod threaded all the way into it. Let the cap rest over the surface of the sample and reset several times to level the surface (Figure 13). Remove the top cap and rod and filter paper.

Figure 13: Specimen leveling process.

11. Insert caliper into vacuum chamber to measure the distance between the top of the confining rings and the surface of the sample. Take multiple measurements. Report an average depth.

12. Calculate the relative density of the sample from the calculated volume and mass of specimen. If greater density is desired, tap top of vacuum chamber carefully with a mallet to vibrate the specimen into a denser arrangement. Measure the depth from the top of the confining rings to the surface of the sample and calculate the relative density again. Repeat if necessary to reach the desired initial state.

13. Screw the rod into the top platen only several turns so that it is easy to unscrew and lower the platen to the surface of the specimen through the lid of the vacuum chamber. Gently unscrew the rod from the top platen.

14. Remove vacuum from the system slowly so that the membrane comes into contact with the sides of the top cap in a controlled motion (Figure 14).

Figure 14: Top cap in place with vacuum released.

15. Slowly unroll the top of the membrane from the fitting ring on the vacuum chamber lid and remove the vacuum chamber lid, making sure not to disturb the specimen. Check the perimeter of the cap in comparison to the confining rings to ensure that it is level.

16. Place O-ring around the top cap to secure the membrane to the sides of the platen. A duct tape roll or any cylindrical item slightly larger than the top platen can be used in assisting stretching the O-rings over the membrane and top platen. The O-ring should fall into the top groove of the specimen top cap to ensure that the O-ring does not contact the top of the confining rings at any point during the simple shear test.

17. Roll the extent of the membrane down around the top section of the cap without disturbing the specimen. Do not allow the membrane to roll under the O-ring on the cap to avoid obstructing the cap from moving downward during loading (refer to Figure 6).

18. Loosen the front right side bolt on the base of the swing arm and relock it gently so that it is easily unlocked to avoid jolting the sample once it is in place. Insert the built specimen into the shear box avoiding collisions with the loading arms and ledges. The bottom of the shear box shows the drainage line that should be pointing left when inserted in the water bath box. The specimen apparatus should fit into the grooves in the bottom of the shear box, adjust to centered position.

19. Tighten the set screws at the base of the shear box (refer to Figure 8).

20. Turn on the Shear Trac II device.

21. Initialize horizontal actuator. On the right panel press: 2 → 3 → enter. The motor will automatically stop when the unit reaches the correct position. The initialized position should be used to ensure proper alignment with the cross bar that positions the vertical load frame and does not impose any eccentricity or unintended loads following the initial steps of this procedure that should ensure system alignment.

22. Unlock the swing arm and insert the rod into the shaft. Lower the swing arm being careful not to let the rod impact the specimen cap. Once the swing arm is lowered and brought to the far left position, lower the rod to the specimen cap and gently screw in the rod to the specimen cap, making slight adjustments if necessary. This step ensures that then the final setup is made that the rod will easily thread into the specimen cap (refer to Figure 9).

23. Unthread the rod from the cap and raise the swing arm and lock into upright position with the front right side bolt of the swing arm base. Remove the rod from the shaft. Remove the plastic rods from the confining rings.

24. Secure the 5.5” circular plate to the rod by lowering the plate onto the rod starting at the rounded end. The bottom of the plate should align with a mark left on the rod to ensure sufficient spacing between the specimen cap and the swing arm when placed in its final position.

25. Unlock the swing arm and insert the rod with plate attached into the shaft. Lower the swing arm and bring to the leftmost position being careful not to let the rod impact the specimen cap. Begin threading the rod into the specimen cap when contact is made making sure that no load from the swing arm is being applied to the specimen by the arm resting on the circular plate. Hold up the swing arm slightly while threading the rod until lowering it all the way will not push down on the specimen through the rod. Complete threading the rod into the specimen cap and ensure there is at least a small gap between the bottom of the circular plate and the specimen cap with the rolled membrane. If the location of the circular plate needs to be adjusted during this process, care should be taken not to apply force to the specimen.

26. Secure all four bolts on the side of the swing arm base to fix position of the swing arm.

27. Place and lock the vertical LVDT into position atop the circular plate and lower slightly so that the measuring pin will be engaged throughout testing (Figure 15). Ensure that the body of the LVDT is free of contact from the swing arm and cross bar side poles for the vertical load controls.

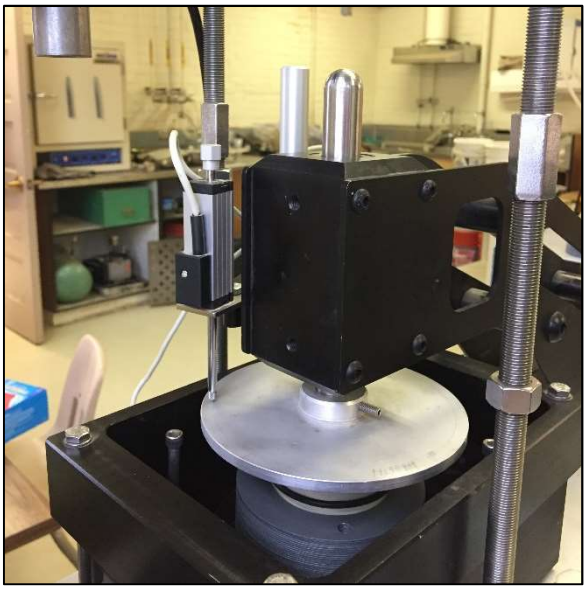

Figure 15: Specimen secured in water bath box. Rod screwed into top cap with circular plate attached and LVDT in place.

28. Swing cross-bar into place. The crossbar should be just slightly above the top of the rod. Level the crossbar and tighten the four prong nuts (Figure 16).

Figure 16: Shear Trac II device and specimen apparatus fully assembled.

29. Lower crossbar until the load cell slightly touches the top of the stainless-steel rod. On the left panel press: 2 → 1 → enter. Once a load is registered by the cell press any button to stop lowering the crossbar. Do not allow the system to apply load to specimen in this step. Stop crossbar motion once the slightest change in load is registered and the load cell is in good contact with the rod.

The following steps detail the software setup to perform a constant vertical stress (i.e., “drained”) simple shear test:

1. Using the left panel (vertical control: ID 101) on the front of the Shear Trac II device, go to the control option (press 3) and select apply and maintain load (press 2).

2. Specify the final vertical stress and loading rate.

3. Specify the final displacement; with a constant vertical stress test the max allowable vertical displacement should be large. Having too small of a predefined max displacement will abort the test before intended.

4. Specify the sampling period.

5. Using the right panel (horizontal control: ID 102) on the front of the Shear Trac II device, go to the control option (press 3) and then choose the constant displacement rate option (press 1).

6. Specify the displacement rate, maximum horizontal displacement and sampling period.

7. Specify the final horizontal load, ensuring that the input value is large enough to allow the test to finish before the final load is reached. Do not input a load higher than the load cell capacity.

8. Zero the horizontal and vertical load cells. This can be done by navigating to: (Desktop\Shortcut to DSS\DS Testing Info\Software\DSS\shear.dss.exe) and bring down the view menu and open the system window. In addition, bring down the calibrate menu and open the summary window.

9. For both the horizontal and vertical load cells, make sure that the offset values are the same in both windows. If not, change the offset value in the calibration summary window. Once this is done, the reading from the system window for both the vertical and horizontal load cells should be zero (Figure 17).

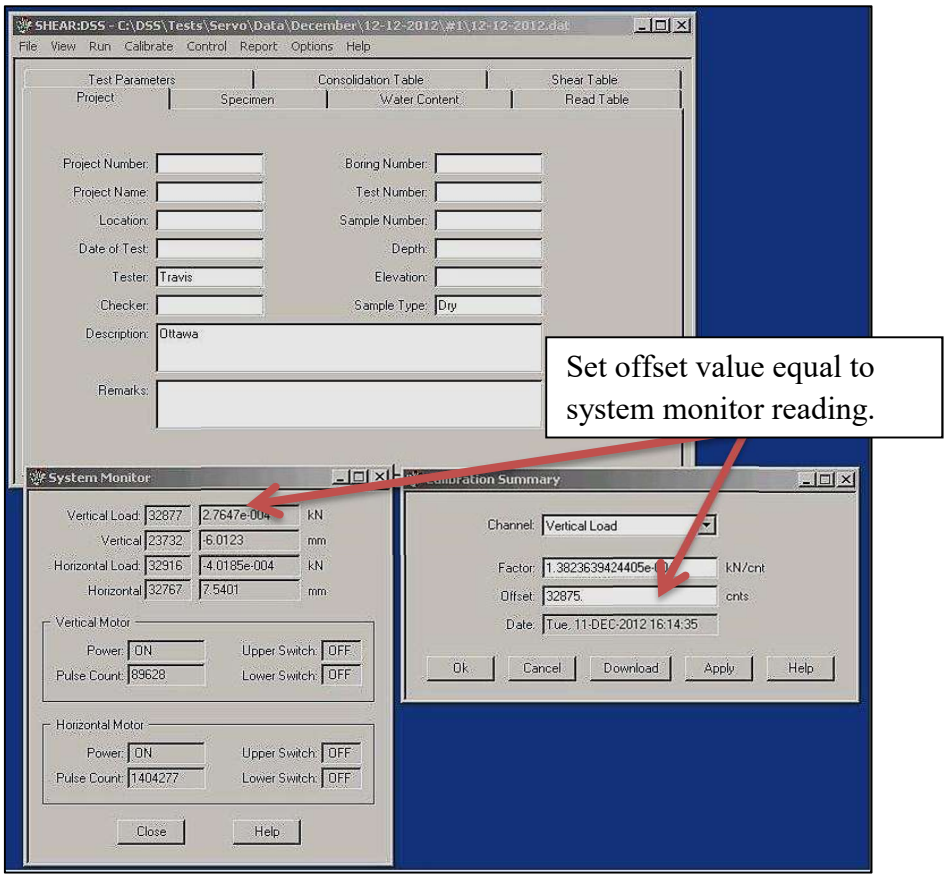

Figure 17: Zeroing of load cells.

10. Navigate to: (Desktop\Shortcut to DSS\DS Testing Info\Software\diags.com20.exe). Open this program twice.

11. Place the windows side by side and type 101 and 102 for the vertical and horizontal control ID's respectively.

12. Bring down the view menu and open the panel window. Do this for each of the control windows. The panel windows display the same information as the two panels on the front of the Shear Trac II device (Figure 18).

13. The user can control the system from the panel windows or from the keypads on the front of the unit.

14. From the 101 control panel window start the vertical loading sequence. Click on: 3→2→6→Enter.

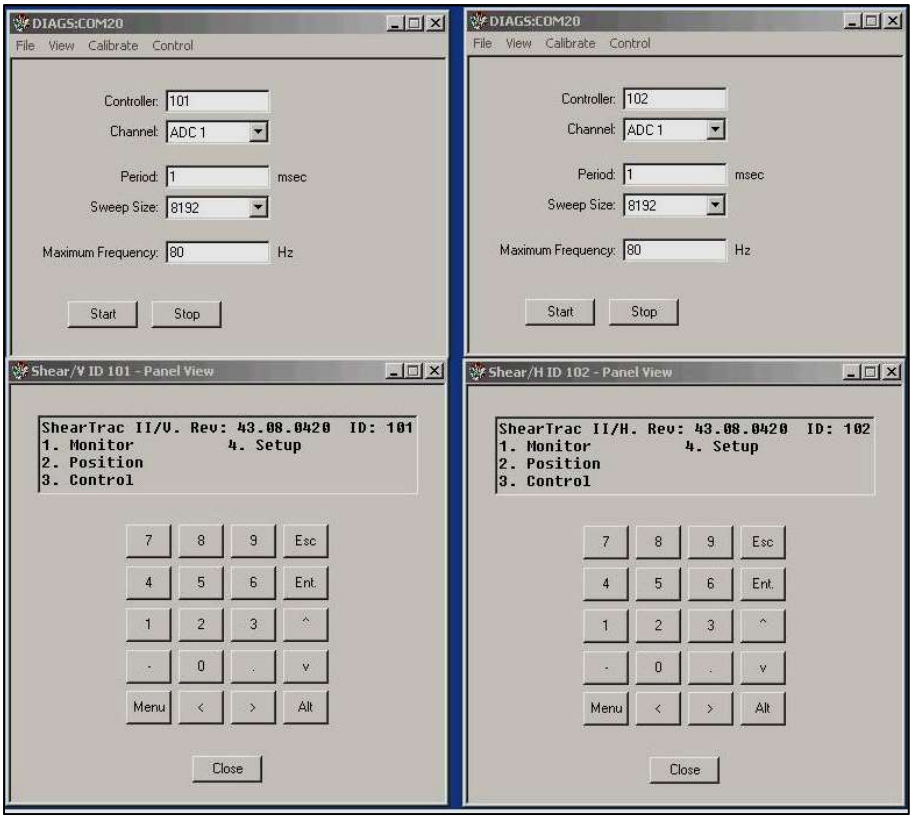

Figure 18: Panel windows.

15. Once the system has reached the desired vertical load, allow specimen to consolidate.

16. Start the horizontal loading sequence using the 102 control panel window. Click on: 3→1→6→Enter.

17. Wait until shearing phase is complete.

The following steps detail the disassembly of the simple shear apparatus after testing and steps to successfully download testing data.

1. Once test is complete: bring down the file menu and open the download window.
2. Right-click and click on select all.
3. Right-click and click copy.
4. Paste in notepad or excel and save data files.
5. Do step 2 for both controller windows.
6. Initialize shear actuator and raise crossbar.
7. Swing crossbar away from rod and remove the vertical LVDT from the circular plate.
8. Loosen set screws holding the circular plate and unscrew rod from top platen.
9. Loosen the four bolts securing the swing arm and raise it.
10. Loosen the two set screws at the base of the shear box.
11. Remove specimen from water bath box and clean specimen apparatus.